ABSTRACT

Title of Dissertation: QUANTITATIVE ANALYSIS OF THE ATMOSPHERIC OXIDATION OF ISOPRENE USING MODELS AND MEASUREMENTS: IMPACTS ON SURFACE OZONE

Margaret Rosemary Marvin,
Doctor of Philosophy, 2019

Dissertation directed by: Adjunct Professor Glenn Wolfe,
Department of Atmospheric and Oceanic Science

Professor Ross Salawitch,
Department of Chemistry and Biochemistry,
Department of Atmospheric and Oceanic Science,
Earth System Science Interdisciplinary Center

The oxidation of isoprene – one of the most abundant volatile organic compounds (VOCs) in our atmosphere – significantly impacts the formation of surface ozone, which is detrimental to public health. Computer models simulate the complex relationships between ozone and VOCs like isoprene and are used to guide policy decisions directed at improving ozone. However, uncertainties in the emissions and chemistry of isoprene limit the accuracy of modeled ozone. This body of work comprises a quantitative analysis of atmospheric isoprene oxidation that strives to identify and improve such uncertainties through the combination of models with measurements. Measurements used in this work mainly comprise *in situ* observations from the Southeast Nexus (SENEX) aircraft campaign, which sampled atmospheric composition across the isoprene-rich summertime Southeast US. I have prepared two

models – the Framework for 0-D Atmospheric Modeling (F0AM) and the Comprehensive Air Quality Model with Extensions (CAMx) – to drive simulations of atmospheric isoprene oxidation, which are evaluated against observations from SENEX. Using F0AM, a photochemical box model, I demonstrate that several commonly-used mechanisms significantly underestimate measured mixing ratios of formaldehyde, a high-yield product of isoprene oxidation, by 0.5–1 ppb across a wide range of NO_x conditions. The consistent underestimation of formaldehyde suggests a deficit of VOC oxidation among all considered mechanisms. Although the cause for this deficit remains elusive, I provide recommendations for improving the simulated production of formaldehyde upon isoprene oxidation in the Carbon Bond version 6 revision 2 (CB6r2) mechanism, commonly used for air quality modeling. Using CAMx, a three-dimensional chemical transport model, I produce a standard air quality modeling scenario that simulates atmospheric composition across the continental US for the summer of 2013. Evaluation of this scenario reveals that the emissions of isoprene from the Biogenic Emissions Inventory System (BEIS) are underestimated in the Southeast US by at least 40%. Finally, implementation of improvements in the emissions and chemistry of isoprene within the CAMx modeling framework increases the net photochemical production of surface ozone by up to 0.5 ppb hr^{-1} and shifts surface ozone production regimes more NO_x-limited, relative to the standard platform for regional air quality modeling.

QUANTITATIVE ANALYSIS OF THE ATMOSPHERIC OXIDATION OF ISOPRENE USING MODELS AND MEASUREMENTS: IMPACTS ON SURFACE OZONE

by

Margaret Rosemary Marvin

Dissertation submitted to the Faculty of the Graduate School of the
University of Maryland, College Park, in partial fulfillment
of the requirements for the degree of
Doctor of Philosophy
2019

Advisory Committee:
Adjunct Professor Glenn Wolfe, Co-chair
Professor Ross Salawitch, Co-chair
Professor Timothy Canty
Professor Russell Dickerson
Professor Alice Mignerey
Professor Akua Asa-Awuku, Dean's Representative

Acknowledgements

I would first like to thank my doctoral advisors, Professors Ross Salawitch and Glenn Wolfe, without whose guidance this work would not be possible. To both of you, thank you for helping me find my research niche and for supporting me ever since. Thank you to my supporting network of colleagues and co-authors, from UMD, NASA, NOAA, and several other research institutions. Thank you to the Salawitch-Dickerson-Canty-Allen atmospheric chemistry group at UMD for providing valuable feedback on my doctoral research over the years. Thank you to Professor Timothy Canty for dedicating your time to helping me practice my public speaking, and thank you to Linda Hembeck, Dr. Allison Ring, Dr. Daniel Goldberg, and Dr. Hao He for providing computer code and programming support. Thank you also to the agencies that funded my research, with special thanks to the NASA Earth and Space Science Fellowship program, which provided three years of financial support.

I am also incredibly grateful for the family, friends, and cats who have blessed me with their love and support over the last five and half years. Thank you, Greg Porter, for meeting me on this path and never letting go. Thank you to Mom, Dad, and Wyatt for always being ready for a phone call. Thank you to the Porters, Ostashes, and Meyerses for welcoming me into your families. Thank you to Emily McGowan, Katie Wesley, Sara Talvacchio, and Kristen and Lawrence Staten for your company and many fabulous adventures. Thank you to Pam Wales, Sandra Roberts, Dolly Hall, Laura McBride, Sarah Benish, and Doyeon Ahn, who are not only wonderfully supportive colleagues, but have also become dear friends. And finally, thank you to Alfredo and Noodle, you know who you are.

Table of Contents

List of Tables

List of Figures

Chapter 1: Introduction

1.1 Motivation

Ozone (O_3) is an important gas-phase atmospheric constituent that is detrimental to public health. Excessive exposure to surface ozone has been linked to respiratory and cardiovascular disease, as well as premature mortality (EPA, 2013), earning its designation as one of the six "criteria air pollutants" regulated by the US Environmental Protection Agency (EPA) (https://www.epa.gov/criteria-air-pollutants). Ground-level ozone is federally mandated to meet a National Ambient Air Quality Standard (NAAQS) of 70 ppb, evaluated as a three-year average of the annual fourth-highest daily 8-hour maximum ozone concentration at any given location (https://www.epa.gov/criteria-air-pollutants/naaqs-table). Many regions of the US, especially large urban areas such as Los Angeles, Houston, and New York City, fail to meet attainment of the NAAQS (https://www3.epa.gov/airquality/greenbook/jnc.html). In nonattainment regions, State Implementation Plans (SIP) are designed to combat the photochemical production of ground-level ozone, which is complicated by a nonlinear dependence on its precursor species: volatile organic compounds (VOC) and NO_x (NO_x = NO + NO_2). Nitrogen oxides are primarily introduced to the atmosphere via anthropogenic emission, whereas VOCs may originate from emissions that are either anthropogenic or biogenic in nature (EPA, 2015a).

Isoprene (C_5H_8) is a biogenic VOC that is emitted by trees into the atmosphere at a rate of about 500 Tg yr^{-1}, accounting for ~30% of global non-methane volatile organic compound (VOC) emissions (Guenther et al., 2012). The chemical structure of

isoprene features a conjugated diene, a highly reactive organic functional group. This functional group is particularly reactive to oxidation by the hydroxyl radical (OH), which limits the atmospheric lifetime of isoprene to less than a few hours (Pike and Young, 2009). The subsequent chemistry for isoprene and its oxidation products is complex, and although the scientific understanding of the isoprene oxidation mechanism has evolved considerably in recent years, multiple aspects of this mechanism remain under debate, such as isomerization rates for isoprene peroxy radicals, yields of isoprene nitrates, and regeneration of OH (Mao et al., 2013b). However, it is widely recognized by the scientific community that OH oxidation reduces isoprene into numerous smaller VOCs and, in the presence of NO_x, may also contribute to the production of ozone (Trainer et al., 1987).

Computer models are often used to simulate the complex relationships between ozone, NO_x, and VOCs like isoprene. Although these models sometimes agree with observations of ozone, ozone precursors are often misrepresented (Canty et al., 2015; Goldberg et al., 2016). Atmospheric modeling of isoprene, for example, is limited by uncertainties in isoprene emissions and chemistry. Isoprene emissions can be difficult to reproduce due to the variety of factors that influence biogenic emissions, such as vegetation landcover and leaf temperature. As a result, different biogenic emissions inventories may produce conflicting results. For example, isoprene emissions generated by the Model of Emissions of Gases and Aerosols from Nature (MEGAN) (Guenther et al., 2012) and the Biogenic Emissions Inventory System (BEIS) (Bash et al., 2016) can differ by up to a factor of 2 (Carlton and Baker, 2011; Warneke et al., 2010). The complexity of isoprene oxidation chemistry and its related uncertainties often lead to inconsistent representation of the isoprene oxidation scheme among the

gas-phase chemical mechanisms developed for atmospheric models (Hildebrandt Ruiz and Yarwood, 2013; Jenkin et al., 2015; Mao et al., 2013b). Some mechanisms are more detailed than others; some consider recent updates to the chemistry while others do not; and sometimes the difference simply comes down to choice of kinetics database for rate constant information. Mechanism inter-comparison studies have shown that different interpretations of isoprene chemistry lead to conflicting representations of isoprene oxidation products, with simulated mixing ratios for ozone varying by as much as 20 ppb under typical atmospheric conditions for NO_x (1 ppb) (Archibald et al., 2010b; Pöschl et al., 2000; von Kuhlmann et al., 2004; Zhang et al., 2011).

This body of work aims to further improve the simulation of ozone in atmospheric models through quantitative analysis of isoprene and its oxidation products. Specifically, I apply measurements of atmospheric composition to evaluate and improve model representations of isoprene chemistry and emissions, in support of the following science questions:

- How well do models simulate atmospheric isoprene oxidation, and what are the limiting uncertainties?
- How can we minimize uncertainties and improve our ability to model isoprene and its oxidation products?
- How do such improvements impact the simulation of surface ozone, and what are the implications for air quality policy?

1.2 Background chemistry

1.2.1 Ozone production

Production of tropospheric ozone is initiated by formation of the hydroxyl (OH) radical via photolysis of existing ozone (R1.1 and R1.2) (Crutzen, 1973):

$$O_3 + h\nu \rightarrow O^1D + O_2 \quad \text{(R1.1)}$$

$$O^1D + H_2O \rightarrow 2\ OH \quad \text{(R1.2)}$$

Once formed, OH may oxidize nearby hydrocarbons (denoted RH below) in sunlight to produce organic peroxy radicals (RO_2) (R1.3 and R1.4):

$$RH + OH \rightarrow R + H_2O \quad \text{(R1.3)}$$

$$R + O_2 + M \rightarrow RO_2 + M \quad \text{(R1.4)}$$

These RO_2 radicals may then undergo varying photochemical fates depending on conditions for NO_x (Jacob, 1999; Thornton et al., 2002).

When NO_x is not present, RO_2 will react with other available radicals such as HO_2 or even other RO_2 to produce stable oxygenated VOC and molecular oxygen (O_2), but not ozone. Such VOCs may include hydroperoxides (ROOH) (R1.5) and aldehydes (R'CHO) (R1.6), where R' represents an organic functional group that contains one less carbon and two less hydrogen atoms than R:

$$RO_2 + HO_2 \rightarrow ROOH + O_2 \quad \text{(R1.5)}$$

$$RO_2 + RO_2 + O_2 \rightarrow 2\ R'CHO + 2\ HO_2 \quad \text{(R1.6)}$$

When NO_x is present, RO_2 may react with NO to form an organic oxy radical (RO) and NO_2 (R1.7). The RO radical subsequently degrades to form the stable aldehyde R'CHO as well as the HO_2 radical (R1.8), which also reacts with NO to

produce NO_2 (R1.9). Each resulting NO_2 molecule then photolyzes in air to produce atomic oxygen, which is rapidly converted to ozone (R1.10 and R1.11):

$$RO_2 + NO \rightarrow RO + NO_2 \quad \text{(R1.7)}$$

$$RO + O_2 \rightarrow R'CHO + HO_2 \quad \text{(R1.8)}$$

$$HO_2 + NO \rightarrow OH + NO_2 \quad \text{(R1.9)}$$

$$NO_2 + h\nu \rightarrow NO + O \quad \text{(R1.10)}$$

$$O + O_2 + M \rightarrow O_3 + M \quad \text{(R1.11)}$$

Since R1.7 and R1.9 each form a molecule of NO_2, R1.10 and R1.11 occurs at least twice in the VOC oxidation chain. Thus, in the presence of NO_x, each VOC molecule is therefore capable of producing at least two molecules of ozone:

$$\text{Net: } RH + 4\ O_2 \rightarrow R'CHO + H_2O + 2\ O_3 \quad \text{(R1.12)}$$

Furthermore, smaller oxygenated VOCs produced through the OH oxidation of RH, such as R'CHO, may undergo subsequent oxidation, producing even more ozone. Theoretically, each carbon atom per VOC molecule is oxidized to CO, which undergoes OH oxidation itself, and therefore also carries the potential to produce ozone. The OH oxidation of CO initially produces CO_2 and HO_2 (R1.13 and R1.14):

$$CO + OH \rightarrow CO_2 + H \quad \text{(R1.13)}$$

$$H + O_2 + M \rightarrow HO_2 + M \quad \text{(R1.14)}$$

Ozone production then proceeds via R1.9–R1.11, leading to the net production of one ozone molecule per molecule of CO:

$$\text{Net: } CO + 2\ O_2 \rightarrow CO_2 + O_3 \quad \text{(R1.15)}$$

It can thus be understood how, in the presence of NO_x, the VOC oxidation chain can contribute significantly to the formation of surface ozone (Trainer et al., 1987).

Ozone production is limited by the conversion of NO to NO_2 in R1.7 and R1.9, and is commonly represented as follows:

$$P(O_3) = k_{HO2+NO}[HO_2][NO] + \sum k_{RO2i+NO}[RO_{2i}][NO] \quad (1.1)$$

where $P(O_3)$ is the ozone production rate (molecules cm^{-3} s^{-1}), k_{HO2+NO} and $k_{RO2i+NO}$ are reaction rate constants (cm^3 $molecule^{-1}$ s^{-1}), and $[HO_2]$, $[RO_{2i}]$, and [NO] are species concentrations (molecules cm^{-3}). The subscript *i* denotes the separation of RO_2 into individual species for calculation of the second term.

Radical termination is achieved by reactions between HO_x ($HO_x = OH + HO_2$), NO_x, and RO_2. One example is the reaction of HO_2 with RO_2 to produce organic peroxides, as described in R1.5. Other common examples include the self-combination of HO_2 to form hydrogen peroxide and the reaction of OH with NO_2 to form nitric acid (R1.16 and R1.17, respectively):

$$HO_2 + HO_2 \rightarrow H_2O_2 + O_2 \quad (R1.16)$$

$$OH + NO_2 + M \rightarrow HNO_3 + M \quad (R1.17)$$

When radical termination is controlled by reactions among HO_x and RO_2, tropospheric production of ozone is considered NO_x-limited and, when nitric acid formation is the dominant termination step, ozone production is considered VOC-limited (Sillman, 1999, 1995; Sillman et al., 1990). Thus, radical termination defines the nonlinear dependence of tropospheric ozone production on NO_x and VOCs. This nonlinearity is represented visually in Fig. 1.1, which shows model simulated ozone mixing ratios (ppb) as a function of VOC and NO_x emissions (10^{11} molecules cm^{-2} s^{-1}). Under NO_x-limited conditions (left of the dividing line), ozone production increases with rising NO_x emissions but is relatively insensitive to VOC emissions; whereas, under VOC-

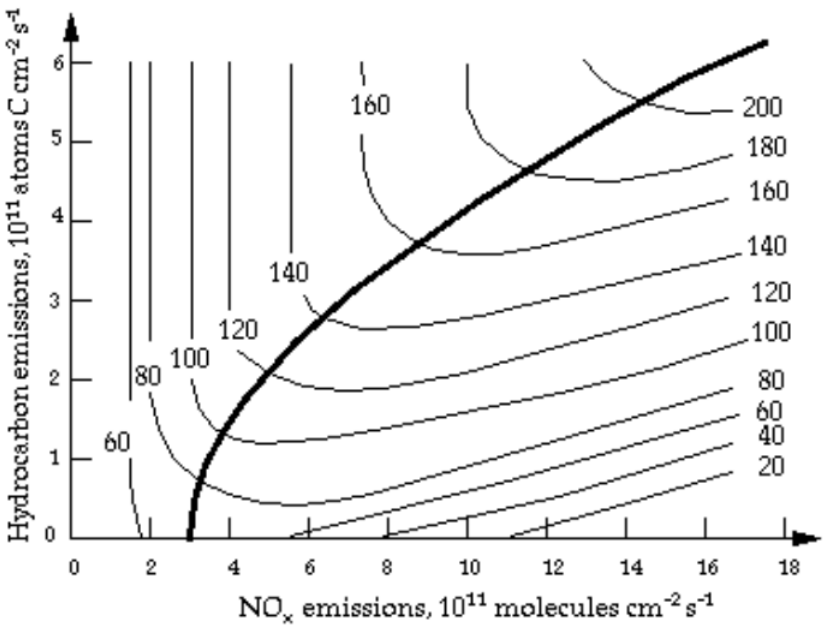

Fig. 1.1. From Jacob et al. (1999): "Ozone concentrations (ppbv) simulated by a regional photochemical model as a function of NO_x and hydrocarbon emissions. The thick line separates the NO_x-limited (top left) and hydrocarbon-limited (bottom right) regimes. Adapted from Sillman, S., et al., J. Geophys. Res., 95, 1837–1852, 1990."

limited conditions (right of the dividing line), ozone production increases with rising VOC emissions but diminishes with increased emissions of NO_x.

1.2.2 Isoprene oxidation

Isoprene oxidation chemistry is complex and comprises nearly 2000 individual photochemical reactions (Jenkin et al., 2015). Presented here is a simplified description of the chemistry, with a visual representation of the first generation of product formation provided in Fig. 1.2. As illustrated, addition of the OH radical results in the generation of isoprene hydroxy peroxy radicals ($ISOPO_2$), which may experience

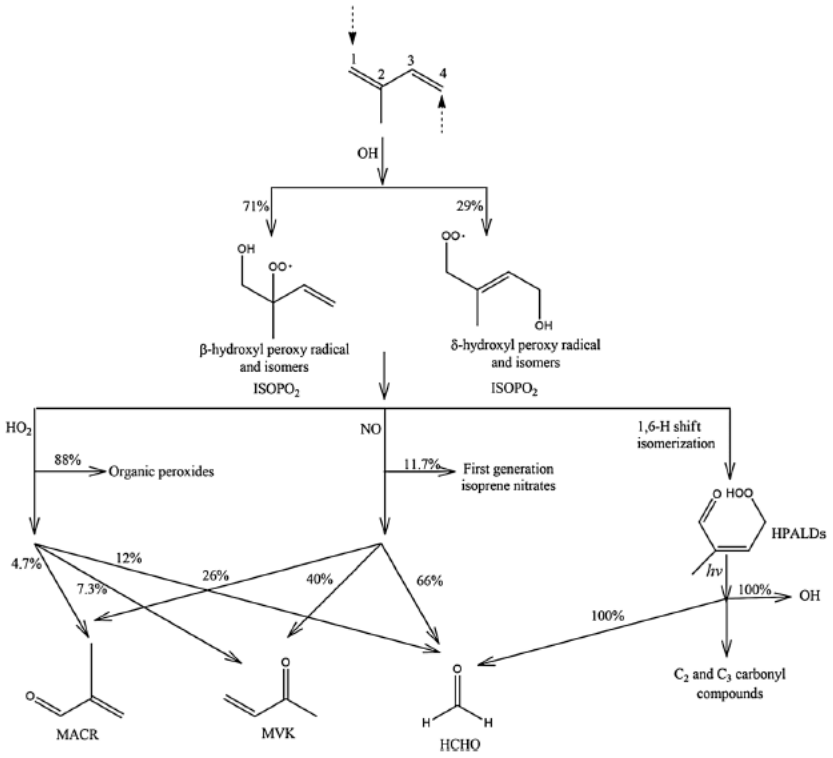

Fig. 1.2. From Mao et al. (2013b): "Schematic of the first stage of the isoprene oxidation mechanism initiated by OH."

different fates depending on conditions for NO_x. In the absence of NO_x, $ISOPO_2$ may react either with HO_2 or RO_2, or it may isomerize. Reaction of $ISOPO_2$ with HO_2 mainly produces isoprene hydroperoxides (ISOPOOH) (Paulot et al., 2009b), while reaction with RO_2 (not shown) mainly produces small oxygenated VOCs such as methyl vinyl ketone (MVK), methacrolein (MACR), and formaldehyde (HCHO) (Saunders et al., 2003). Isomerization of $ISOPO_2$ proceeds by intramolecular hydrogen transfer, specifically via either 1,6-H or 1,5-H shift (Da Silva et al., 2010; Peeters et al., 2009). The 1,6-H shift produces hydroperoxy aldehydes (HPALD), which photolyze to form small VOCs and regenerate OH (Crounse et al., 2011; Peeters and Müller, 2010; Peeters et al., 2014; Wolfe et al., 2012), while the 1,5-H shift (not shown) forms an

unstable intermediate that degrades to form MVK, MACR, and HCHO (Peeters et al., 2014; Peeters and Müller, 2010). In the presence of NO_x, $ISOPO_2$ favors reaction with NO to form MVK, MACR, and HCHO (Paulson and Seinfeld, 1992), with a minor channel leading to the production of organic nitrates (ISOPN) (Paulot et al., 2009a). The high-NO_x reaction pathway for $ISOPO_2$ results in the net conversion of NO to NO_2, which promotes production of tropospheric ozone.

Formaldehyde is a small oxygenated VOC that is produced in high yield throughout the isoprene cascade. This species is a major product of isoprene oxidation, not only from the first generation of product formation, but also from the subsequent chemistry of other isoprene oxidation products such as MVK and MACR (Tuazon and Atkinson, 1990). Like ozone production, the formation of HCHO through the oxidation of isoprene is highly dependent on the abundance of NO_x (Wolfe et al., 2016a). Enhanced production of both HCHO and ozone in the presence of NO_x distinguishes HCHO as a potential photochemical tracer for tropospheric ozone production. Furthermore, as shown in R1.18–R1.20, the primary pathways for daytime HCHO decomposition lead to the formation of CO and HO_2:

$$HCHO + h\nu \rightarrow CO + H_2 \quad \text{(R1.18)}$$

$$HCHO + h\nu + O_2 \rightarrow CO + 2\,HO_2 \quad \text{(R1.19)}$$

$$HCHO + OH + O_2 \rightarrow CO + HO_2 + H_2O \quad \text{(R1.20)}$$

In the presence of NO_x, both CO and HO_2 contribute directly to the production of tropospheric ozone, as described in the previous section. The photochemical behavior of HCHO thus provides valuable insight into atmospheric isoprene oxidation and its impacts on surface ozone.

1.3 Measurements

This body of work makes substantial use of measurements from the Southeast Nexus (SENEX) aircraft campaign, which provides *in situ* observations of isoprene, ozone, HCHO, and other relevant species. The mission, led by the National Oceanic and Atmospheric Administration (NOAA), was conducted in June and July of 2013 and utilized the WP-3D payload to sample atmospheric composition across the Southeast US, with flight tracks as shown in Fig. 1.3a. This region experiences high emissions of isoprene during the summer (Fig. 1.3b) and thus provides a favorable environment for characterizing the atmospheric oxidation of isoprene. The atmosphere in the Southeast United States is also highly variable in NO_x emissions, which are low in rural regions such as the Ozark mountains and high near urban centers (Fig. 1.3c). This variability provides a unique opportunity to map out the sensitivity of isoprene oxidation and ozone production across a range of NO_x conditions.

Measurements of HCHO were collected by the In Situ Airborne Formaldehyde (ISAF) instrument during SENEX (Cazorla et al., 2015). The ISAF instrument samples ambient air at a fequency of 10 Hz and records HCHO measurements at 1 Hz. The accuracy of the instrument is ±10% against calibration with a standard, and the 1-σ precision is 15 ppt s^{-1}. This work also utilizes *in situ* measurements of several other trace gases, including ozone, NO_x, isoprene, and other relevant VOCs. Although multiple measurements of certain species were collected during SENEX, this work primarily utilizes measurements of ozone and NO_x obtained via chemiluminescence (CL) detection (accuracy = ±2%; ±5%) (Ryerson et al., 2000, 1999, 1998), and measurements of isoprene obtained via proton-transfer-reaction mass spectrometry

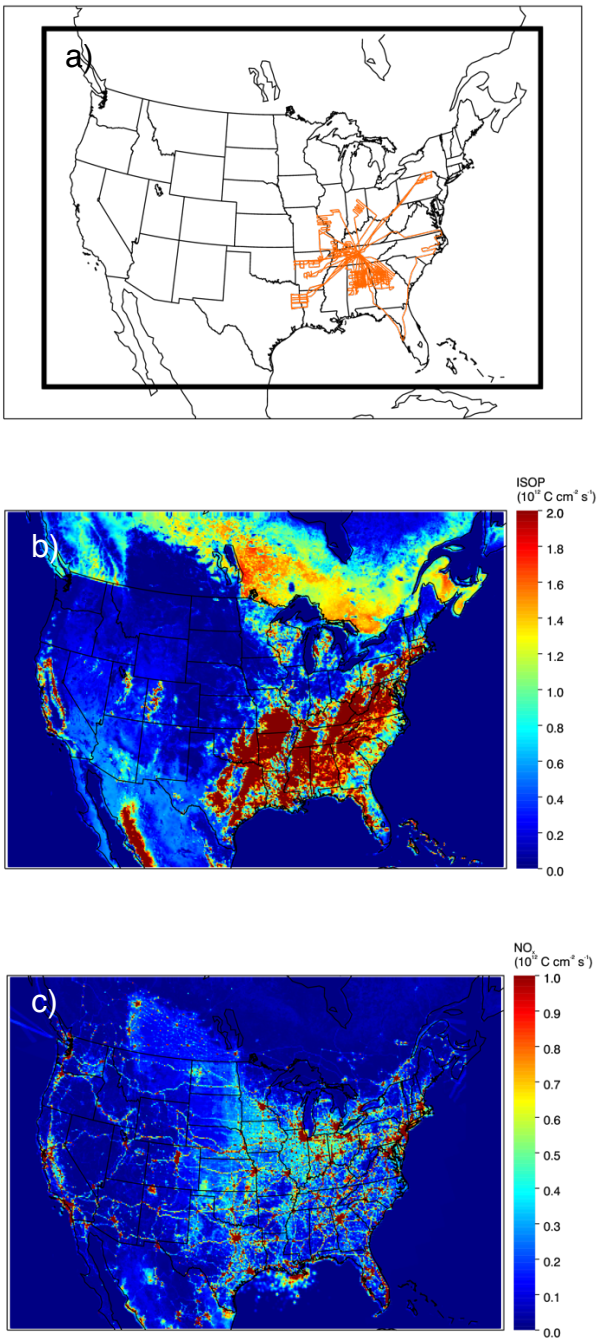

Fig. 1.3. a) Flight tracks of the WP-3D aircraft from the SENEX campaign. The thick black border denotes domain boundaries for the CONUS 2013 regional modeling platform. b) Isoprene area emissions (10^{12} C cm^{-2} s^{-1}) generated using BEIS version 3.61, averaged for the hours of 8–20 EDT across days between May 21 and July 15 of 2013. Note that the color bar saturates at 2×10^{12} C cm^{-2} s^{-1}. c) NO_x area emissions (10^{12} C cm^{-2} s^{-1}) based on the 2011 NEI version 2 platform "ek," averaged for the hours of 8-20 EDT across days between May 21 and July 15 of 2013. Note that the color bar saturates at 1×10^{12} C cm^{-2} s^{-1}.

(PTR-MS; ±25%) (de Gouw and Warneke, 2007). *In situ* measurements such as these are highly resolved in space and time, allowing for their photochemical relationships to be explored in great detail (Wolfe et al., 2016a), which is critical to elucidating the intricacies of atmospheric isoprene oxidation and tropospheric ozone production. Further information regarding SENEX instrumentation is provided as necessary throughout the following chapters.

1.4 Models

This work utilizes two different types of computer model to simulate the atmospheric oxidation of isoprene. One is a zero-dimensional photochemical box model that I helped develop, called the Framework for 0-D Atmospheric Modeling (F0AM) (Wolfe et al., 2016b). Within the context of this body of work, F0AM is mainly used to simulate atmospheric isoprene oxidation along the SENEX flight tracks. The model is constrained to observations of ozone, NO_x, isoprene, and other species important to isoprene oxidation or production of HCHO. The F0AM model in particular offers several different gas-phase chemical mechanisms for model implementation – including recent versions of the Carbon Bond (CB) mechanism (Hildebrandt Ruiz and Yarwood, 2013; Yarwood et al., 2005), the Master Chemical Mechanism (MCM) (Jenkin et al., 2015, 1997; Saunders et al., 2003), and the GEOS-Chem mechanism (Fisher et al., 2016; Kim et al., 2015; Mao et al., 2013b; Marais et al., 2016; Travis et al., 2016) – and otherwise supports mechanism customization, which provides an ideal environment for testing different representations of isoprene oxidation chemistry.

The other model applied in this work is the Comprehensive Air Quality Model with Extensions (CAMx) (http://www.camx.com), a three-dimensional regional chemical transport model that has been approved by the EPA for use in developing SIPs. In support of my research objectives, I developed a platform for CAMx to simulate atmospheric composition across the continental US, with domain boundaries as shown in Fig. 1.3a, from May 21 through July 15 of 2013. The CAMx model integrates atmospheric chemistry with several other important atmospheric processes such as meteorology, emissions, mixing, transport, and deposition. This platform thus provides opportunities to test different representations of isoprene emissions, in addition to isoprene chemistry. Moreover, the CAMx model in particular provides valuable tools for characterizing and quantifying simulated tropospheric ozone production, which are designed to support SIPs, but are applied in this work to assess how model representations of isoprene oxidation impact the simulation of surface ozone. Further information regarding the F0AM and CAMx models, as well as descriptions of my personal contributions to model development, are provided in Chapter 2. Additional details pertaining to individual research simulations are provided as necessary throughout the remaining chapters.

1.5 Outline

Subsequent chapters in this body of work describe how the SENEX measurements, as well as the F0AM and CAMx models, are applied to conduct a quantitative analysis of atmospheric isoprene oxidation. Chapter 2 describes my role in preparing both models to meet this objective. Chapter 3 describes my application of the

F0AM box model to the simulation of atmospheric isoprene oxidation along the SENEX flight tracks. Several gas-phase chemical mechanisms are implemented within the box model framework to test different representations of isoprene oxidation chemistry. Model simulations are evaluated using measurements of HCHO from SENEX, and recommendations are provided for improving HCHO production from isoprene oxidation. Chapter 4 describes my application of the CAMx regional model to the simulation of atmospheric composition across the continental US during the summer of 2013. Different representations of isoprene chemistry and emissions are incorporated into sensitivity simulations, which are evaluated against SENEX measurements of several species, including HCHO, isoprene, and ozone. The CAMx tools for ozone production analysis are applied to determine how model representations of atmospheric isoprene oxidation impact the simulation of surface ozone. Recommendations for improving isoprene emissions are provided, and implications for surface ozone management strategies are discussed. Finally, Chapter 5 summarizes this work and poses suggestions for future studies.

Chapter 2: Model Development

This chapter describes my efforts to prepare the F0AM and CAMx models for analysis of atmospheric isoprene oxidation. A description of each model is provided, along with explanations of my contributions to its model development and my role in related modeling applications. My contributions to the development of the F0AM model are substantial, and I am listed as the second author on the corresponding model description paper by Wolfe et al. titled "The Framework for 0-D Atmospheric Modeling (F0AM) v3.1," which was published on 20 September 2016 in Volume 9 of *Geoscientific Model Development*, pages 3309–3319. Applications using the F0AM model include Chapter 3 of this dissertation, and have also led to my co-authorship of three other scientific articles: (1) "Quantifying sources and sinks of reactive gases in the lower atmosphere using airborne flux observations" by Wolfe et al., published on 28 September 2015 in Volume 42, Issue 9 of *Geophysical Research Letters*, pages 8231–8240, (2) "Formaldehyde production from isoprene oxidation across NO_x regimes" by Wolfe et al., published on 2 March 2016 in Volume 16 of *Atmospheric Chemistry and Physics*, pages 2597–2610, and (3) "Multidecadal trends in ozone and ozone chemistry in the Baltimore-Washington Region" by Roberts et al., in preparation. My contributions to the CAMx model are described and applied in Chapter 4, which is also in preparation for publication.

2.1 F0AM

2.1.1 Description

The Framework for 0-D Atmospheric Modeling (F0AM), originally developed by Glenn Wolfe in the form of the University of Washington Chemical Model (UWCM), is a simple box model that simulates photochemistry at a single point in space (Wolfe et al., 2016b). Provided initial photochemical and meteorological conditions, as well as a chemical mechanism, the model solves a system of production and loss equations to predict the evolution of chemical composition over time. For any species *X*, the time evolution of its concentration [*X*] (molecules cm^{-3}) is described by a combination of reaction rates:

$$\frac{d[X]}{dt} = \sum_{i=1}^{n} f_i k_i G_i \tag{2.1}$$

where *f* is the stoichiometric coefficient (unitless) for each reaction *i*, *k* is the reaction rate constant (for bimolecular reactions: cm^3 $molecule^{-1}$ s^{-1}), *G* is the product of reactant concentrations (for bimolecular reactions: $molecules^2$ cm^{-6}), and *n* is the total number of reactions. Though primarily focused on chemistry, the F0AM model also applies a simple dilution function to all species to account for physical removal from the system. The effect of dilution on the rate of change of species concentration is parameterized as follows:

$$\frac{d[X]}{dt} = k_{\text{dil}}([X]_{\text{b}} - [X]) \tag{2.2}$$

where k_{dil} is the dilution rate constant (s^{-1}) and $[X]_{\text{b}}$ is a prescribed background concentration (molecules cm^{-3}). Equation 2.2 is incorporated into Equation 2.1, and the total rate of change is integrated over time to determine instantaneous species concentrations at specified intervals.

The major advantages of the F0AM box model stem from its simplicity and flexibility. The model's zero-dimensional approach simplifies the atmospheric system to a predominantly chemical basis, providing an ideal environment for exploring atmospheric chemistry. The model also provides a flexible platform for customizing simulations to support a wide range of applications. For example, F0AM offers three different photolysis settings. The first is a "bottom-up" technique, most appropriate for chamber study simulations, that calculates photolysis rates (or J-values; s^{-1}) as a function of wavelength (λ; nm), temperature (T; K), and pressure (P; torr), using literature-based cross sections (σ; cm^2 $molecule^{-1}$) and quantum yields (Φ; molecules $photon^{-1}$), mainly drawn from the kinetic data evaluations of the International Union of Pure and Applied Chemistry (IUPAC) (http://iupac.pole-ether.fr) and the Jet Propulsion Laboratory (JPL) (https://jpldataeval.jpl.nasa.gov), as well as an actinic flux spectrum (F; photons cm^{-2} s^{-1}) that must be provided by the user:

$$J = \int_{\lambda_{\min}}^{\lambda_{\max}} \phi(\lambda,T,P)\sigma(\lambda,T,P)F(\lambda)d\lambda \quad (2.3)$$

Photolysis rates may also be calculated as a function of solar zenith angle (SZA) using a parameterization of the following form:

$$J = I * \cos(\mathrm{SZA})^m * \exp(-n * \sec(\mathrm{SZA})) \quad (2.4)$$

where I, m, and n are constants optimized for each photolytic species based on radiative transfer simulations for clear sky conditions on 1 July at 45° N latitude and 0.5 km altitude (Jenkin et al., 1997). This parameterization is based on a single solar spectrum and does not capture full atmospheric variability due to albedo, overhead ozone column, and other radiative transfer considerations. The third option determines J-values using lookup tables varying in SZA, overhead ozone, albedo, and altitude. The

lookup tables are derived from simulations of the Tropospheric Ultraviolet and Visible (TUV) radiative transfer model (https://www2.acom.ucar.edu/modeling/tropospheric-ultraviolet-and-visible-tuv-radiation-model), which uses the same literature cross sections and quantum yields from the bottom-up method in conjunction with a solar actinic flux spectrum. A diel solar cycle in SZA can be applied to the last two photolysis options, which is useful for simulations supporting ground and aircraft field studies. Beyond photolysis, options are also available to customize initial conditions, constraint behavior, integration parameters, simulation sequences, and model output.

The F0AM modeling platform is also designed to enable maximum flexibility in the driving chemistry. For example, F0AM comes standard with several preset gas-phase chemical mechanisms for model implementation, including Carbon Bond (CB) mechanism variants CB05 (Yarwood et al., 2005) and CB6r2 (Hildebrandt Ruiz and Yarwood, 2013; Yarwood et al., 2010), versions 3.2 and 3.3.1 of the Master Chemical Mechanism (MCM) (Jenkin et al., 2015, 1997; Saunders et al., 2003), version 2 of the Regional Atmospheric Chemistry Mechanism (RACM) (Goliff et al., 2013), and version 9-2 of the GEOS-Chem mechanism (Mao et al., 2013b) enhanced with some post-release updates to isoprene oxidation (Fisher et al., 2016; Kim et al., 2015; Marais et al., 2016; Travis et al., 2016). All six mechanisms define the reactions characteristic of tropospheric ozone-NO_x-VOC chemistry and provide corresponding reaction rate constants, which are usually drawn from the IUPAC or JPL kinetic data compendia. Differences in age and complexity (Table 2.1) influence variety among mechanisms, with tradeoffs between level of detail and computation time (Fig 2.1). The CB mechanisms, which are designed to favor computational efficiency, are representative

Table 2.1 Preset gas-phase chemical mechanisms available for implementation in F0AM.

Mechanism	Species	Reactions	Reference
CB05[a]	53	156	Yarwood et al., 2005
CB6r2[a]	77	216	Hildebrandt Ruiz and Yarwood, 2013
RACM2	121	363	Goliff et al., 2013
GEOS-Chem[b]	171	505	Mao et al., 2013b
MCMv3.2	5733	16940	Saunders et al., 2003; Jenkin et al., 1997
MCMv3.3.1	5832	17224	Jenkin et al., 2015

[a]Updated for consistency with CAMx v6.40 documentation.
[b]Updated for consistency with Kim et al. (2015), Fisher et al. (2016), Marais et al. (2016), and Travis et al. (2016).

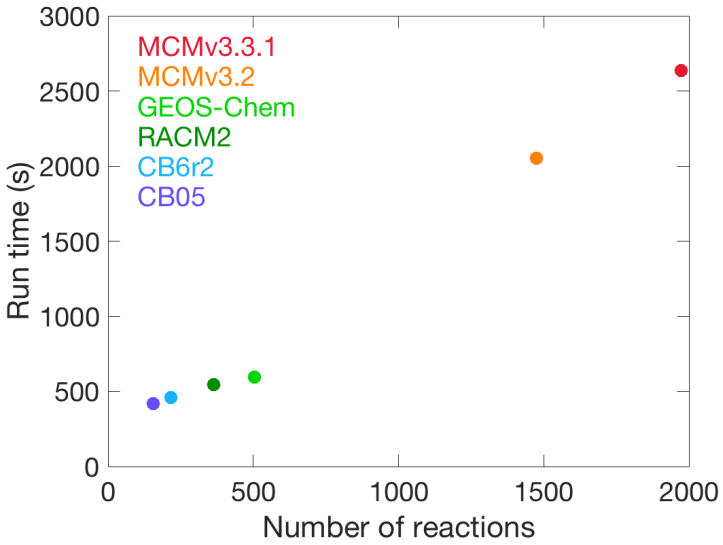

Fig. 2.1. Model run time (s) versus number of reactions for each of the preset mechanisms available in F0AM. Run time is calculated for a typical aircraft campaign modeling scenario, as described in Section 2.1.1, with 263 discrete points each integrated for 72 hours. Isoprene subsets are taken to simplify the MCM down to 1476 reactions for v3.2 and 1974 reactions for v3.3.1. Run times for the full MCM mechanisms are estimated between 60,000–70,000 s, based on extrapolation from a single point.

of the chemistry commonly used in regional air quality models (Canty et al., 2015; Goldberg et al., 2016). In contrast, the MCM mechanisms aim instead for completeness and provide benchmarks for the optimization of less detailed mechanisms (Jenkin et al., 2015). In addition to the preset mechanisms, F0AM also provides options for chemistry customization, with opportunities to adjust existing mechanisms and create original mechanisms from scratch.

Though the F0AM model offers many advantages, it also has limitations. The zero-dimensional modeling approach, for example, inherently precludes explicit representation of horizontal or vertical transport. This, in turn, limits the representation of all processes that rely on transport, including meteorology, emissions, and deposition. The F0AM model requires that all meteorological variables must be initialized explicitly. Though a simple function for physical removal is provided to simulate deposition/entrainment/advection (Equation 2.2), further representation of emissions or deposition must be developed by the user. Besides these inherent limitations, F0AM is also limited in its support for heterogenous chemistry. Provided examples lay a groundwork for the user to construct heterogeneous reactions and rate information, which must be compatible with Equation 2.1. However, no standard heterogenous mechanism is yet available.

My experience using the F0AM model is exclusively in support of aircraft field studies. In a typical model setup for such an application, meteorological and photochemical conditions are initialized with constant values or constrained to available aircraft observations. Photolysis rates may also be set or constrained, but otherwise must be calculated using one of the three photolysis options described above. Because each observation is defined by a unique time, location, and altitude, it is most appropriate to select the third photolysis option, which applies lookup tables that account for such variables. The lookup tables also require estimates for overhead ozone column and surface albedo, which should be set to values that correspond with the model domain: I use 300 DU and 0.05, respectively, to represent the summertime southeast US. Calculated photolysis rates may then be scaled to constrained rates. For most aircraft applications, parameterized J-values are scaled using observed $J(O^1D)$

and $J(NO_2)$ to account for variations in overhead ozone, surface albedo, and cloud cover. This scaling procedure is accomplished through the application of a multiplicative factor, computed as the ratio of the sum of parameterized $J(O^1D)$ and $J(NO_2)$ to the sum of the observed values. Since the driving photolytic source in this case would be the sun, diel solar cycle mode should be applied to ensure that J-values evolve with SZA over time. Any preset or customized gas-phase photochemical mechanism may be selected to provide the reaction and rate constant information needed for integration, but the total integration time should be optimized to ensure that the system achieves photochemical steady state conditions, which usually requires at least 72 hours (i.e., three complete diel cycles) of integration time. The dilution constant should be set to approximate physical removal from the system – this constant is typically set to 1/86400 s^{-1} to ensure that the lifetime of each species is no longer than 24 hours – though sensitivity tests have confirmed that my simulations are not significantly affected by this parameter. For an aircraft flight or campaign, each discrete set of observations should be simulated independently, though this can be accomplished in a single batch run. An example model setup script for an aircraft field study application, as described above, is provided in Appendix A. Model output includes instantaneous mixing ratios (ppb) for all species and rates for all reactions (ppb s^{-1}) specified by the selected chemical mechanism.

The F0AM model, user's guide, tutorial, and several example scripts are available for download at: https://sites.google.com/site/wolfegm/models. All provided software is programmed for use with the Matrix Laboratory (MATLAB) computing environment, available for download at: https://www.mathworks.com/products/matlab.html. Due to its accessibility, flexibility, and ease of use, F0AM and

its prior manifestation UWCM have already been used to support several research studies, with applications involving ozone production (Baier et al., 2017; Benish et al., 2019; Roberts et al., 2019; Romer et al., 2018), VOC oxidation (Kaiser et al., 2015; Kim et al., 2015; Marvin et al., 2017; Wolfe et al., 2016a, 2015, 2014), biomass burning (Anderson et al., 2016; Busilacchio et al., 2016; Kumar et al., 2018; Müller et al., 2016), and halogen chemistry (Riedel et al., 2014).

2.1.2 Contributions

My major contributions to F0AM relate to the development of its preset gas-phase chemical mechanisms. Though the code for the MCMv3.2 mechanism was carried over from the UWCM, I added MCMv3.3.1. This task was streamlined by existing model software that builds on the native FACSIMILE-formatted code, available for download from: http://mcm.leeds.ac.uk/MCM/. I collaborated with other developers to update photolysis and complex rate constant parameterizations from MCMv3.2 to MCMv3.3.1. I also contributed substantially to the formatting and revision of codes for the RACM2 and CB05 mechanisms, which were originally developed by other colleagues. Last but not least, I programmed the CB6r2 mechanism in its entirety and formatted it for compatibility with F0AM. Existing codes for the CB6r2 mechanism were not suitable for automation, so this task was completed manually, adapting from CB05 where possible. The full mechanism includes a base script that defines all 77 species and 216 reactions, as well as one script for the assignment of photolysis rates and another script for the parameterization of complex reaction rate constants, such as Troe-type expressions. All three scripts accompany the standard F0AM model and are included in the package that is available for download

from: https://sites.google.com/site/wolfegm/models. These scripts, truncated where appropriate, are also presented in Appendix B for reference.

Besides my work with the chemical mechanisms, I contributed to F0AM model development in other ways. For example, I supplied code to enhance the output visualization program PlotRatesAvg.m, which plots average production and loss rates for a specified species and population of model points. The program offers a selection of two different plot types: horizontal bar chart or pie chart. My code, specifically, introduced the averaging calculations and laid the groundwork for the pie plotting module. Examples of plots constructed with this program are shown in Fig. 2. Panel a) demonstrates the horizontal bar chart plot type with production on the right and loss on the left, while panel b) demonstrates the pie chart plot type with production on the left and loss on the right. I was also instrumental to the development of the simulation example ExampleSetup_FlightSS.m, which is typical of an aircraft field study application run to diel steady state. This example constrains to 60-second average aircraft observations from a single flight from the Southeast Nexus (SENEX) campaign (Warneke et al., 2016), and can be configured to run using any of the preset chemical mechanisms that are provided with F0AM. I compiled the data for this example and supplied the base code for the corresponding setup script. Fig. 2.3 shows six of the ten plots that are produced when this example is executed with CB6r2 as the driving mechanism. These plots demonstrate the model's various post-processing programs, including PlotRatesAvg.m. In addition to these individual specified contributions, I have also assisted with universal benchmarking and debugging throughout the evolution of the model, since UWCM version 2.2.

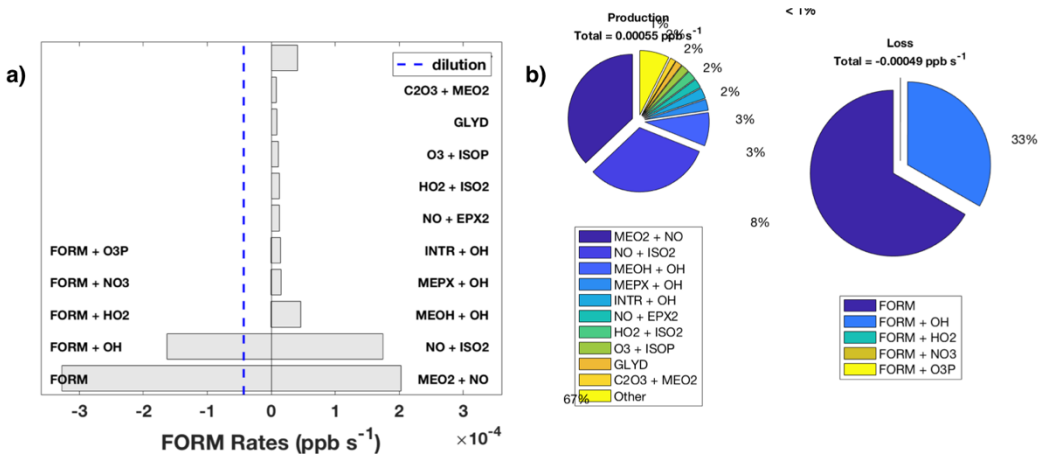

Fig. 2.2. Example plots constructed with PlotRatesAvg.m. Panel a) demonstrates the horizontal bar chart plot type with production on the right and loss on the left, while panel b) demonstrates the pie chart plot type with production on the left and loss on the right. Here, both plots quantify average production and loss rates output for HCHO (i.e., 'FORM'), from a simulation representative of a typical aircraft field study application, as described in Section 2.1.1. This particular simulation applies the CB6r2 mechanism and mimics a flight over Atlanta conducted by the WP-3D aircraft during SENEX on 12 June 2013, which provides a sample population of 263 model points for averaging.

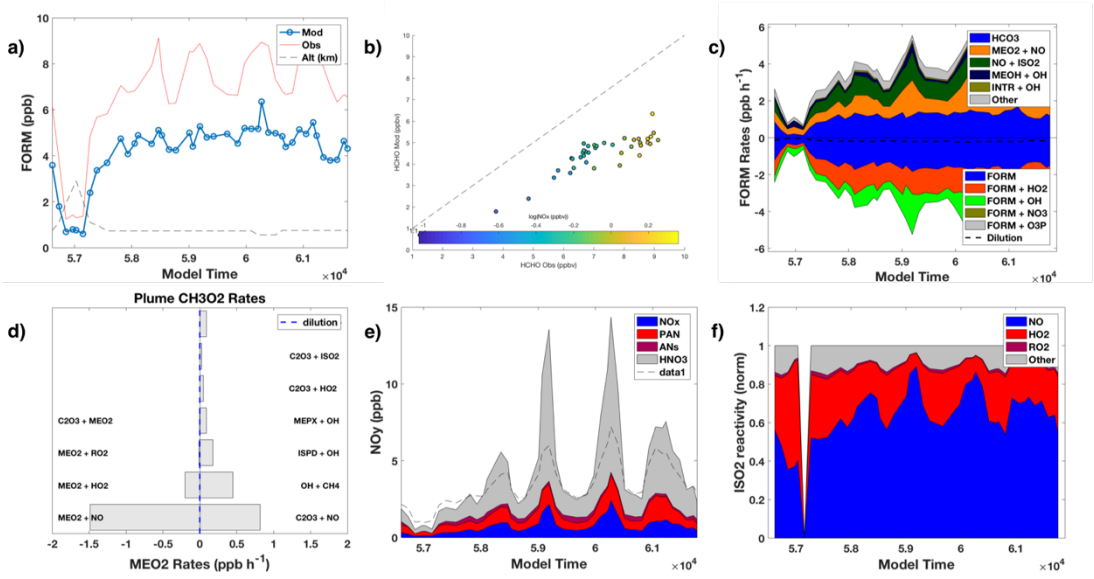

Fig. 2.3. Six of the ten plots produced from the execution of ExampleSetup_FlightSS.m, configured to run using the CB6r2 chemical mechanism. This simulation demonstrates an example model setup, typical of an aircraft field study application run to diel steady state. Specifically, it mimics part of a flight over Atlanta conducted by the WP-3D aircraft during SENEX on 12 June 2013. Panels a)–f) are constructed using the model's post-processing software, showing a) species concentrations, b) model-measurement scatter, c) cumulative production and loss rates, d) average production and loss rates, e) lumped species concentrations, and f) reactivities.

My contributions to the development of the F0AM model were acknowledged by my appointment as the second author on the model description paper by Wolfe et al., which was titled "Framework for 0-Dimensional Atmospheric Modeling (F0AM) v3.1" and published on 20 September 2016 in Volume 9 of *Geoscientific Model Development*, pages 3309–3319. As co-author, I assisted in revising the corresponding manuscript, as well as the written supplementary materials, which facilitated the publication and official public release of F0AM version 3.1.

2.1.3 Applications

In addition to the indirect support imparted via model development, I have also supported various research applications of the F0AM model directly, by running simulations and generating results. For example, I used F0AM version 3 to lead a mechanism inter-comparison study, which comprises Chapter 3 of this dissertation. There, I inter-compare and evaluate isoprene oxidation chemistry among the preset mechanisms CB05, CB6r2, GEOS-Chem, MCMv3.2, and MCMv3.3.1. Each mechanism is implemented separately in F0AM to simulate isoprene chemistry during the SENEX aircraft campaign. In each simulation, initial conditions are constrained to relevant *in situ* observations from SENEX, and model setup follows the description provided in Section 2.1.1. My analysis utilizes various model output, including instantaneous mixing ratios and reaction rates, which is inter-compared between mechanisms and evaluated using *in situ* observations of HCHO. My results inspire recommendations to improve HCHO production from isoprene oxidation in the CB6r2 chemical mechanism, and the corresponding modifications are presented as an updated

version called 'CB6r2-UMD,' which can be reproduced in F0AM or any model that allows such flexibility. Finally, I investigate how the recommended improvements to the isoprene chemistry affect simulated ozone production rates. Please refer to Chapter 3 for a complete description of this F0AM application and its publication information.

I have also provided F0AM/UWCM modeling support for research led by other colleagues. For example, I conducted a simulation with the UWCM version 2.2 to support a study by Wolfe et al. (2016a) titled "Formaldehyde production from isoprene oxidation across NO_x regimes." That study utilizes observations from SENEX to characterize the NO_x-dependence of isoprene oxidation and the impacts of that dependence on the production of HCHO. I contributed results from a UWCM simulation to provide insight into the representation of this NO_x-dependence in current gas-phase chemical mechanisms. The simulation is set up as described in Section 2.1.1, constrained to relevant observations from SENEX; however, because UWCMv2.2 precedes the addition of more complex photolysis functionalities, photolysis rates are determined using the MCM parameterization method, assuming clear-sky conditions. The MCMv3.3.1 mechanism is selected for implementation, because it is expected to present the most detailed, accurate, and up-to-date isoprene chemistry of the preset mechanisms available in UWCM or F0AM.

Results from this simulation are evaluated against SENEX observations and provide insight into modeling capabilities for representing the production of HCHO (and other species) from isoprene oxidation across NO_x regimes, as illustrated by several figures from the paper. Fig. 2.4b shows a simple scatter of HCHO simulated using UWCM (ppb) versus observed HCHO (ppb). A major-axis least-squares fit is applied to the scatter, with fitting parameters presented in the lower right-hand corner

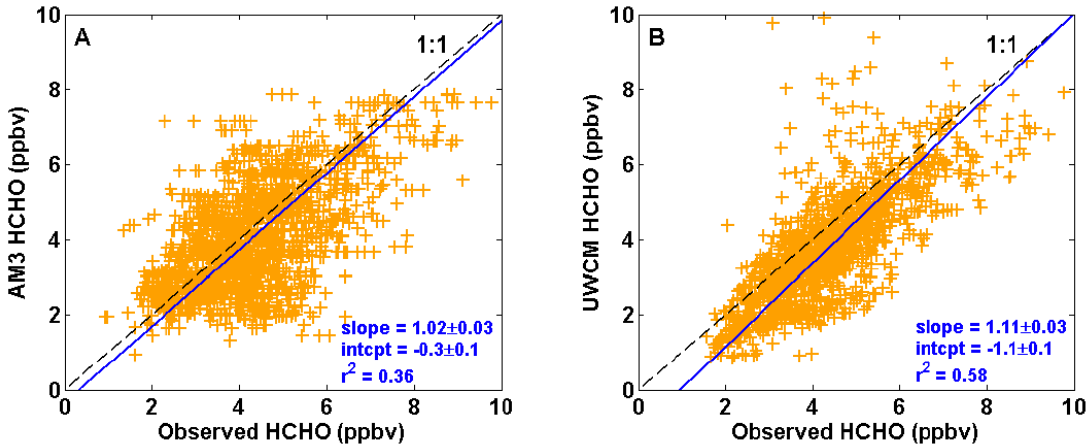

Fig. 2.4. From Wolfe et al. (2016a): "Comparison of observed and modeled HCHO mixing ratios for A) the AM3 global chemical transport model and B) the UWCM 0-D box model. Observations and model results are averaged/simulated at 1-minute resolution and filtered to only include daytime, boundary layer, non-biomass burning regions. Dashed lines represent the 1:1 correlation, and solid blue lines represent major axis least-squares fits. Corresponding slopes, intercepts and coefficients of determination (r^2) are also shown with their 1σ fitting uncertainty."

of the figure. Though the slope is greater than 1, the normalized mean bias is –15%, which suggests that the box model simulation tends to underestimate observed HCHO. Fig. 2.5 compares the NO_x-dependence of the relationship linking HCHO to emitted isoprene. Panel a) shows the slopes (ppb HCHO / ppb isoprene) and panel b) the intercepts (ppb) that define this chemical connection, presented as a function of NO_x (ppb). Observationally-derived results are represented by the blue line (mean) and shaded area (3σ standard deviation), with simulation results overlaid from the UWCM box model (black diamonds) and the atmospheric component (AM3) of the Geophysical Fluid Dynamics Laboratory (GFDL) coupled general circulation model (CM3; red circles) (Donner et al., 2011), which supplies its own unique gas-phase chemical mechanism (Mao et al., 2013a; Naik et al., 2013). This figure shows that both models successfully reproduce the NO_x-dependence of HCHO production from

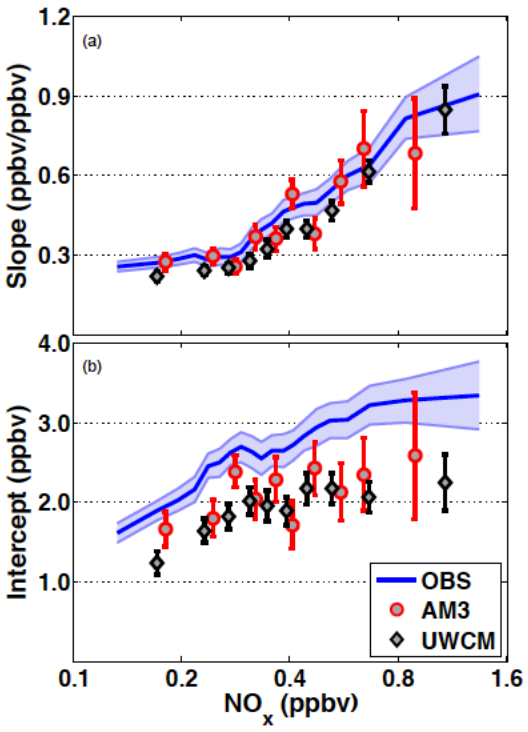

Fig. 2.5. From Wolfe et al. (2016a): "Comparison of observed and model-derived relationships between HCHO and initial isoprene versus NO_x. Slopes **(a)** and intercepts **(b)** are calculated as described in the [published] text. The observed values (blue line with shading) are the same as those shown in Fig. 3b–c. Symbols represent fit results for the global AM3 model (red circles) and the 0-D UWCM box model (black diamonds). Error bars denote 3σ fitting uncertainties."

isoprene oxidation, or the slope linking HCHO to initial isoprene; however, both also underestimate the intercept, or background HCHO, by 0.5–1 ppb. Fig. 2.6 illustrates the NO_x-dependences of production rates and branching ratios relevant to HCHO production from isoprene oxidation. Panel a) shows production (ppt s^{-1}) of HCHO (blue line and shading) and RO_2 (orange line and shading) as a function of NO_x (ppb), and panel b) shows the HCHO branching ratio (unitless) from the reaction of NO with various RO_2 (CH_3O_2 as the red dashed line; $ISOPO_2$ as the pink dashed line; weighted total RO_2 as the black solid line) as a function of NO_x (ppb). In this figure, production

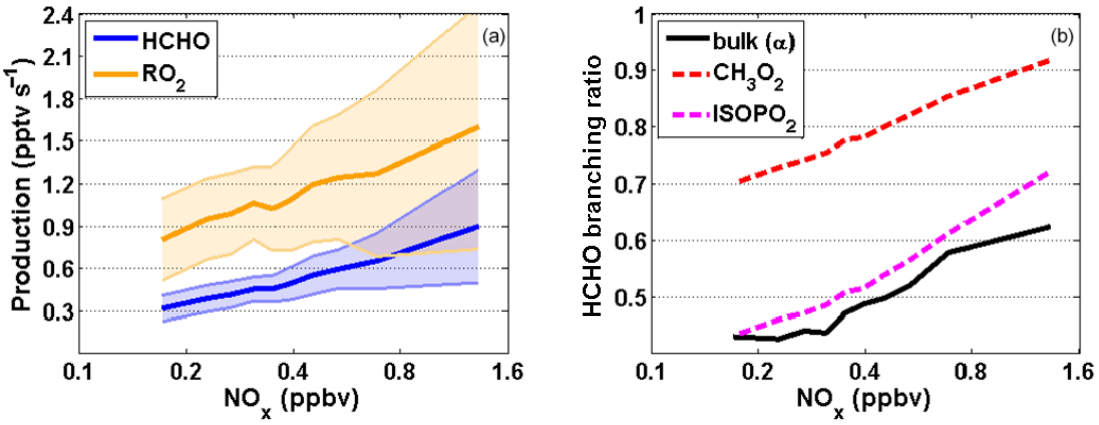

Fig. 2.6. From Wolfe et al. (2016a): "NO_x dependence of chemical properties related to HCHO production, extracted from the UWCM simulation of SENEX observations. **(a)** Production rates for HCHO (blue) and total RO_2 (orange). **(b)** Branching ratios for HCHO production weighted over all RO_2 (solid black line) and for several individual RO_2, including methyl peroxy radical (red) and total isoprene hydroxyperoxy radicals (magenta). All quantities are averaged over NO_x using 10 bins with equal numbers of points. In **(a)**, solid lines show the mean and shading is 1σ variability."

of HCHO increases as a function of NO_x by a factor of 3, driven by an increase in the production of RO_2 and the HCHO branching ratio with NO_x. Production of RO_2 is in turn dependent upon abundance of OH, so these results indicate that the characteristic NO_x-dependence of HCHO production from isoprene oxidation may be largely due to enhanced production of OH, which is a major conclusion of the study by Wolfe et al. (2016a). My contributions to the study are acknowledged with my appointment as co-author on its publication, which appeared in Volume 16 of the journal *Atmospheric Chemistry and Physics*, pages 2597–2610. As co-author, I also assisted in revising the corresponding manuscript and supplemental materials.

Similarly, I provided model results for another study by Wolfe et al. (2015) titled "Quantifying sources and sinks of reactive gases in the lower atmosphere using airborne flux observations." That study applies observations from the Studies of

Emissions and Atmospheric Composition, Clouds, and Climate Coupling by Regional Surveys (SEAC^{4}RS) aircraft campaign (Toon et al., 2016) to determine eddy covariance fluxes for certain species, namely isoprene, NO_x, ozone, and hydrogen peroxide (H_2O_2). These fluxes provide observational constraints on complex atmospheric processes, including emissions, deposition, entrainment, aerosol uptake, and gas-phase chemistry. The study discusses implications for each process in detail and utilizes the determined eddy covariance fluxes to quantify significant results. For example, based on the eddy covariance fluxes calculated for isoprene and H_2O_2, the study estimates average concentrations of OH ($(1.3 \pm 0.3) \times 10^6$ molecules cm^{-3}) and HO_2 ($(6 \pm 1) \times 10^8$ molecules cm^{-3}) for a flight from the SEAC^{4}RS aircraft campaign, which were not measured directly. I estimated the flight average concentrations of the same species via box model simulation, in order to provide a basis for comparison.

For this application, I conducted five simulations with the UWCM version 2.2. All five simulations were constrained to 10-second average observations from a flight over the forested Ozark Mountains that was performed as part of the SEAC^{4}RS aircraft campaign; model setup generally follows the description in Section 2.1.1. Again, this early model version precedes more complex photolysis treatments, so J-values are calculated using the MCM parameterization method; however, many J-values are constrained to observations, and the rest are scaled to observed J(NO_2), in order to account for cloud cover. The base case simulation implements the MCMv3.2 gas-phase chemical mechanism, with literature-based updates to the isoprene oxidation chemistry that optimize:

1. Rate constants for oxidation of isoprene nitrates (ISOPN) and isoprene epoxydiols (IEPOX) (Bates et al., 2014; Lee et al., 2014)

2. Formation and yields of second-generation ISOPN (Paulot et al., 2009a)
3. Reaction rates and products for the oxidation of isoprene oxidation products glycolaldehyde (GLYD) and methylglyoxal (MGLYOX) (Baeza-Romero et al., 2007; Butkovskaya et al., 2006)
4. Inter-conversion of isoprene peroxy radicals ($ISOPO_2$) (Archibald et al., 2010a), their isomerization via 1,5-H and 1,6-H shift (Crounse et al., 2011; Da Silva et al., 2010; Peeters et al., 2009; Peeters and Müller, 2010), and subsequent chemistry (Wolfe et al., 2012)

Four sensitivity simulations explore the sensitivity of simulated OH, HO_2, and RO_2 to faster $ISOPO_2$ isomerization (M1), a 50% reduction in the isoprene oxidation rate (M2), and a factor of 2 decrease (M3a) or increase (M3b) in the physical loss rate (M3a–b).

From each simulation, I extracted flight average concentrations of OH (10^6 molecules cm^{-3}), as well as HO_2 and RO_2 (10^8 molecules cm^{-3}), for incorporation into Table 2.2, which appears in the study's publication. This table also includes the inferred estimates for OH and HO_2 from the eddy covariance flux calculations and estimates for the same species extracted from a simulation of the GEOS-Chem three-dimensional global chemical transport model, run at 25 × 25 km^2 resolution (Wang et al., 1998). The table shows that the UWCM simulations and flux derivations agree within stated 2σ uncertainties for OH, while GEOS-Chem underestimates both. However, GEOS-Chem matches the flux derivation for HO_2 almost exactly, while the UWCM simulations are consistently high. Simulated only with UWCM, RO_2 is a factor of ~1.5 higher than HO_2. From the UWCM sensitivity simulations, we deduce that simulated OH responds noticeably (50%) only to changes in the rate of isoprene oxidation (M2). Simulated HO_2 and RO_2 respond to all considered adjustments

Table 2.2. From Wolfe et al. (2015): "Comparison of HO_x concentrations calculated from flux divergence of isoprene (OH) and H_2O_2 (HO_2) with modeled concentrations from the GEOS-Chem global chemical transport model and the 0-D University of Washington Chemical Model (UWCM). Total RO_2 concentrations from the box model are also shown. Units for OH are 10^6 molecules cm^{-3}, and units for HO_2 and RO_2 are 10^8 molecules cm^{-3}. Uncertainties for flux-derived concentrations represent 2σ errors propagated from fits to flux profiles. Model-derived concentrations and uncertainties represent means and 2σ variability averaged over the first three flight legs. UWCM simulations include the base case with default MCM v3.2 chemistry and slow $ISOPO_2$ isomerization and four sensitivity simulations: faster $ISOPO_2$ isomerization (M1), reaction rate constant for OH + isoprene reduced by 50% to mimic reactant segregation (M2), and the physical loss rate constant reduced (M3a) or increased (M3b) by a factor of 2."

Species	Flux	GEOS-Chem	UWCM (base)	UWCM (M1)	UWCM (M2)	UWCM (M3a)	UWCM (M3b)
OH	1.3 ± 0.3	0.45 ± 0.07	1.0 ± 0.4	1.0 ± 0.4	1.5 ± 0.6	1.0 ± 0.4	1.0 ± 0.4
HO_2	5.8 ± 1.0	5.8 ± 0.4	6.6 ± 0.6	6.9 ± 0.6	6.9 ± 0.6	7.0 ± 0.7	6.3 ± 0.6
RO_2	---	---	10.4 ± 0.9	10.6 ± 1.0	10.0 ± 0.9	10.8 ± 1.0	10.1 ± 0.9

(1–8%); however, only a factor of 2 increase in the physical rate loss constant (M3b) successfully brings the simulation into agreement with the flux calculations. Reasonable agreement with the UWCM simulations lends confidence to the eddy covariance flux calculations, which comprise the principal methods employed in the study. My contributions to the study are acknowledged with my appointment as co-author on the publication by Wolfe et al. (2015), which appeared in Volume 42, Issue 9 of the journal *Geophysical Research Letters*, pages 8231–8240. As co-author, I contributed descriptions of the UWCM simulations to the manuscript, and I assisted with the revision of all supporting materials.

Finally, I provided informal training and guidance in using the F0AM model to colleagues at the University of Maryland, who apply the model to study a variety of research problems. One of these colleagues is Sandra Roberts from the Department of Chemistry and Biochemistry, who uses the F0AM model to study trends in ozone,

ozone precursors, and ozone production in Baltimore and Washington DC over time. She is preparing her work for publication under the title "Multidecadal trends in ozone and ozone chemistry in the Baltimore-Washington Region" and has acknowledged my assistance with the F0AM model by appointing me as one of her co-authors. I have also collaborated with Sarah Benish from the Department of Atmospheric and Oceanic Science, who uses F0AM to study ozone production in China.

2.2 CAMx

2.2.1 Description

The Comprehensive Air Quality Model with Extensions (CAMx; http://www.camx.com) is a gridded three-dimensional chemical transport model designed to predict variations in atmospheric composition across space and time (Ramboll Environ, 2018). The model implements the continuity equation, which represents all sources and sinks that influence species concentration [X] (μmol m^{-3} for gases; μg m^{-3} for aerosols) over time, at each model grid point. Processes represented in the continuity equation include horizontal advection, vertical advection, horizontal and vertical diffusion, emission, dry deposition, wet deposition, chemical production, and chemical loss. For the chemical rates, species concentrations are converted to units of molecules cm^{-3}, which allows for rate expression following Equation 2.1. At each grid cell, the model integrates the continuity equation forward in time to determine instantaneous concentrations for each species, which are averaged and then reported at specified intervals.

Advantages of the CAMx model stem from its comprehensive modeling approach and its expansive suite of ozone assessment tools. The ability to simulate multiple physiochemical processes allows for investigation into the complex interactions of those processes as well as their individual contributions to atmospheric composition. Compared to other chemical transport models, the CAMx model in particular leverages its complexity into valuable tools for characterizing and quantifying mass budget terms. Specifically, CAMx supports physical and chemical Process Analysis (PA), Ozone and Particulate Source Apportionment Technology (OSAT/PSAT), Decoupled Direct Method (DDM) and Higher-Order DDM (HDDM) Source Sensitivity, and Reactive Tracers (RTRAC). Such tools are particularly valuable to state regulatory agencies, who use them regularly for SIP development. Considered a "regional" model, CAMx is typically configured to simulate atmospheric composition across large expanses of land, throughout the troposphere, and over timescales of months to years (Emery et al., 2012; Goldberg et al., 2016, 2015; Marvin et al., 2019; Nopmongcol et al., 2012; Vijayaraghavan et al., 2016).

Three-dimensional models like CAMx can be computationally expensive. For example, standard CAMx simulations may require 1–3 hours of runtime for every day of output, even with the implementation of parallel processing techniques. Typical model resolution is no less than 12×12 km^2 in space and hourly in time for regional applications (Emery et al., 2012; Goldberg et al., 2016, 2015; Marvin et al., 2019; Nopmongcol et al., 2012; Vijayaraghavan et al., 2016). The computationally demanding nature of such models also necessitates the use of condensed gas-phase chemical mechanisms with relatively few species and reactions: version 6.50 of CAMx comes standard with four variations of the Carbon Bond mechanism – CB05 (Yarwood

et al., 2005), CB6r2 (Hildebrandt Ruiz and Yarwood, 2013; Yarwood et al., 2010), CB6r2 with halogen chemistry (115 species and 304 reactions) (Yarwood et al., 2014), and CB6r4 (86 species and 229 reactions) (Emery et al., 2016, 2015) – as well as the 2007 version of the condensed Statewide Air Pollution Research Center (SAPRC) mechanism with updated chemistry for toxic species (117 species and 565 reactions) (Carter, 2010; Hutzell et al., 2012). An option is also provided for the user to create an original gas-phase chemical mechanism from scratch.

Extensive pre-processing is required to prepare inputs for compatibility with the CAMx model framework. As shown in Fig. 2.7, the CAMx model requires prepared inputs for meteorology, emissions, photolysis, and landcover, as well as initial and boundary conditions, which must all conform to a desired domain, timeframe, and resolution. For a typical regional air quality modeling application, meteorological conditions are simulated using an auxiliary weather model such as the Weather Research and Forecasting (WRF) model (Skamarock et al., 2008). Most anthropogenic emissions are compiled from existing inventories, such as the National Emissions Inventory (NEI) (EPA, 2015a). Such inventories provide emission factors and activity data for mobile vehicle emissions, but proper emissions must be simulated using a model such as the Motor Vehicle Emission Simulator (MOVES) (EPA, 2015b), which applies meteorological output from the weather model. Biogenic emissions are also meteorology-dependent, and they are typically simulated using models such as the Model of Emissions of Gases and Aerosols from Nature (MEGAN) (Guenther et al., 2012) or the Biogenic Emissions Inventory System (BEIS) (Bash et al., 2016). Anthropogenic and biogenic emissions can be merged together using the Sparse Matrix Operator Kernel Emissions (SMOKE) modeling system (Community Modeling and

Analysis System, 2017). Sea salt emissions are also meteorology-dependent and may be entirely prepared and merged using CAMx support software. Simulation of photolysis rates requires total ozone columns, which can be obtained from satellite data, for example from the Ozone Monitoring Instrument (OMI) (http://ozoneaq.gsfc.nasa.gov/data/ozone). Lookup tables for photolysis rates must then be prepared using a CAMx-compatible extension of the TUV model. Existing databases for landcover and leaf area index (LAI) must be shaped to the model domain using a geographic information system (GIS). Finally, initial and boundary conditions must be extracted from existing three-dimensional model simulations, with boundary conditions usually

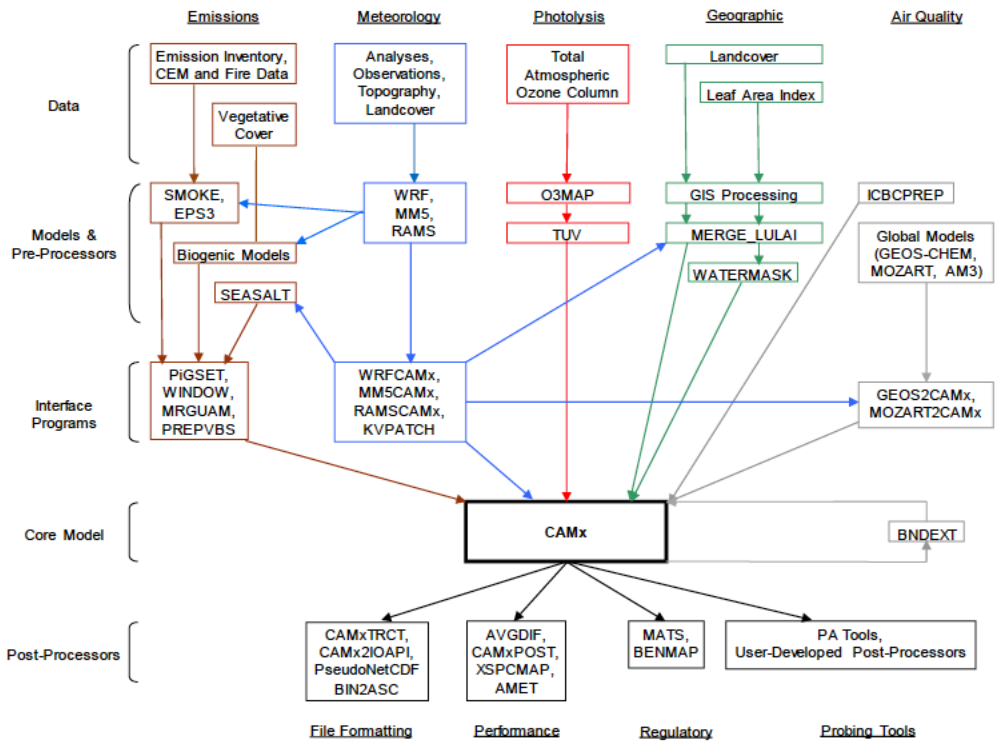

Fig. 2.7. From Ramboll Environ (2018): "Schematic diagram of the CAMx modeling system."

determined using a global model such as GEOS-Chem (Henderson et al., 2014). Processing software must then be applied to all prepared inputs to format them for compatibility with CAMx.

An example CAMx model setup script is provided in Appendix A. This script demonstrates the incorporation of the various model inputs and the configuration of other settings essential to the model. The user must specify the model domain and resolution, and may also select from a number of model options, for example among advection solvers, planetary boundary layer schemes, chemistry solvers, dry deposition models, plume-in-grid models, and probing tools. Model output consists of the time-averaged mixing ratios (ppm) predicted for user-selected species at each grid cell center throughout the model domain and timeframe, though probing tools can be applied to extract additional information.

The CAMx model, user's guide, support software, and an example test case are available for download at: http://www.camx.com. The model and its support software are programmed in Fortran 90, though user interaction is mainly limited to Linux shell scripting. The accessibility and valuable probing tools of CAMx have earned the model a prominent role in the air quality community, and CAMx is therefore commonly used for applications that target the development or improvement of regulatory policies (Emery et al., 2012; Goldberg et al., 2016, 2015; Nopmongcol et al., 2012; Vijayaraghavan et al., 2016).

2.2.2 Contributions

I developed a platform for using the CAMx regional model to simulate atmospheric composition over the continental US (CONUS) (Fig. 2.8) for the summer of 2013. This platform is designed to run CAMx version 6.50 for May 1 – July 18 of 2013 at hourly temporal resolution and 12 × 12 km^2 spatial resolution through 35 vertical layers, from the surface to ~100 mb. The selected domain is of particular interest for its coincidence with the SENEX aircraft campaign (May 29 – July 10) and the greater Southeast Atmosphere Study (SAS) (Mao et al., 2018).

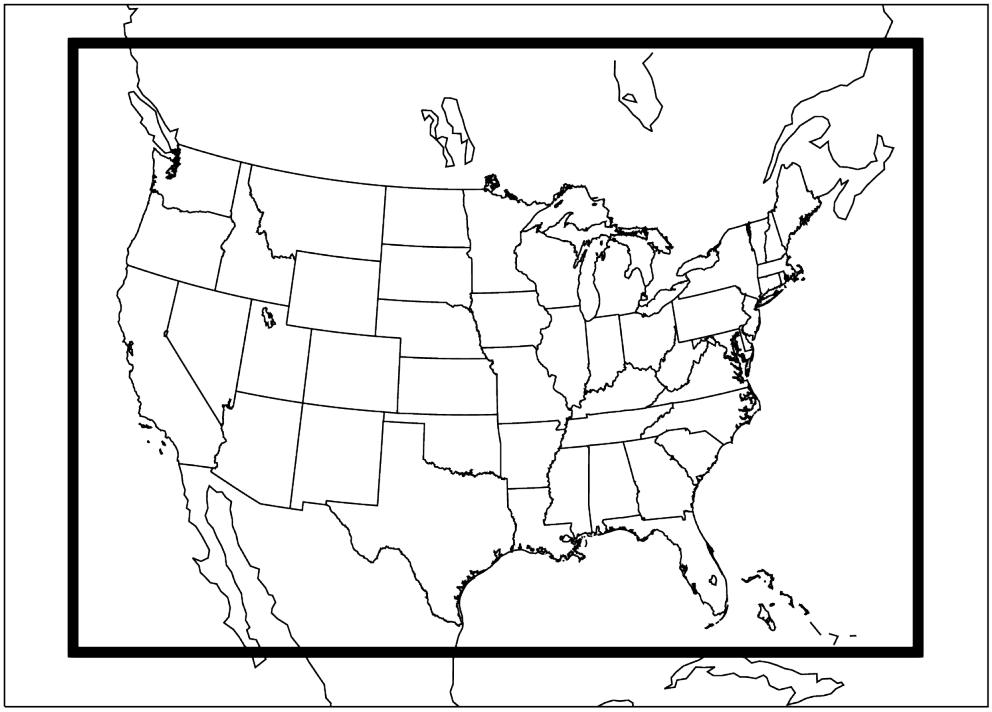

Fig. 2.8. Model domain from the CONUS 2013 platform developed for CAMx. The box bordered in thick black lines indicates the domain boundaries.

To build this modeling platform, I leveraged inputs originally developed by the US Environmental Protection Agency (EPA) for implementation in the Community Multiscale Air Quality (CMAQ) model (https://www.cmascenter.org/cmaq/) (Pye et al., 2018, 2015). I inherited CMAQ-ready inputs for meteorology, anthropogenic area and point emissions, as well as initial and boundary conditions. Meteorological conditions were simulated for 2013 using the WRF model version 3.8 (Skamarock et al., 2008). Anthropogenic area and point emissions were drawn from the 2011 NEI version 2 "ek" (EPA, 2015a), with electrical generating unit (EGU) emissions updated using temporalized Continuous Emission Monitoring System (CEMS) data for 2013 (Farkas et al., 2015) and mobile emissions simulated for 2013 using MOVES 2014a (EPA, 2015b). Initial and boundary conditions were extracted from a 36 km CMAQ simulation that was in turn initialized with output from a global simulation of GEOS-Chem version 8-3-2 (Henderson et al., 2014).

Once these principal inputs were obtained, I prepared all remaining inputs and processed the entire platform for compatibility with the CAMx model framework. For example, I optimized the meteorology by patching vertical diffusivity to enhance mixing over urban areas (Huszar et al., 2018), and by constraining LAI to GIS-processed remote observations from the Moderate Resolution Imaging Spectrometer (MODIS) that were provided by the EPA. I used BEIS version 3.61 (Bash et al., 2016), as implemented in SMOKE version 4.5 (Community Modeling and Analysis System, 2017), to apply the meteorological conditions from WRF to normalized biogenic emissions provided by the EPA; then, I used SMOKE to merge the biogenic and anthropogenic area source emissions. I applied the meteorology and a water mask provided by the EPA to generate sea salt emissions, which I prepared and merged using

the corresponding CAMx pre-processor. Though most of the provided anthropogenic point source emissions could be formatted directly for use in CAMx, differences between CAMx and CMAQ in the inline plume rise algorithm for wildfire emissions necessitated modification of the corresponding stack parameters, which I implemented as described in Appendix C. I combined all anthropogenic point source emissions together using an auxiliary CAMx merging program. I also extracted total column ozone from OMI data (http://ozoneaq.gsfc.nasa.gov/data/ozone) and ran the TUV pre-processor for CAMx to generate photolysis rate lookup tables. Finally, I used various utilities from the model's support software to format all inputs, self-prepared and inherited alike, for direct implementation into CAMx.

Fundamental differences between the CAMx and CMAQ model frameworks lead to inherent deviations in the CONUS 2013 platforms designed for each, beyond simple formatting requirements. For example, CMAQ supports inline simulation of biogenic and sea salt emissions, whereas CAMx requires offline pre-processing of emissions from these sources, which is expected to degrade precision and increase uncertainty compared to CMAQ. Differences in the internal treatment of these emissions are reflected in the preparation of their respective inputs for model implementation. Furthermore, CMAQ also supports inline simulation of windblown dust (Foroutan et al., 2017), lightning NO_x (Allen et al., 2012; Pickering et al., 1998), and bidirectional ammonia emissions (Pleim et al., 2013). However, none of these are supported by CAMx, so the corresponding inputs are omitted entirely from the CONUS 2013 platform. Although these components are not significant to my applications, the bias and uncertainty introduced to CAMx output through such simplification can be

evaluated by comparison to CMAQ and should be assessed for each application of the CONUS 2013 modeling platform.

A complete description of the CONUS 2013 modeling platform for CAMx is presented in Chapter 4, which is in preparation for publication. All CAMx-ready model inputs developed for this platform are uploaded to servers hosted by Department of Atmospheric and Oceanic Science. These servers also store the output from a CONUS 2013 baseline simulation for May 21 – July 15 that implements the CB6r2 gas-phase chemical mechanism with halogen chemistry (Hildebrandt Ruiz and Yarwood, 2013; Yarwood et al., 2014, 2010). Compiled executables for the CAMx model version 6.50, SMOKE version 4.5, and all other software used to construct the CONUS 2013 platform are also available. I have stored these resources on the campus servers to maintain their accessibility and promote their application by colleagues affiliated with the University of Maryland.

2.2.3 Applications

The expansive domain and practical resolution of the CONUS 2013 platform for CAMx support a variety of modeling applications. Its coincidence with the SENEX aircraft campaign is particularly useful to the research that I lead, because it maintains consistency between studies. In Chapter 4, I apply the CONUS 2013 modeling platform to explore how improvements to isoprene oxidation chemistry and emissions impact the simulation of ozone and its precursors. I conducted four simulations on the CONUS domain for May 21 – July 15 to test these improvements: a baseline simulation running standard CB6r2 with halogen chemistry (Hildebrandt Ruiz and Yarwood, 2013;

Yarwood et al., 2014, 2010), two sensitivity simulations testing updates to the isoprene chemistry, and one sensitivity simulation applying an additional modification to the input isoprene emissions. I evaluate the simulations against SENEX observations of ozone, NO_x, and VOCs including isoprene, HCHO and PAN. I also make use of the CAMx probing tool for chemical process analysis to investigate effects on ozone production rates and the designation of VOC- or NO_x-limited regimes. Please refer to Chapter 4 for a complete description of this application of the CONUS 2013 platform for CAMx.

The CONUS 2013 platform for CAMx also extends the boundaries that have previously limited our research group to regional modeling of only the Eastern US, which presents new opportunities for our colleagues to explore subjects such as air quality, biomass burning, and boundary conditions to the west. For example, Professor Timothy Canty has applied the CONUS 2013 platform for CAMx to investigate the impact of wildfires in the Western US. Fig. 2.9 demonstrates the influence of wildfires on average maximum 8-hour ozone for June 2013, which exceeds the 70 ppb ozone standard in the regions of California that experienced significant wildfires during that time, namely Los Angeles, Santa Barbara, and Mariposa Counties. Professor Canty has submitted a grant proposal that supports use of the CONUS 2013 platform to evaluate and improve wildfire plume rise in both the CAMx and CMAQ regional models. It is my hope that Professor Canty and other colleagues at the University of Maryland will continue to make use of the CONUS 2013 platform for CAMx, in support of these and other potential air quality applications.

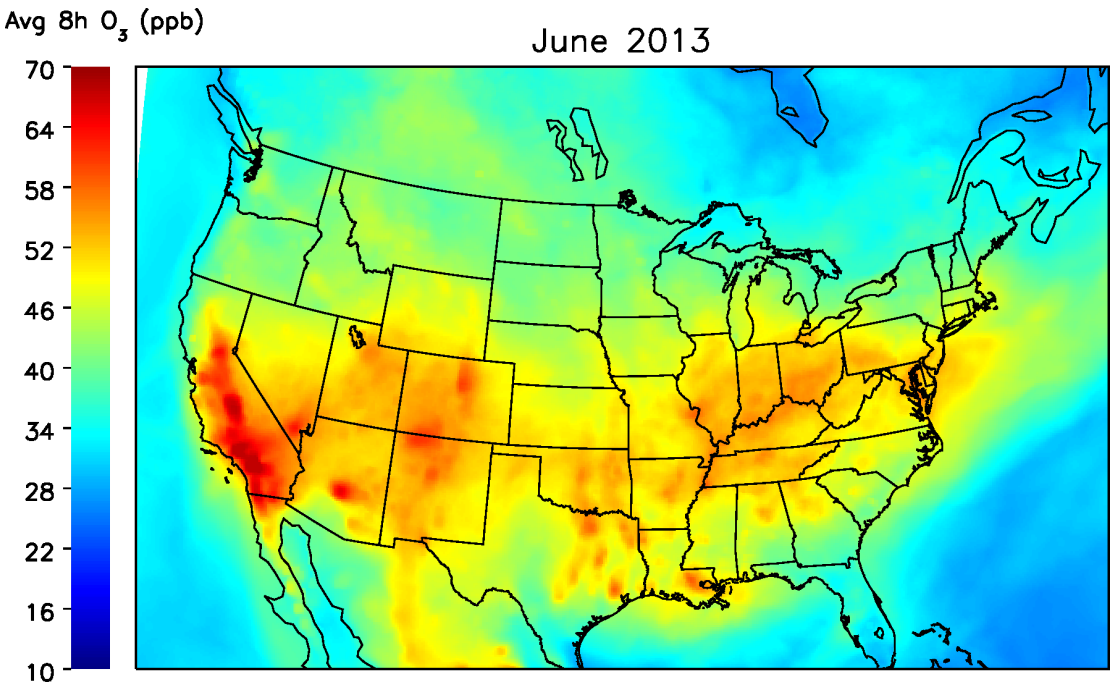

Fig. 2.9. Courtesy of Professor Timothy Canty: Average maximum 8-hour ozone (ppb) simulated for the month of June using the CONUS 2013 platform for CAMx. The color bar indicates average maximum 8-hour ozone on a scale of 10–70 ppb. Average maximum 8-hour ozone exceeds the 70 ppb ozone standard in California, over regions affected by wildfires, including Los Angeles, Santa Barbara, and Mariposa Counties.

Chapter 3: Impact of evolving isoprene mechanisms on simulated formaldehyde: An inter-comparison supported by in situ observations from SENEX

This chapter was previously published under the same title, as an article in the scientific journal *Atmospheric Environment*. I am the lead author of this work, and I acknowledge collaboration with 19 co-authors, who form a network of support connecting colleagues at the University of Maryland, developers of the F0AM box model, and participants in the SENEX aircraft campaign. The article was published on 30 May 2017, appearing in Volume 164, pages 325–336. Here, the numbering of sections, figures, and tables reflects incorporation into the greater dissertation. The supplemental material from the article is distributed throughout the chapter, and comprises Appendices D and E.

3.1. Introduction

Isoprene (C_5H_8) is a reactive biogenic hydrocarbon that fuels oxidative chemistry in many terrestrial regions. Annual isoprene emissions are ~500 Tg yr^{-1}, accounting for nearly one-third of global non-methane volatile organic compound (VOC) emissions (Guenther et al., 2012). Once emitted, isoprene is quickly oxidized by atmospheric OH, which limits the isoprene lifetime to <1–3 hours. The oxidation of isoprene by OH generates many products, including formaldehyde (HCHO), methyl vinyl ketone (MVK), methacrolein (MACR), and numerous other oxygenated organic compounds. Depending on conditions for NO_x ($NO_x = NO + NO_2$), the oxidation of

isoprene can also produce ozone (Trainer et al., 1987) or secondary organic aerosol (SOA) (Jacobs et al., 2014; Kroll et al., 2006; Lin et al., 2013; Paulot et al., 2009b; Surratt et al., 2010; Surratt et al., 2006), both of which are hazardous to human health (EPA, 2009, 2013) and are strong climate forcers (IPCC, 2013).

The oxidation of isoprene by OH leads to the formation of isoprene hydroxy peroxy radicals ($ISOPO_2$), with subsequent chemistry determined by NO_x conditions. In the presence of NO_x, $ISOPO_2$ reacts with NO to form MVK, MACR, and HCHO (Paulson and Seinfeld, 1992). In a minor channel, the reaction of $ISOPO_2$ with NO produces organic nitrates (ISOPN), which undergo oxidation by OH to form small nitrated organic products (Paulot et al., 2009a). The high-NO_x reaction pathways of $ISOPO_2$ result in the net conversion of NO to NO_2, which promotes production of tropospheric ozone. Under low-NO_x conditions, $ISOPO_2$ may react with HO_2 or RO_2 or isomerize. Reaction with HO_2 produces isoprene hydroperoxides (ISOPOOH), which undergo oxidation by OH to form isoprene epoxydiols (IEPOX), known precursors of SOA (Paulot et al., 2009b). Reaction of $ISOPO_2$ with RO_2 mainly produces MVK, MACR, and HCHO (Saunders et al., 2003). Isomerization of $ISOPO_2$ proceeds by intramolecular hydrogen transfer, specifically via either 1,5-H or 1,6-H shift (Da Silva et al., 2010; Peeters et al., 2009). The 1,5-H shift forms an unstable intermediate that degrades into MVK, MACR, and HCHO. The 1,6-H shift produces hydroperoxy aldehydes (HPALD), which photolyze to form small VOCs and regenerate OH (Crounse et al., 2011; Peeters and Müller, 2010; Peeters et al., 2014; Wolfe et al., 2012).

Representations of isoprene chemistry in gas-phase chemical mechanisms can vary widely (Table 3.1). Inconsistencies arise from differences in complexity, choice

of kinetic rate constants, and incorporation of results from recent literature. Previous mechanism inter-comparison studies have shown that different interpretations of atmospheric chemistry lead to conflicting representations of species important to air quality and climate, including ozone (Coates and Butler, 2015; Emmerson and Evans, 2009; Knote et al., 2015; Saylor and Stein, 2012; Yu et al., 2010). Although some mechanism inter-comparisons have focused on isoprene oxidation in the past (Archibald et al., 2010; Fan and Zhang, 2004; Pöschl et al., 2000; Squire et al., 2015; von Kuhlmann et al., 2004; Zhang et al., 2011), the scientific understanding of isoprene chemistry has evolved rapidly in recent years, with discoveries such as epoxide formation (Paulot et al., 2009b), peroxy radical isomerization (Peeters et al., 2009), and OH regeneration (Paulot et al., 2009b; Peeters et al., 2009; Wolfe et al., 2012). Furthermore, the limited availability of *in situ* observations has restricted our ability to quantitatively evaluate mechanisms against ground truth.

Formaldehyde is produced in high yield throughout the isoprene cascade (Tuazon and Atkinson, 1990). The chemical link between HCHO and isoprene also depends on NO_x, which determines the chemical fate of $ISOPO_2$ and subsequent yield of organic products (Wolfe et al., 2016a). Although complex, the relationships between these species are crucial to many modeling applications. In air quality simulations, for example, the production of HCHO from VOCs such as isoprene is indicative of the effects of VOC oxidation on ozone production (Sillman, 1995). Also, space-based HCHO column observations are often used to constrain isoprene emissions inventories, with direct consequences for modeled ozone and SOA (Millet et al., 2008; Palmer et al., 2003). *In situ* measurements of HCHO, isoprene, and NO_x are highly resolved in space and time, allowing for their photochemical relationships to be explored in great

detail (Wolfe et al., 2016a). Observations of these and several related species were collected during the Southeast Nexus (SENEX) aircraft campaign, which took place in the Southeast United States in 2013 (Warneke et al., 2016). This region is abundant in isoprene and variable in NO_x, which provides a unique opportunity to test the sensitivity of modeled HCHO to differences in isoprene chemistry.

Here, we combine *in situ* observations from SENEX with a constrained photochemical box model to evaluate and inter-compare isoprene oxidation schemes in five different gas-phase chemical mechanisms: CB05, CB6r2, GEOS-Chem, MCMv3.2, and MCMv3.3.1. The box model is constrained to observations of isoprene and related species – NO, NO_2, O_3, CO, methane (CH_4), methanol (CH_3OH), and peroxy acetyl nitrate (PAN) – and is used to simulate isoprene chemistry during SENEX with respect to each considered mechanism. *In situ* measurements of HCHO provide a benchmark for model performance, and inter-comparison of reaction-specific HCHO production rates elucidates the mechanistic drivers of model-to-model differences. Based on the results of our study, we recommend improvements to CB6r2, which has the greatest potential for impact with regard to air quality management. Implications for modeled ozone are discussed.

3.2. Choice of gas-phase chemical mechanisms

Mechanisms investigated in this work include two versions of the Carbon Bond (CB) mechanism, CB05 and CB6r2; two versions of the Master Chemical Mechanism (MCM), MCMv3.2 and MCMv3.3.1; and GEOS-Chem v9-2+. Condensed mechanisms CB05, CB6r2, and GEOS-Chem are designed for implementation in

chemical transport models (CTMs): CB05 and CB6r2 are used extensively in air quality simulations (Canty et al., 2015; Goldberg et al., 2016), and GEOS-Chem is a standard tool for evaluation of space-based HCHO column observations (Zhu et al., 2016). The MCM, which is chemically near-explicit (i.e., highly detailed), is commonly used with photochemical box models to assess knowledge of tropospheric chemistry, and also provides a benchmark for evaluating condensed mechanisms (Jenkin et al., 2015). Size and complexity vary widely between mechanisms, from ~50 species and ~150 reactions in CB05 to ~600 species and ~2000 reactions in an isoprene-focused subset of MCMv3.3.1. The number of species and reactions included in each mechanism are listed in Table 3.1. Each mechanism features a unique isoprene oxidation scheme. The CB05 mechanism uses a scheme carried over from CB4, in which first-generation isoprene oxidation is represented by a single reaction: isoprene reacts with OH to form HO_2, RO_2, MVK, MACR, and HCHO (Yarwood et al., 2005). Intermediate $ISOPO_2$ is not explicitly described. The isoprene scheme is updated in CB6r2 to account for the formation of $ISOPO_2$ and its reactions with NO, HO_2, and RO_2 (Hildebrandt Ruiz and Yarwood, 2013).

Table 3.1. Gas-phase chemical mechanisms evaluated and compared in this work.

Mechanism	Species	Reactions	Reference
CB05[a]	53	156	Yarwood et al., 2005
CB6r2[a]	77	216	Hildebrandt Ruiz and Yarwood, 2013
GEOS-Chem[b]	171	505	Mao et al., 2013b
MCMv3.2[c]	455	1476	Saunders et al., 2003
MCMv3.3.1[c]	610	1974	Jenkin et al., 2015

[a]Updated for consistency with CAMx v6.40 documentation.
[b]Updated for consistency with Kim et al. (2015), Fisher et al. (2016), Marais et al. (2016), and Travis et al. (2016).
[c]Subset of MCM with organic chemistry limited to methane, methanol, and isoprene oxidation.

Isomerization of $ISOPO_2$ is also represented; however, only the 1,6-H shift is considered. The isoprene scheme in GEOS-Chem v9-2+ was recently updated to include the 1,6-H shift isomerization pathway, and its basic underlying structure is similar to that of CB6r2 (Mao et al., 2013b; Travis et al., 2016). The 9-2+ version also features optimized yields of ISOPOOH and ISOPN, up-to-date secondary chemistry, and expanded treatment of SOA (Fisher et al., 2016; Kim et al., 2015; Marais et al., 2016; Travis et al., 2016). The MCMv3.2 mechanism adopts a more complex isoprene oxidation scheme that traces four different $ISOPO_2$ isomers through their reactions with NO, HO_2, and RO_2 (Saunders et al., 2003). The distribution of $ISOPO_2$ isomers and their unique products depends on the $ISOPO_2$ lifetime (Teng et al., 2017), which is neglected in coarser mechanisms. The MCMv3.2 scheme additionally considers the reaction of $ISOPO_2$ with NO_3; however, the 1,5-H shift and 1,6-H shift isomerization pathways are omitted. Both isomerization pathways are included in MCMv3.3.1, along with reversible O_2 addition to form $ISOPO_2$, new OH adducts and $ISOPO_2$ isomers, and updates to existing reaction parameters following recommendations from recent literature (Jenkin et al., 2015).

Early versions of the CB and MCM were included in a mechanism inter-comparison study by Pöschl et al. (2000), which was one of the first to focus specifically on isoprene chemistry. The purpose of the study was to develop a new condensed isoprene oxidation mechanism (Mainz Isoprene Mechanism, MIM) based on explicit chemistry in MCMv2, and to compare model performance against other condensed mechanisms, including CB4. A box model was used to simulate different emission scenarios and produce time series of several species, which were evaluated against MCMv2. Compared to MCMv2, most condensed mechanisms underestimated

modeled ozone except for MIM, which agreed mostly to within 10%. Von Kuhlmann et al. (2004) implemented selected mechanisms from the Pöschl study – including MIM and CB4 – in the MATCH-MPIC (Model of Atmospheric Transport and Chemistry – Max-Planck-Institute for Chemistry) CTM. The simulated global tropospheric ozone burden was found to be relatively insensitive to choice of isoprene mechanism, varying by only 5%.

Similar studies have been performed since, but perhaps the most relevant to this work is by Archibald et al. (2010), who inter-compared more recent mechanisms including CB05, GEOS-Chem v7-3-6, and MCMv3.1. Their study demonstrated good agreement with respect to modeled ozone, but large variability in modeled mixing ratios of other isoprene oxidation products such as HCHO, MVK, and MACR. Mechanisms were evaluated by comparison to MCMv3.1: most organic products were overestimated by CB05 and were either matched or underestimated by GEOS-Chem, depending on conditions for isoprene and NO_x. Zhang et al. (2011) followed with an inter-comparison of some of the same mechanisms – such as CB05 and MCMv3.1 – that included support from chamber studies. Under isoprene-rich conditions, MCMv3.1 matched measured ozone mixing ratios within 5–45%, improving with chamber evolution over time; CB05, however, consistently underestimated ozone by at least 30%. The MCM also matched peak measurements of MVK and MACR within ~20%, though a similar comparison was not included for CB05. Measurements of HCHO were not reported.

The CB, GEOS-Chem, and MCM mechanisms have all recently been updated to reflect the current understanding of isoprene chemistry. New versions CB6r2, GEOS-Chem v9-2+, and MCMv3.3.1 account for recent contributions from Paulot et

al. (2009a, 2009b), Peeters et al. (2009), and many others (Bates et al., 2014; Crounse et al., 2011; Da Silva et al., 2010; Peeters and Müller, 2010; Peeters et al., 2014; Wolfe et al., 2012). Inclusion of previous versions of the CB and MCM allows us to examine the impact of these recent updates. Specific updates between GEOS-Chem v9-2+ and prior versions of GEOS-Chem are discussed elsewhere (Fisher et al., 2016; Kim et al., 2015; Marais et al., 2016; Travis et al., 2016). Our study is the first isoprene-focused inter-comparison to include the most recent versions of these mechanisms, and to evaluate results by comparison to *in situ* observations of isoprene oxidation products such as HCHO.

3.3. Methods

3.3.1. Aircraft observations

The objective of the NOAA SENEX mission was to explore the interactions between biogenic and anthropogenic emissions that define atmospheric composition in the summertime Southeast US. Based out of Smyrna, TN, SENEX comprised 20 research flights of the NOAA WP-3D aircraft between May 29 and July 10 of 2013. Flight tracks are provided in Fig. 3.1. The payload featured instruments that characterize and quantify aerosols and numerous gas-phase atmospheric constituents including ozone, NO_x, and VOCs (Warneke et al., 2016). More information about the SENEX aircraft campaign is available at http://www.esrl.noaa.gov/csd/projects/senex/.

In situ observations of HCHO obtained during SENEX were collected using the NASA In Situ Airborne Formaldehyde (ISAF) instrument, which detects HCHO by laser-induced fluorescence (LIF) (Cazorla et al., 2015). The ISAF instrument reports

measurements of HCHO at 1 Hz, and has a detection limit of 36 ppt for a signal-to-noise ratio of 2. Accuracy is ±10% based on instrument calibration, which is determined via standard additions of known HCHO mixtures to zero air before and after each field mission. As described in Cazorla et al. (2015), calibration is tied to the literature UV cross section of HCHO (Meller and Moortgat, 2000) and typically varies by less than 10% over the course of a mission. Observations of NO, NO_2, O_3, CO, isoprene, methane, methanol, PAN, and the J-values $J(O^1D)$ and $J(NO_2)$ are used to constrain the box model, which is described in the next section. Corresponding instrumentation and measurement accuracies are included in Table 3.2. Further information on SENEX instrumentation is provided by Warneke et al. (2016).

All observations used in this study are averaged to a 60-second time base and then filtered for daytime (SZA < 70°), boundary-layer (altitude < 1500 m) conditions. Data are also filtered to exclude biomass burning (CO > 300 ppb or acetonitrile > 0.5 ppb), fresh NO_x sources ($NO_x > 95^{th}$ percentile), and missing or negative measurements of species used to constrain the box model. This filtering procedure retains a total of 2219 data points, spanning a wide gradient in mixing ratios of both NO_x (0.07–1.63 ppb) and isoprene (~0–8.15 ppb). Fig. 3.1 shows the geographical distribution of observed HCHO mixing ratios (1.12–9.98 ppb) that are included in our analysis.

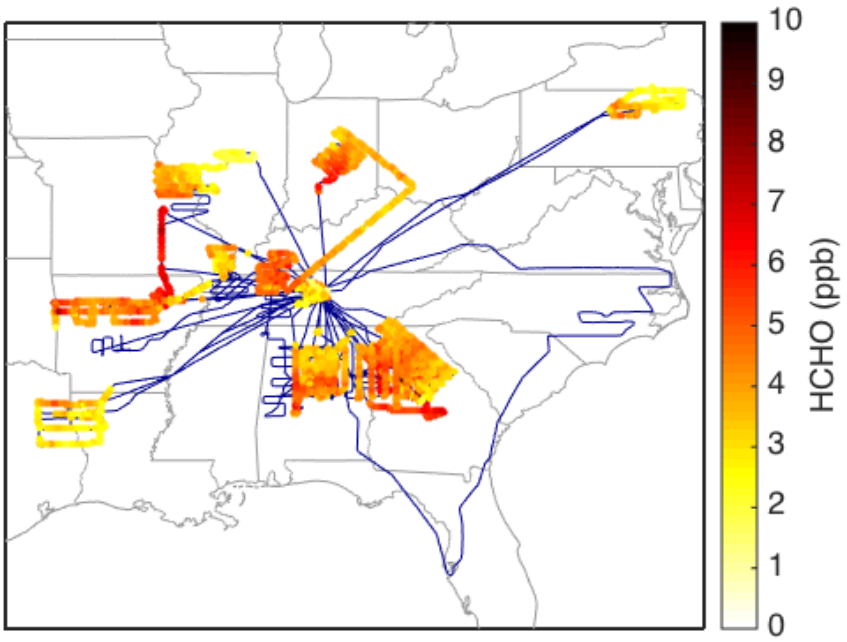

Fig. 3.1. Map of the flight tracks from the SENEX aircraft campaign. Flight tracks are plotted in blue, with ISAF measurements of HCHO (ppb) plotted over the tracks, according to the scheme denoted by the color bar. Observations are 60-second averages and are only included if collected in the daytime (SZA < 70°) boundary layer (altitude < 1500 m). Observations affected by biomass burning (CO > 300 ppb or acetonitrile > 0.5 ppb), fresh NO_x sources (NO_x > 95th percentile), and missing or negative measurements of constrained species are excluded.

Table 3.2. Instrumentation for the SENEX observations used in this work (adapted from Warneke et al., 2016).

Measurement	Technique	Accuracy
NO; NO_2; O_3	Chemiluminescence	3%; 4%; 2%
CO	Vacuum ultraviolet resonance fluorescence	5%
CH_4	Cavity ring-down spectroscopy (CRDS)	0.07 ppm
C_5H_8; CH_3OH	Proton-transfer-reaction mass spectrometry (PTR-MS)	25%
HCHO	Laser-induced fluorescence (LIF)	10%
PAN	Chemical ionization mass spectrometry (CIMS)	0.04–0.05 ppb
J-values	Filter radiometry	10%

3.3.2. Box model simulations

We use the Framework for 0-D Atmospheric Modeling version 3 (F0AMv3) (Wolfe et al., 2016b) to simulate isoprene chemistry during SENEX. Though each simulation features a different chemical mechanism, the model setup is otherwise identical. Simulations are constrained to match observed mixing ratios of NO, NO_2, O_3, CO, isoprene, methane, methanol, and PAN, while H_2 (not observed) is assigned a mixing ratio of 550 ppb (Novelli et al., 1999). Mixing ratios are held fixed throughout each model run for all constrained species except NO, which is allowed to float after initialization to preserve the modeled NO/NO_2 ratio. Reaction rate constants are calculated using aircraft measurements of pressure, temperature, and relative humidity. Time and location of the aircraft are used to calculate solar zenith angle (SZA), which controls photolysis rates as described below. The chemical system defined by each set of observations is integrated 72 hours forward in time, in one-hour time steps with time-varying SZA, to reach diel steady state. Physical losses are represented by a 24-hour lifetime applied to all species.

The J-values corresponding to the major photolytic pathways of ozone and NO_2 – $J(O^1D)$ and $J(NO_2)$, respectively – are constrained to match observations. All other J-values are initialized using a set of lookup tables based on literature-derived photolysis parameters and solar spectra from the NCAR Tropospheric Ultraviolet and Visible (TUV) radiation model (https://www2.acom.ucar.edu/modeling/tropospheric-ultraviolet-and-visible-tuv-radiation-model). Lookup tables are organized by SZA, altitude, overhead ozone, and surface albedo (Wolfe et al., 2016b). We use SZA and altitude from aircraft measurements and constant values for ozone column (300 DU) and surface albedo (0.05), which we estimate for SENEX using concurrent data from

the Ozone Monitoring Instrument (OMI) Level-3 OMDOAO3e data product (https://disc.gsfc.nasa.gov/Aura/data-holdings/OMI/omdoao3e_v003.shtml). The average ratio of measured-to-calculated $J(O^1D)$ and $J(NO_2)$ provides a multiplicative scaling factor, which is applied to all unconstrained J-values. This scaling technique improves consistency with observations and reduces sensitivity to initial choice of overhead ozone column and surface albedo. Once initialized, all J-values are allowed to evolve throughout the corresponding model run following a simulated diel cycle.

For each simulation, model output includes diel steady-state mixing ratios and instantaneous reaction rates for species corresponding to the implemented gas-phase chemical mechanism. In the following analysis, we evaluate the isoprene schemes in the five mechanisms chosen for this study by comparing modeled HCHO mixing ratios to SENEX observations. Additionally, we explore the underlying chemistry of the mechanisms by closely examining simulated HCHO production and loss rates.

3.4 Analysis

3.4.1 Comparison to observations

To assess the accuracy of the mechanisms, we compare modeled and measured mixing ratios of HCHO from SENEX, as shown in Fig. 3.2. Linear least-squares regression analysis is performed for each mechanism with respect to observations, and normalized mean bias (NMB) is calculated as follows:

$$\mathrm{NMB} = \frac{\frac{1}{n}\sum_{i=1}^{n}(M_i - O_i)}{\frac{1}{n}\sum_{i=1}^{n} O_i} \times 100\% \quad (3.1)$$

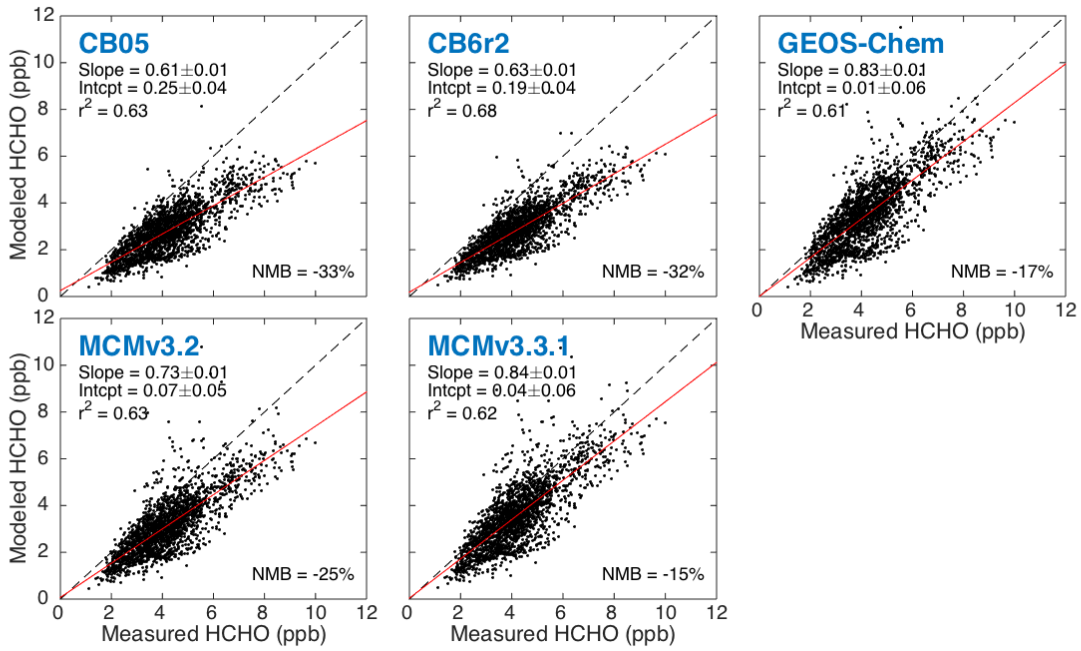

Fig. 3.2. Regression of modeled and measured mixing ratios of HCHO (ppb) from SENEX. Each panel features HCHO modeled using a different gas-phase chemical mechanism, as indicated. In each case, linear least-squares regression analysis provides parameters for a line of best fit, which is plotted in red. The 1:1 line, shown here as a dashed black line, is provided for reference. All uncertainties are 1σ standard deviations.

where M is the modeled HCHO mixing ratio (ppb) and O is the observed HCHO mixing ratio (ppb) for each individual point i in a total of n data points (n = 2219). Model-measurement agreement is best for MCMv3.3.1, with a regression slope of 0.84 ± 0.01 (1σ) and an NMB of −15%. Agreement worsens among the other mechanisms in the following order: GEOS-Chem (slope = 0.83 ± 0.01; NMB = −17%), MCMv3.2 (0.73 ± 0.01; −25%), CB6r2 (0.63 ± 0.01; −32%), and CB05 (0.61 ± 0.01; −33%). Using a two-tailed Z-test, we determine that differences in the slopes are statistically significant (p-value < 0.05), except between GEOS-Chem and MCMv3.3.1 (p-value = 0.56). Calculated r^2 values range from 0.61 for GEOS-Chem to 0.68 for CB6r2, indicating that 60–70% of the variability in the data is reproduced by the model. The fact that the

r^2 values are all very similar suggests that any unexplained variability is consistent among mechanisms and does not significantly influence differences in modeled HCHO. The MCMv3.3.1 and CB6r2 mechanisms demonstrate improved agreement with observations over their predecessors (MCMv3.2 and CB05, respectively); however, the degree of improvement of CB6r2 over CB05 is low, which is perhaps surprising given the drastic changes in the isoprene oxidation chemistry between these two CB versions. The chemically explicit MCM mechanisms result in better agreement with observations than either of the mechanisms of the condensed CB, though GEOS-Chem performs nearly as well as MCMv3.3.1, despite its classification as a condensed mechanism.

Comparison to observations also enables evaluation of the overall relationship between HCHO, isoprene, and NO_x. Fig. 3.3 shows the NO_x-dependence of measured and modeled HCHO from SENEX. Observations demonstrate a trend of increasing HCHO with NO_x, which is captured by all five mechanisms. As noted by Wolfe et al. (2016a), changes in both OH production and RO_2 branching drive this trend, with the former having a stronger net influence. The strength of the observed NO_x-dependence ($\Delta y/\Delta x$ between endpoints ~ 2.75 ppb HCHO per log(NO_x (ppb))) is best reproduced by MCMv3.2 (2.78). Otherwise, modeled NO_x-dependences vary in strength from CB05 (1.67) to MCMv3.3.1 (3.00). A more complex isoprene scheme in CB6r2, which includes NO-dependent branching of isoprene-derived RO_2 radicals, results in a stronger NO_x-dependence than is modeled for CB05. As a result, CB05 agrees better with measurements of HCHO obtained under low-NO_x conditions, but CB6r2 agrees better at high NO_x. Similarly, differences in the strengths of the NO_x-dependences of GEOS-Chem and MCMv3.3.1 allow GEOS-Chem to match MCMv3.3.1 at low NO_x,

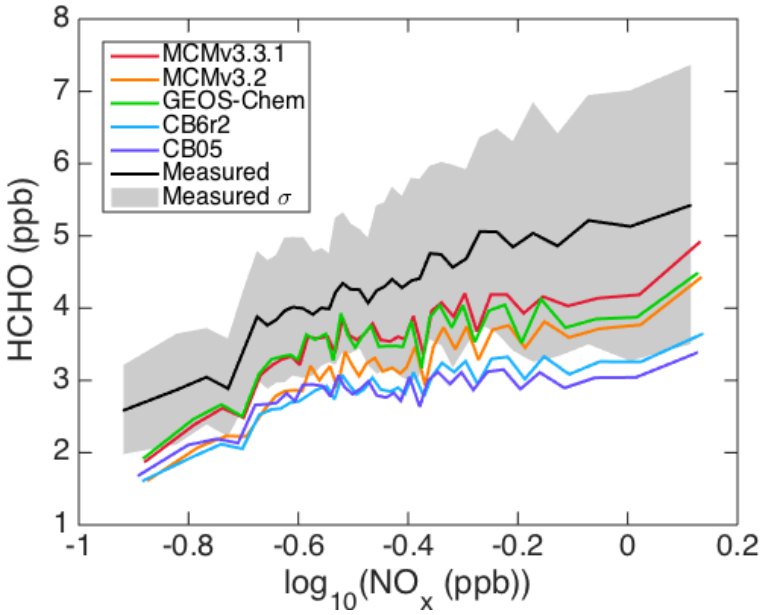

Fig. 3.3. NO_x-dependence of HCHO (ppb), as measured (black) and modeled (colors, as indicated for each mechanism) for SENEX. Data and model output are binned by log(NO_x), with each bin containing 60 points. Lines represent bin averages; the grey shaded region is the 1σ standard deviation of the binned measurements, which is not shown for the binned model output.

but to underestimate at high NO_x. This behavior is partly explained by the NO_x-dependence of modeled OH (Fig. 3.4): larger mixing ratios of OH at high NO_x in MCMv3.3.1 increase production of HCHO. Higher mixing ratios of OH also partly explain the ~0.5 ppb increase in modeled HCHO between MCMv3.2 and MCMv3.3.1, which is independent of NO_x across the range of conditions presented in Fig. 3.3. For all mechanisms, model-measurement agreement tends to decline with increasing NO_x and demonstrates nonlinear behavior at the tail ends of the NO_x distribution (Fig. 3.5).

Although most mechanisms effectively simulate the NO_x-dependence of HCHO, none reproduce the magnitude of measured HCHO mixing ratios. Fig. 3.2 points to a systematic bias in modeled HCHO that, in Fig. 3.3, is shown to be consistent across NO_x regimes. For all five simulations, HCHO is underestimated by at least 0.5–

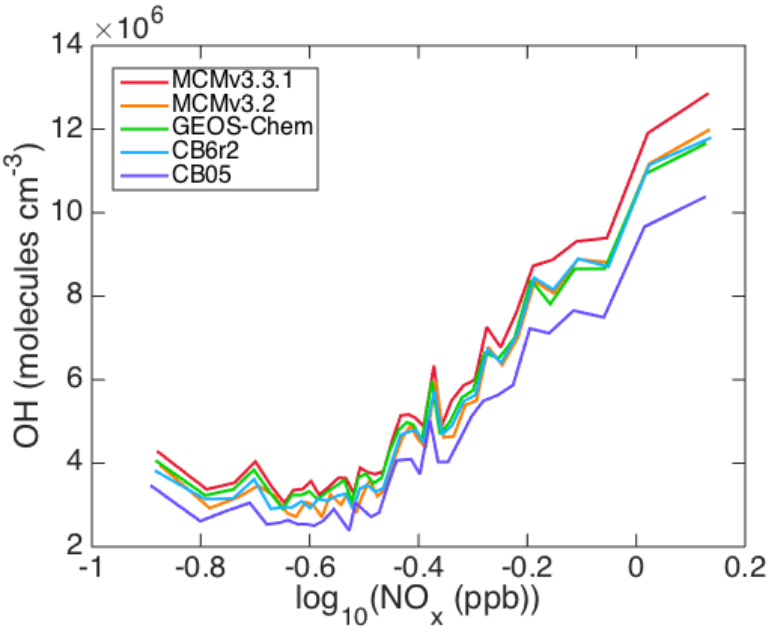

Fig. 3.4. NO_x-dependence of OH (molecules cm^{-3}), as modeled (colors, as indicated for each mechanism) for SENEX. Model output is binned by log(NO_x), with each bin containing 60 points. Lines represent bin averages.

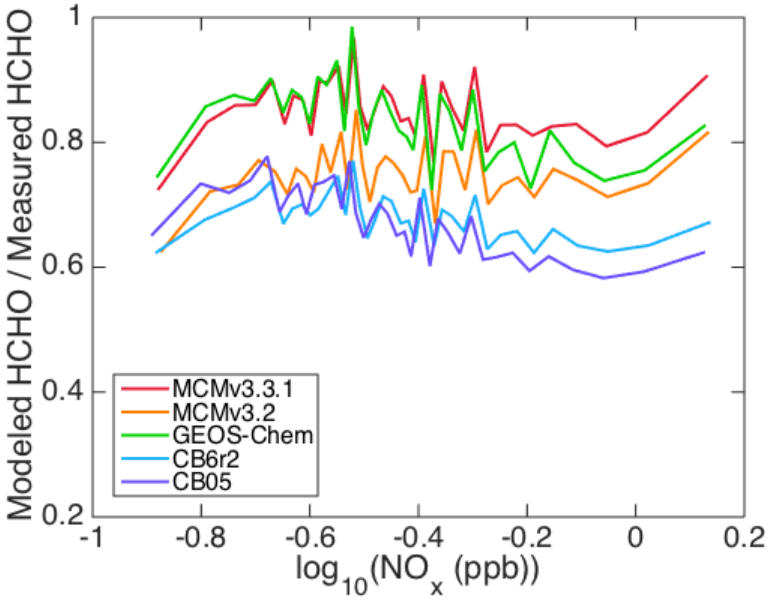

Fig. 3.5. NO_x-dependence of the ratio of modeled mixing ratios of HCHO (ppb) to measured mixing ratios of HCHO (ppb) for SENEX (colors, as indicated for each mechanism). Model output is binned by log(NO_x), with each bin containing 60 points. Lines represent bin averages.

1 ppb throughout the range of NO_x conditions sampled during SENEX. These results mirror those of Wolfe et al. (2016a), who observed the same trend in MCMv3.3.1 as well as the global model AM3 (Donner et al., 2011), which runs using a self-contained gas-phase chemical mechanism with updated isoprene chemistry (Mao et al., 2013a; Naik et al., 2013). Underestimated HCHO in both the 0-D and global models suggests that this bias is not an artifact of the steady-state box model setup. Wolfe et al. attributed the bias to "background" HCHO, due to either missing primary VOCs or inadequate representation of HCHO production in the later generations of isoprene degradation. Investigation of background HCHO from late-generation isoprene oxidation would require observations to constrain the full scope of the isoprene cascade, such as OH reactivity or additional late-generation products. However, we explore the impact of non-methane, non-isoprene primary VOCs on background HCHO in Section 3.4.3 and investigate additional strategies for bias mitigation in Section 3.5.

3.4.2 Formaldehyde production rates

To understand differences in simulated HCHO, we inter-compare underlying chemical rates. Because the lifetime of HCHO is comparable across all mechanisms (within 7%), our analysis focuses primarily on rates contributing to HCHO production. Average HCHO production rates (ppb hr^{-1}) computed for SENEX are shown in Fig. 3.6. Total rates range from 1.30 to 1.77 ppb hr^{-1}. Individual rates are sorted by primary source VOC – methane, methanol, or isoprene – and rates specific to isoprene chemistry are further classified by the product generation in which HCHO is formed. 'Other' accounts for HCHO production from late-generation isoprene oxidation by OH,

including PAN degradation, and from isoprene oxidation by O_3, $O(^3P)$, and NO_3. Grouping individual rates is complex, as many reactions are common to different VOCs or are multi-generational. A description of our grouping scheme and a list of group assignments are provided in Appendix D.

The formulation of CB6r2 expands the simple isoprene scheme in CB05 to consider the NO_x-dependent reactivity of $ISOPO_2$ (Hildebrandt Ruiz and Yarwood, 2013). Fig. 3.6 shows that the updated chemistry increases the average production of HCHO by 0.06 ppb hr^{-1} (~5%), consistent with increased HCHO mixing ratios (Fig. 3.2). Formaldehyde production from first- and second-generation isoprene oxidation is actually reduced by 0.13 ppb hr^{-1} within CB6r2. Increases in the production of HCHO are attributed to methane, methanol, and late-generation isoprene oxidation chemistry. The increases from methane and methanol oxidation result from more efficient radical recycling: additional OH and HO_2 are returned to the system by new RO_2 reaction pathways and new isoprene oxidation products, such as HPALD. Increased recycling of both species leads to larger modeled mixing ratios of OH (Fig. 3.4), effectively increasing production of HCHO. Other updates within CB6r2 include the addition of new isoprene oxidation products – such as IEPOX and glycolaldehyde (GLYD) – that form HCHO in later generations. Several existing reactions were updated to add or increase formation of methyl peroxy radical (CH_3O_2), a major source of late-generation HCHO. The CH_3O_2 radical is also formed via RO_2+RO_2 chemistry, which is expanded in CB6r2 to account for new RO_2 species – such as $ISOPO_2$ and $IEPOXO_2$ – increasing the contribution to late-generation HCHO production even further. However, the cumulative increases in HCHO production from late-generation isoprene chemistry

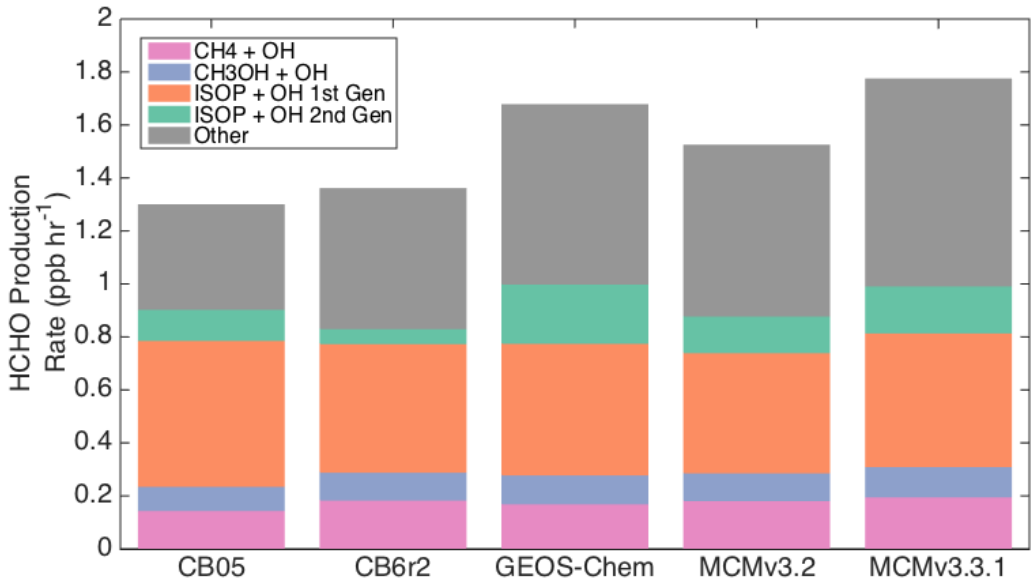

Fig. 3.6. Average HCHO production rates (ppb hr^{-1}) simulated for SENEX. Rates are grouped by contribution to HCHO production from methane, methanol, and isoprene oxidation (first- and second-generation). 'Other' accounts for HCHO production from late-generation isoprene oxidation by OH, including PAN degradation, and from multi-generational isoprene oxidation by O_3, $O(^3P)$, and NO_3.

barely outweigh the reductions from first- and second-generation chemistry, explaining why modeled HCHO rises so little between CB05 and CB6r2.

The MCMv3.3.1 mechanism builds on the complex isoprene scheme of MCMv3.2 and refines the chemistry for consistency with several recent laboratory and theoretical studies (Jenkin et al., 2015). The applied updates increase the average production of HCHO by 0.25 ppb hr^{-1} (~16%) between MCMv3.2 and MCMv3.3.1. New radical chemistry, $ISOPO_2$ isomers, and $ISOPO_2$ isomerization pathways in MCMv3.3.1 increase first-generation HCHO production from isoprene oxidation. Representation of minor OH-adducts in MCMv3.3.1 yields new first-generation oxidation products pent-4-en-2-one and 3-methyl-but-3-enal, which react to form HCHO in the second generation. Though the chemistry of these species is largely based

on theory (Park et al., 2003), it accounts for ~2% of total HCHO production in MCMv3.3.1 and ~88% of the increase in second-generation HCHO production between MCMv3.2 and MCMv3.3.1. Updates to the late-generation isoprene oxidation chemistry, however, are responsible for the largest increases in HCHO production, totaling 0.14 ppb hr^{-1}. For example, MCMv3.3.1 includes several new or enhanced sources of acetyl peroxy radical (CH_3CO_3), a precursor of PAN and CH_3O_2; furthermore, updated rate constants controlling PAN equilibria increase production of CH_3CO_3 from PAN by a factor of 2. These changes lead to increased production of CH_3O_2, and therefore HCHO, in the late stages of isoprene oxidation. Finally, larger OH mixing ratios in MCMv3.3.1 from additional radical recycling – mainly via RO_2 isomerization and HPALD photolysis – increase the production of HCHO from all source VOCs.

Though considered a condensed mechanism, GEOS-Chem v9-2+ contains a detailed isoprene scheme that was recently updated to incorporate results from a variety of studies (Fisher et al., 2016; Kim et al., 2015; Marais et al., 2016; Travis et al., 2016). Consequently, the average production of HCHO during SENEX approaches that of MCMv3.3.1 (1.68 and 1.77 ppb hr^{-1}, respectively), differing by only ~5%. The distribution of HCHO sources is also very similar. Cumulative production of HCHO from methane, methanol, and first-generation isoprene oxidation matches within 5%. However, GEOS-Chem exhibits more second-generation and less late-generation HCHO production compared to MCMv3.3.1. Because the representation of underlying chemistry is fundamentally different between condensed and explicit mechanisms, it is difficult to pinpoint causes of discrepancy. Nevertheless, broad comparison of major HCHO-producing reactions allows us to make some determinations. For instance,

HPALD photolysis is a much larger source of HCHO in GEOS-Chem than in MCMv3.3.1. Since J-values are consistent between simulations (Section 3.3.2), we attribute this discrepancy to differing yields of HCHO and HCHO precursors. Furthermore, HCHO production from HPALD photolysis is prompt (second-generation) in GEOS-Chem but delayed (late-generation) in MCMv3.3.1 due to formation of intermediate VOCs. The treatment of HPALD photolysis in GEOS-Chem thus contributes to more production of HCHO in the second generation. Late-generation HCHO production is limited by the production of CH_3O_2, which is 10% less in GEOS-Chem than in MCMv3.3.1. An evaluation of the CB mechanisms with respect to MCMv3.3.1 is presented in Section 3.5.

Differences in the generational distribution of HCHO production rates lead to discrepancies in the time-evolution of modeled HCHO (Fig. 3.7). A prior study by Marais et al. (2012) investigated the simulated yield of HCHO from isoprene oxidation as a function of time and under varying conditions for NO_x. We apply a similar approach to explore the temporal behavior of each of the five mechanisms considered in this work, and we find that modeled HCHO and its time progression vary between mechanisms and NO_x conditions, as in Marais et al. The influence of the distribution of HCHO production rates is manifested in the rate of change of HCHO mixing ratios throughout subsequent diel cycles. Though the mechanisms tend to deviate over time in all NO_x regimes, the greatest variation (~0.5 cumulative ppb HCHO per ppb initial isoprene) occurs in the high-NO_x simulation (1 ppb), which favors production of tropospheric ozone. Precisely representing the time-evolution of isoprene oxidation products such as HCHO and ozone is critical for effective air quality modeling.

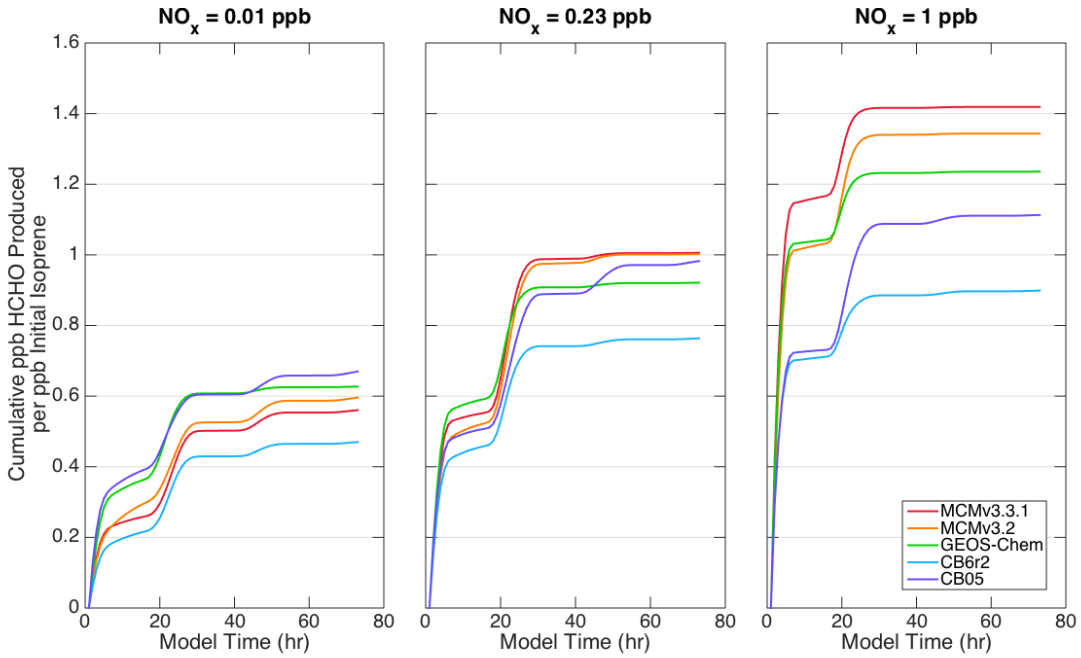

Fig. 3.7. Time-evolution of cumulative ppb HCHO produced per ppb initial isoprene, as modeled (colors, as indicated for each mechanism) for a sample point from SENEX under varying NO_x conditions. The simulations shown here follow the model setup described in Section 3.2, with two exceptions: constrained organic species are limited to isoprene only, and the mixing ratio of isoprene is allowed to decay freely after initialization. The simulated sample point is representative of high isoprene (8.15 ppb) and moderate NO_x (0.23 ppb) conditions. Low- and high-NO_x conditions (0.01 and 1 ppb, respectively) are achieved by scaling initial NO_x.

3.4.3 Uncertainties

As described in Section 3.3.1, the stated accuracy of ISAF HCHO is ±10%. This estimate comprises calibration uncertainty but does not account for interference from ISOPOOH, which has been shown to affect ISAF measurements of HCHO (St. Clair et al., 2016). Measurements of $C_5H_{10}O_3$ (lumped ISOPOOH and IEPOX) were obtained during SENEX via chemical ionization mass spectrometry (CIMS) (Warneke et al., 2016). Applying an ISOPOOH-to-HCHO conversion rate of 6%, which is recommended for ISAF under SENEX-like conditions (St. Clair et al., 2016), we

determine that ISOPOOH interference inflates measured HCHO by at most ~1% on average. A systematic 11% down-revision in observed HCHO mixing ratios, derived from combining calibration uncertainty and ISOPOOH interference, would not be sufficient to bring measured and modeled HCHO into agreement.

Modeled HCHO is also subject to uncertainty, which can arise from errors in the observational constraints. Stated accuracies for measurements of most constrained species are within 5% (Table 3.2), and we expect these uncertainties to have a minimal impact on modeled HCHO. However, larger uncertainties are reported for PAN (0.04–0.05 ppb, ~15%) and VOCs (25%), including isoprene and methanol. Sensitivity simulations show that systematic error in constrained PAN or methanol could explain about 10% of the discrepancy between measured and modeled HCHO, whereas error in constrained isoprene could account for nearly 50%. Depending on the mechanism used, the combination of a 25% increase in constrained isoprene with an 11% decrease in measured HCHO could bring model and measurements into agreement. However, the required correction of isoprene observations is not supported by recent instrument inter-comparison studies (Lerner et al., 2017; Warneke et al., 2016).

Modeled HCHO may also be limited by the choice of represented sources. Although HCHO is a pervasive byproduct of general VOC oxidation, our box model setup assumes that primary VOCs isoprene, methane, and methanol dominate the photochemical production of HCHO in the Southeast US. To test this assumption, we perform a simulation constrained to observations of primary VOCs collected by the improved whole air sampler (iWAS) during SENEX. The iWAS provides observations of 24 primary VOCs, including a variety of alkanes, alkenes, aromatics, and monoterpenes (Lerner et al., 2017; Warneke et al., 2016). Using the MCMv3.3.1

mechanism, which resolves explicit chemistry for most measured VOCs, we find that omission of observed primary VOCs explains <10% of the difference between modeled and measured HCHO. Observations of secondary VOCs MVK and MACR were also collected during SENEX, measured via iWAS analysis and proton-transfer-reaction mass spectrometry (PTR-MS). As first-generation products of isoprene oxidation, these species are useful in constraining HCHO production in later generations. However, the two sets of measurements do not agree, with lumped MVK and MACR measured ~30% higher by iWAS analysis (Lerner et al., 2017). Greater benefit to modeled HCHO is achieved by constraining to iWAS MVK and MACR, which improves model-measurement agreement by ~10%; however, due to potential ISOPOOH interference (Rivera-Rios et al., 2014), this effect is likely overestimated. We do not constrain to iWAS observations in the base model runs because iWAS sampling severely limits the size of our dataset (n = 62), but we conclude that, within measurement uncertainties, inclusion of all observed VOCs still cannot explain the HCHO model-measurement discrepancy.

Photochemical rate constants provide another source of model uncertainty. Based on our box model setup, photolysis frequencies are limited by uncertainties in constrained J-values (10%). Kinetic rate constants, on the other hand, are unique to each mechanism and are generally drawn from established databases such as the IUPAC Task Group on Atmospheric Chemical Kinetic Data Evaluation (http://iupac.pole-ether.fr/) or the JPL Data Evaluation (http://jpldataeval.jpl.nasa.gov/). Such databases combine information from laboratory and chamber studies to determine the "preferred value" of each rate constant. Uncertainties from the individual studies and their combination lead to uncertainties in the preferred values. Following the procedure

described in Appendix E, we estimate that uncertainty in photochemical rate constants produces ~12% (1σ) uncertainty in modeled HCHO mixing ratios for each of our box model simulations. This error is random and could imply better, or worse, model-measurement agreement than is indicated in Section 3.4.1.

3.5 Suggested modifications to CB6r2

The two mechanisms geared specifically towards air quality simulations, CB05 and CB6r2, underestimate HCHO by 33% and 32%, respectively. These results imply deficiencies in the same coupled chemical system that predicts ozone and SOA. Although CB05 is still widely used today, its isoprene scheme cannot be easily improved without first upgrading to CB6r2. The CB6r2 mechanism contains more developed isoprene chemistry and is thus more suitable for incorporating modifications. Here we present suggestions for improving simulated HCHO in CB6r2 and consider effects on modeled ozone.

We evaluate HCHO production rates in CB6r2 using MCMv3.3.1 as a benchmark. Average production of HCHO during SENEX is considerably lower in CB6r2 compared to MCMv3.3.1 (1.36 and 1.77 ppb hr^{-1}, respectively). Fig. 3.6 shows that cumulative production of HCHO from methane, methanol, and first-generation isoprene oxidation is comparable between CB6r2 and MCMv3.3.1, with the two values differing less than 5%. However, the production of HCHO from second- and late-generation isoprene oxidation is underestimated by CB6r2, relative to MCMv3.3.1, by a factor of 1.64. We find that CB6r2 omits HCHO production from both the 1,5-H shift and 1,6-H shift pathways of $ISOPO_2$ isomerization; in MCMv3.3.1, the 1,5-H shift

pathway contributes to first-generation HCHO production, the 1,6-H shift pathway to late-generation HCHO production. The CB6r2 mechanism also omits HCHO from the OH oxidation of MVK and MACR, a source of second-generation HCHO in MCMv3.3.1. Finally, CB6r2 omits or underestimates HCHO production from several late-generation reactions, including the OH oxidation of GLYD and the radical reactions of $IEPOXO_2$.

We recommend a set of modifications (Table 3.3) to address the underestimated production of HCHO in the second and late generations of isoprene oxidation within CB6r2. Modification 1 is intended to correct missing HCHO from $ISOPO_2$ isomerization. The existing 1,6-H shift pathway in CB6r2 produces HPALD and HO_2; subsequent HPALD photolysis forms MVK, MACR, and OH. Production of HCHO via 1,6-H shift isomerization is complex in MCMv3.3.1, so we look to GEOS-Chem for a condensed representation. Following v9-2+, we add HCHO to the products of HPALD photolysis with a yield of 100%. Though GEOS-Chem also includes production of HCHO from HPALD oxidation, the proposed modification to CB6r2

Table 3.3. Recommended modifications to CB6r2 that are incorporated into CB6r2-UMD. The parameter ΔP_{HCHO} quantifies the effect of each modification on the average HCHO production rate from SENEX.

Mod.	Description	ΔP_{HCHO} (ppb hr^{-1})	ΔP_{HCHO} (%)
1	Add HCHO as a product of HPALD + hν	0.11	8
2	Add HCHO as a product of MVK + OH and MACR + OH	0.07	5
3	Add HCHO as a product of GLYD + OH	0.05	4
4	Increase product fraction of HCHO in $IEPOXO_2$ + HO_2 and $IEPOXO_2$ + NO	0.05	4
5	Update PAN equilibrium rate constants according to IUPAC 2014	0.07	5
All	Implement Modifications 1-5 simultaneously	0.36	26

results in about the same average HCHO production as the combined HPALD reactions in GEOS-Chem (0.11 and 0.08 ppb hr^{-1}, respectively). Production of HCHO via 1,5-H shift isomerization of $ISOPO_2$ is also expected. However, representation of this pathway in MCMv3.3.1 accounts for a small fraction of total HCHO production (~1%), and we refrain from adding entirely new reactions to CB6r2 due to the complications of implementing such changes in CTMs. All of the other recommended modifications are supported by related studies. For example, including HCHO production from the OH oxidation of MVK and MACR (Modification 2) and the OH oxidation of GLYD (Modification 3) is consistent with the isoprene oxidation scheme proposed by Paulot et al. (2009a), upon which the isoprene chemistry of CB6r2 is based (Hildebrandt Ruiz and Yarwood, 2013). Modification 4 derives from the recent work of Bates et al. (2014), who discovered new products of IEPOX oxidation (C_4 hydroxy dicarbonyl and C_4 dihydroxy carbonyl compounds), which upon subsequent reaction, are thought to form HCHO. Finally, Modification 5 simply applies the most recent evaluation of the PAN equilibrium rate constants from IUPAC (Atkinson et al., 2006) (corresponding data sheets at http://iupac.pole-ether.fr/htdocs/datasheets/pdf/ROO_14_CH3CO3_NO2_M.pdf and http://iupac.pole-ether.fr/htdocs/datasheets/pdf/ROO_15_CH3C(O)O2NO2_M.pdf).

The recommended modifications require only minor adjustments to the existing CB6r2 mechanism (Table 3.4). We refer to the adjusted CB6r2 as 'CB6r2-UMD.' As shown in Fig. 3.8, modeled HCHO improves significantly in CB6r2-UMD relative to CB6r2. Panel a) shows a scatter plot of modeled HCHO (ppb) versus measured HCHO

Table 3.4. Modified reactions in CB6r2 that are incorporated into CB6r2-UMD.

Reaction No.	Reactants and Products	Rate Constant Expression	Reference
54	C2O3 + NO2 = PAN	Falloff: F = 0.3; n = 1.41 k(0) = 3.28E−28 (T/300)^−6.87 k(inf) = 1.125E−11 (T/300)^−1.105	Atkinson et al., 2006
55	PAN = NO2 + C2O3	Falloff: F = 0.3; n = 1.41 k(0) = 1.10E−5 exp(−10100/T) k(inf) = 1.9E17 exp(−14100/T)	Atkinson et al., 2006
113	GLYD + OH = 0.2 GLY + 0.2 HO2 + 0.8 FORM	k = 8.00E−12	Paulot et al., 2009
158	ISPD + OH = 0.022 XO2N + 0.521 XO2 + 0.115 MGLY + 0.115 MEO2 + 0.269 GLYD + 0.269 C2O3 + 0.457 OPO3 + 0.117 FORM + 0.137 ACET + 0.137 CO + 0.137 HO2 + 0.658 RO2	k = 5.58E−12 exp(511/T)	Paulot et al., 2009
163	HPLD + hν = OH + ISPD + FORM	Photolysis	Stavrakou et al., 2010
166	EPX2 + HO2 = 0.275 GLYD + 0.275 GLY + 0.275 MGLY + 1.125 OH + 0.825 HO2 + 0.815 FORM + 0.074 FACD + 0.251 CO + 1.735 PAR	k = 7.43E−13 exp(700/T)	Bates et al., 2014
167	EPX2 + NO = 0.275 GLYD + 0.275 GLY + 0.275 MGLY + 0.125 OH + 0.825 HO2 + 0.848 FORM + NO2 + 0.251 CO + 1.702 PAR	k = 2.39E−12 exp(365/T)	Bates et al., 2014

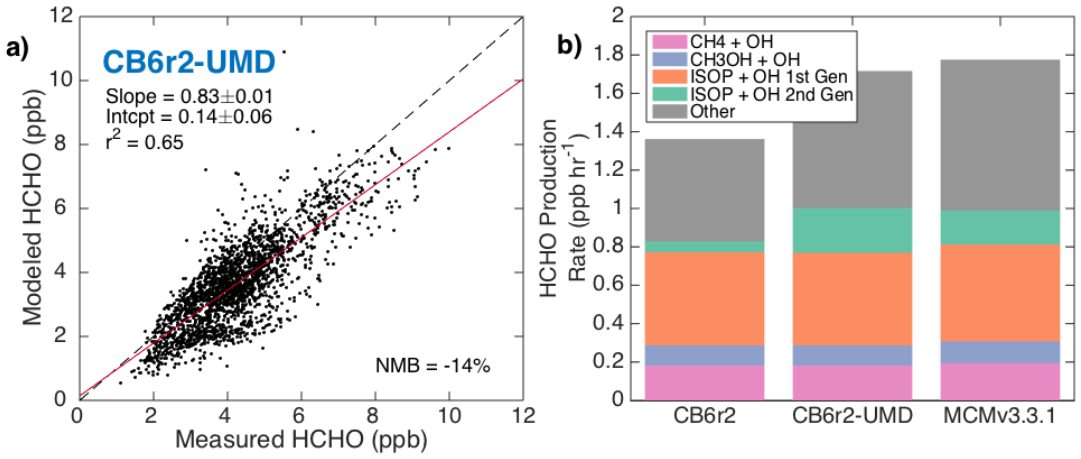

Fig. 3.8. a) Regression of modeled and measured mixing ratios of HCHO (ppb) from SENEX, where HCHO is modeled using CB6r2-UMD. Linear least-squares regression analysis provides parameters for a line of best fit, which is plotted in red. The 1:1 line, shown here as a dashed black line, is provided for reference. All uncertainties are 1σ standard deviations. b) Average HCHO production rates (ppb hr^{-1}) simulated for SENEX using CB6r2, CB6r2-UMD, and MCMv3.3.1. Rates are grouped by contribution to HCHO production from methane, methanol, and isoprene oxidation (first- and second-generation). 'Other' accounts for HCHO production from late-generation isoprene oxidation by OH, including PAN degradation, and from multi-generational isoprene oxidation by O_3, $O(^3P)$, and NO_3.

(ppb). Linear regression yields a line of best fit with a slope of 0.83 ± 0.01, and we calculate an NMB of −14%, which indicates that model-measurement agreement is comparable to MCMv3.3.1. Panel b) shows that average HCHO production increases 0.36 ppb hr^{-1} (~26%) in CB6r2-UMD relative to CB6r2, and that the total production rate of HCHO is within ~3% of MCMv3.3.1. The distribution of HCHO production rates among source VOCs roughly imitates that of MCMv3.3.1: Modifications 1 and 2 contribute to HCHO production from second-generation isoprene oxidation, whereas Modifications 3 through 5 contribute to HCHO production in later generations. Our proposed CB6r2-UMD mechanism thus effectively simulates the isoprene-HCHO relationship of more complex mechanisms while retaining the computational efficiency of CB6r2.

Although CB6r2-UMD improves modeled HCHO compared to other mechanisms, it is still biased low by 14% compared to measured mixing ratios of HCHO from SENEX. This deficit is consistent with our findings from Section 3.4.1, which revealed a negative bias in modeled HCHO relative to observations, common to all considered mechanisms. Potential sources of this bias, discussed in Sections 3.4.1 and 3.4.3, are difficult to evaluate using a box model. However, we leverage our CB6r2-UMD simulation to determine whether we can reduce the bias through the manipulation of mechanism reaction rates, within accepted uncertainties. We begin by identifying the reactions in CB6r2-UMD to which modeled HCHO is most sensitive (Appendix E). Of these, only the thermal degradation of PAN has enough influence on modeled HCHO to eliminate model-measurement bias when the corresponding rate constant is perturbed within its 2σ uncertainty limits; however, model-measurement agreement is not achieved for HCHO or PAN, when PAN is unconstrained (Fig. 3.9). The next most important reaction is the OH oxidation of HCHO, which must be perturbed by a factor of 2 – significantly past its 2σ rate constant uncertainty limits (~20% at 298 K) – to match modeled and measured mixing ratios of HCHO (not shown). These results suggest that the detected bias in modeled HCHO cannot be corrected by a simple adjustment of rate parameters, but rather that continued investigation is required to isolate its cause and formulate meaningful solutions.

As we are still unable to match simulated HCHO mixing ratios to observations, we perform a CB6r2-UMD simulation constrained to measured mixing ratios of HCHO

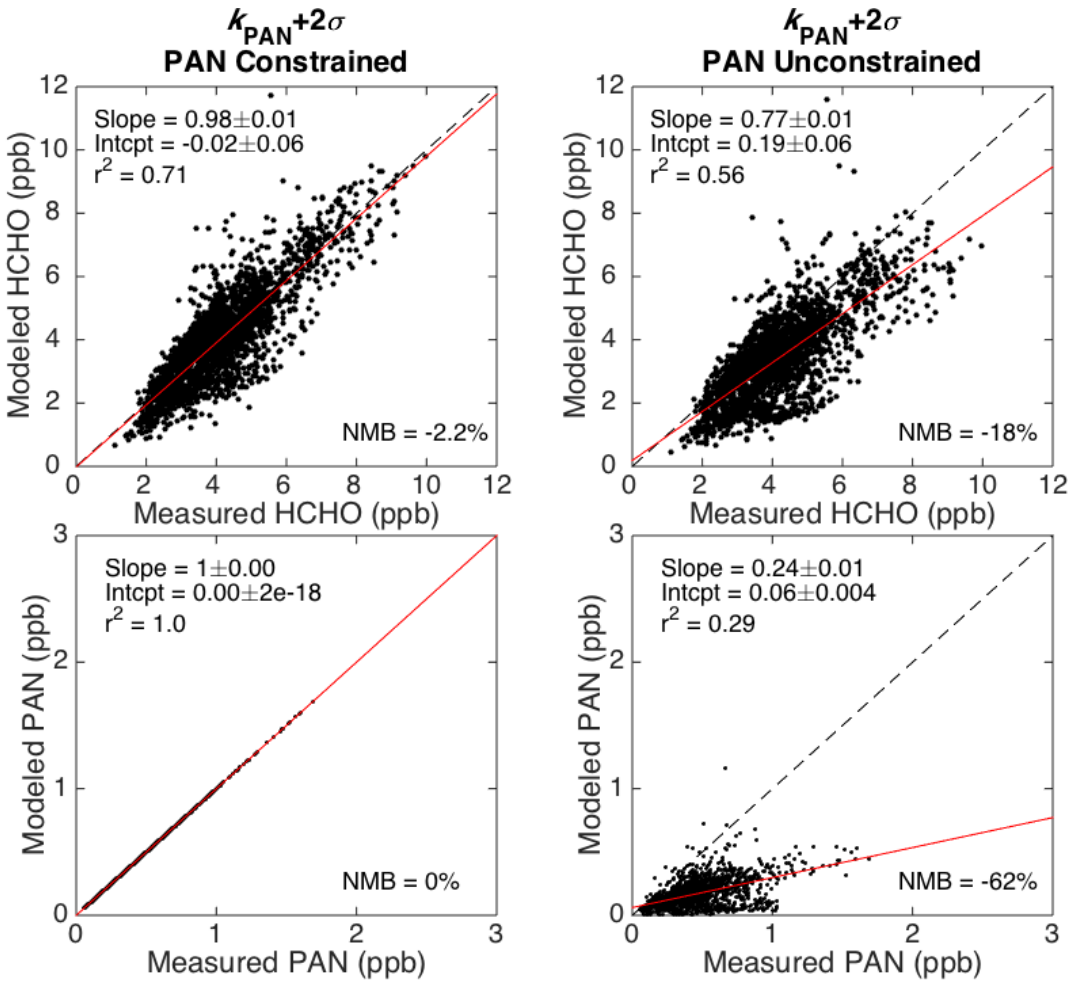

Fig. 3.9. Regression of modeled and measured mixing ratios of HCHO (ppb) and PAN (ppb) from SENEX. All panels feature a variation on the CB6r2-UMD mechanism in which the rate constant for the thermal degradation of PAN (k_{PAN}) is increased to its upper 2σ uncertainty limit: the left column shows results from a simulation in which PAN is constrained, the right from a simulation in which PAN is unconstrained. For each comparison, linear least-squares regression analysis provides parameters for a line of best fit, which is plotted in red. The 1:1 line, shown here as a dashed black line, is provided for reference. All uncertainties are 1σ standard deviations.

from SENEX, which allows us to assess consequences for the calculated production rate of tropospheric ozone. Formaldehyde degrades to form HO_2, which leads to production of ozone in the presence of NO_x. Changes in HCHO, therefore, impact the first term in the following equation for ozone production:

$$P(O_3) = k_{HO2+NO}[HO_2][NO] + \sum k_{RO2i+NO}[RO_{2i}][NO] \quad (3.2)$$

where $P(O_3)$ is the ozone production rate (molecules cm^{-3} s^{-1}), k_{HO2+NO} and $k_{RO2i+NO}$ are reaction rate constants (cm^3 $molecule^{-1}$ s^{-1}), and $[HO_2]$, $[RO_{2i}]$, and [NO] are species concentrations (molecules cm^{-3}). The subscript *i* denotes the separation of RO_2 into individual species for calculation of the second term. Fig. 3.10 illustrates how ozone production responds to differences in modeled HCHO. Ozone production rates (in ppb hr^{-1}) are calculated for SENEX using model output from the CB6r2, CB6r2-UMD, and constrained CB6r2-UMD simulations. These are then plotted as a function of NO (ppb). Increased mixing ratios of HCHO strengthen the NO-dependence of the ozone production rate, increasing ozone production at ~0.3 ppb NO by 0.24 ppb hr^{-1} (~3%) between CB6r2 and CB6r2-UMD and 0.38 ppb hr^{-1} (~4%) between CB6r2-UMD and the constrained CB6r2-UMD simulation. The "missing HCHO" represented

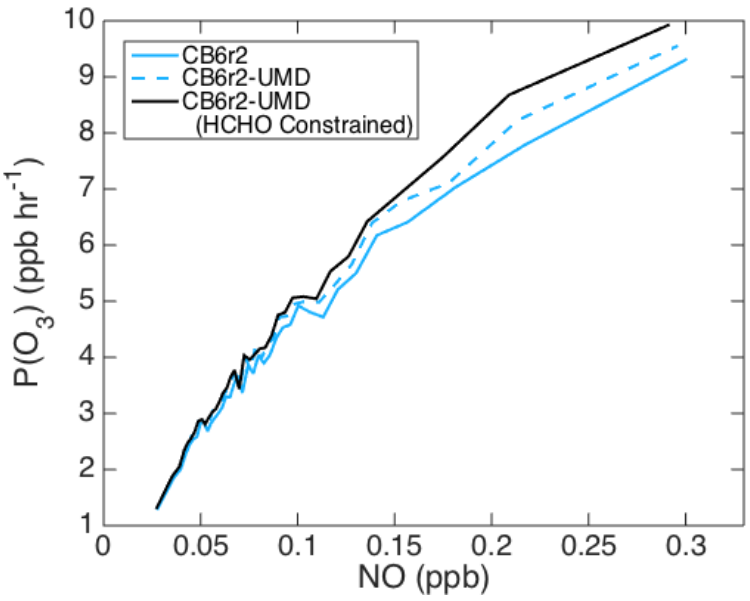

Fig. 3.10. Ozone production rate (ppb hr^{-1}) as a function of NO (ppb) calculated for SENEX using model output from three different simulations: CB6r2 (blue), CB6r2-UMD (blue dashed), and CB6r2-UMD constrained to observations of HCHO (black). Calculated rates are binned by NO, with each bin containing 60 points. Lines represent bin averages.

by the constrained simulation implies a deficit of VOC oxidation, affecting all of the mechanisms investigated in this study, that directly impacts the production of tropospheric ozone.

Chemical transport models tend to overestimate surface ozone in the summertime Southeast US (Canty et al., 2015; Fiore et al., 2003; Reidmiller et al., 2009). In a recent study, Travis et al. (2016) investigated this phenomenon using the GEOS-Chem CTM with v9-2+ chemistry. Their study supports the recent discovery that non-power plant NO_x emissions are overestimated in most CTMs (Anderson et al., 2014; Castellanos et al., 2011; Fujita et al., 2012), and shows that reducing mobile and industrial NO_x emissions by 60% improves agreement between modeled and measured ozone mixing ratios at the surface. However, their model remains biased high by 6 ± 14 ppb, which Travis et al. attribute to excessive vertical mixing and undiagnosed ozone chemistry. Our results show that improving modeled HCHO in the summertime Southeast US increases simulated ozone production by up to ~7%. These results are representative of boundary layer conditions; however, excessive vertical mixing may well extend the influence of our modifications to the surface, potentially worsening agreement between modeled and measured ozone mixing ratios. The resulting discrepancy in surface ozone is expected to be partly balanced by implementation of halogen chemistry (Sherwen et al., 2016). But despite the potential ramifications for modeled ozone mixing ratios, our proposed changes demonstrate improved model representation of ozone precursors, which are important in the development of air quality policy.

As a final note, two new revisions to the CB6 mechanism have been recently released: CB6r3 and CB6r4. Updates in CB6r3 account for the temperature-dependence of alkyl nitrate yields, which improves simulated ozone production rates at low temperatures, for example during wintertime (Emery et al., 2015). The subsequent revision, CB6r4, incorporates the same updates from CB6r3, removes VOC oxidation by $O(^3P)$, includes pseudo-heterogeneous hydrolysis of ISOPN, and adds a 16-reaction condensed iodine mechanism (Environ, 2016). We have performed SENEX simulations using both CB6r3 and CB6r4 (excluding halogen chemistry), and we find that the changes incorporated into each revision have a negligible (<1%) impact on modeled HCHO mixing ratios compared to CB6r2 (Fig. 3.11). We deduce that our suggested modifications put forth for CB6r2 apply also to CB6r3 and CB6r4, and for the summertime Southeast US, will produce nearly identical results with respect to simulated HCHO and its contribution to the production of tropospheric ozone.

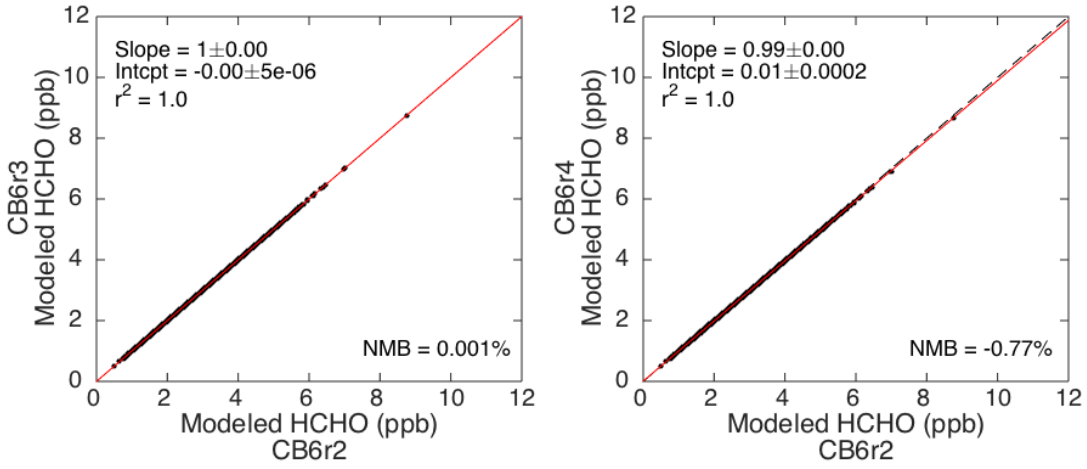

Fig. 3.11. Regression of mixing ratios of HCHO (ppb) modeled for SENEX using CB6r3 (left) and CB6r4 (right) versus mixing ratios of HCHO (ppb) modeled using CB6r2. For each comparison, linear least-squares regression analysis provides parameters for a line of best fit, which is plotted in red. The 1:1 line, shown here as a dashed black line, is provided for reference. All uncertainties are 1σ standard deviations.

3.6 Conclusions

In situ observations and a constrained 0-D box model were used to evaluate and inter-compare the isoprene schemes of the CB05, CB6r2, GEOS-Chem, MCMv3.2, and MCMv3.3.1 gas-phase chemical mechanisms. Comparison of modeled HCHO to measurements obtained during SENEX showed that, in general, mechanisms containing more developed isoprene oxidation chemistry (e.g., chemically explicit or recently updated) tend to simulate HCHO more accurately; however, all mechanisms were found to underestimate measured HCHO by at least 15%. The GEOS-Chem mechanism, which is used to estimate isoprene emissions from remote measurements of HCHO, achieves relatively high model-measurement agreement with an NMB of −17%. The CB05 and CB6r2 mechanisms, though often used in air quality simulations, underestimate measured HCHO by 33% and 32% respectively, which directly impacts modeled ozone.

Inter-comparison of reaction rates revealed that major restructuring of the CB isoprene scheme produces cancelling effects on HCHO production rates, so that the average production of HCHO simulated for SENEX increases only ~5% from CB05 to CB6r2. In contrast, further refinement of the complex MCM scheme increases average production of HCHO by ~16%, leading to larger modeled HCHO mixing ratios in MCMv3.3.1 relative to MCMv3.2. The GEOS-Chem mechanism, though considered condensed, provides a good approximation of the explicit isoprene chemistry in MCMv3.3.1, and reproduces average HCHO production rates within ~5%. Cumulative HCHO production from methane, methanol, and first-generation isoprene oxidation chemistry is fairly consistent between all five mechanisms, but responds to changes in radical recycling. Disagreement in the simulated production of HCHO is mainly

attributed to second- and late-generation isoprene oxidation chemistry, which varies between mechanisms according to level of detail and inclusion of updates from relevant studies.

We recommend improvements to CB6r2, which has the greatest potential to impact air quality management. Evaluation of CB6r2 against MCMv3.3.1 exposes shortcomings in the isoprene scheme of CB6r2 that limit the amount of HCHO produced via isoprene oxidation. Based on these shortcomings, we propose a few simple modifications to CB6r2 (Table 3.3), referred to as CB6r2-UMD, that mimic HCHO production in MCMv3.3.1 and improve agreement with SENEX observations to −14%. These modifications are intended for implementation in CTMs, which remains to be tested. The CB6r2 mechanism is currently publicly available for use within the Comprehensive Air Quality Model with Extensions (CAMx) (http://www.camx.com/), and CB6r3 accompanied the recent release of version 5.2 of the Community Multiscale Air Quality (CMAQ) model (https://www.cmascenter.org/cmaq/). Implementation of CB6r2-UMD in a CTM such as CAMx or CMAQ will provide a means to assess the effects of improved simulation of HCHO on regional air quality modeling.

While CB6r2-UMD demonstrates improvement in the simulation of HCHO, it still underestimates measured mixing ratios by 14%, which is consistent with a negative bias affecting all of the gas-phase chemical mechanisms considered in this study. We do not propose a solution to correct this bias, but rather acknowledge its presence and recommend continued investigation. Lacking a simulation that matches measured HCHO mixing ratios, we performed a simulation constrained to observed HCHO from SENEX to evaluate the effects of improving HCHO on modeled ozone. Increased

production of HCHO in CB6r2-UMD relative to CB6r2 increased the production of ozone by ~3% at 0.3 ppb NO; ozone production increased another ~4% when constrained to observed HCHO. The ozone production rates reported here are averaged across the SENEX campaign, which may dampen effects in high-NO_x urban regions where nonlinearities in the ozone chemistry could lead to a stronger dependence on HCHO. Individual case studies in combination with ozone sensitivity tools may provide a more precise characterization of the relationship between HCHO and ozone in these areas.

We conclude by noting that we are generally reassured by how well the various mechanisms simulate isoprene oxidation products such as HCHO and ozone. Isoprene oxidation chemistry is extremely complex, and implementation in air quality models is complicated by the need to have a computationally efficient scheme, given the high spatial and temporal resolution of typical CTM runs. The scientific understanding of isoprene oxidation chemistry is constantly evolving, and the development of atmospheric models is an ongoing process. Current gas-phase chemical mechanisms exhibit considerable skill in simulating observed HCHO. Though presently biased low, these mechanisms improve with each revision and continue to approach agreement with observations.

Chapter 4: Impact of improved isoprene mechanisms on regional modeling of ozone and its precursors

This chapter is in preparation for publication under the same title, as an article that will be submitted to the scientific journal *Atmospheric Environment*. I will be the lead author of this work, and I acknowledge collaboration with 23 co-authors, who form a network of support connecting colleagues at the University of Maryland, air quality modelers at the EPA, developers of the F0AM box model, and participants in the SENEX aircraft campaign. Here, the numbering of sections, figures, and tables reflects incorporation into the greater dissertation. The supplemental material from the article is distributed throughout the chapter.

4.1 Introduction

Ozone (O_3) is an important gas-phase atmospheric constituent that can be detrimental to climate and public health (EPA, 2013; IPCC, 2013). Designated a criteria pollutant by the US Environmental Protection Agency (EPA), ground-level ozone is federally mandated to meet a National Ambient Air Quality Standard (NAAQS) of 70 ppb, evaluated as a three-year average of the annual fourth-highest daily 8-hour maximum ozone concentration (https://www.epa.gov/criteria-air-pollutants/naaqs-table). Ozone is measured at surface monitoring sites across the US; however, many sites fail to meet the 70 ppb standard, especially near expansive urban areas such as Los Angeles, Houston, and New York City, (https://www3.epa.gov/airquality/greenbook/jnc.html). Air quality policy is continuously evolving to achieve compliance

with the NAAQS, which have evolved to meet lower ozone thresholds as air quality has improved. Surface ozone concentrations have declined due to reduced emissions of the precursor species that control the secondary production of tropospheric ozone, namely volatile organic compounds (VOC) and nitrogen oxides (NO_x = NO + NO_2) (Goldberg et al., 2015; Hogrefe et al., 2011; Simon et al., 2015).

Surface concentrations of ozone are predominantly attributed to secondary photochemical production, with a nonlinear dependence on concentrations of VOCs and NO_x. Tropospheric production of ozone is initiated by the generation of the OH radical, following photolysis of ozone (tropospheric or stratospheric) or conversion from HO_2 (Jacob, 1999; Thornton et al., 2002). The OH radical oxidizes VOCs in sunlight to produce the organic peroxy radical (RO_2), which may experience varying photochemical fates depending on conditions for NO_x. In the absence of NO_x, RO_2 reacts with available radicals such as HO_2 or even another molecule of RO_2 in a manner that leads to organic degradation without production of ozone. In the presence of NO_x, RO_2 may react with NO to form an organic oxy radical (RO) and NO_2. The RO radical subsequently degrades to form smaller oxidized organic compounds and the HO_2 radical, which also reacts with NO to produce NO_2. The resulting NO_2 then photolyzes in air to produce ozone. Radical termination is achieved by reactions between HO_x (HO_x = OH + HO_2) radicals, or if NO_x concentrations are high enough, by reactions between HO_x and NO_x. Tropospheric production of ozone therefore varies with concentrations of both VOCs and NO_x, considered NO_x-limited when radical termination is controlled by HO_x radicals and VOC-limited when radical termination involves NO_x (Sillman, 1999, 1995; Sillman et al., 1990).

Isoprene (C_5H_8) is a primary VOC that can influence local ozone production significantly. The major source of isoprene is biogenic emission, with global annual emissions totaling nearly ~500 Tg yr^{-1}, about half of all biogenic VOC emissions and one third of all non-methane VOC emissions (Guenther et al., 2012). Isoprene is a conjugated diene with a lifetime of <1–3 hr against OH. The oxidation of isoprene by OH proceeds following the general reaction scheme outlined above, with the fate of the isoprene hydroxy peroxy radical ($ISOPO_2$) characterized by a strong dependence on NO_x (Wolfe et al., 2016a). In addition to the NO, HO_2, and RO_2 reaction channels, isomerization by intramolecular hydrogen transfer is another potential fate for $ISOPO_2$, achieved via either 1,5-H or 1,6-H shift (Da Silva et al., 2010; Peeters et al., 2009). First-generation isoprene oxidation products depend upon the favored reaction pathway for $ISOPO_2$: isoprene nitrates (ISOPN) are formed by the reaction with NO (Paulot et al., 2009a), isoprene hydroxy hydroperoxides (ISOPOOH) by reaction with HO_2 (Paulot et al., 2009b), hydroperoxyenals (HPALD) by 1,6-H shift (Crounse et al., 2011; Peeters et al., 2014), and both methyl vinyl ketone (MVK) and methacrolein (MACR) by reaction with NO, reaction with RO_2, or 1,5-H shift (Jenkin et al., 2015, 1997; Paulson and Seinfeld, 1992; Saunders et al., 2003). Formaldehyde (HCHO) is a small oxygenated VOC that is co-produced with MVK and MACR in the first generation of isoprene oxidation and is also produced from the degradation of these and other isoprene oxidation products throughout the isoprene cascade. The acyl peroxy radical (CH_3CO_3) also forms throughout the isoprene oxidation chain, and either reacts reversibly with NO_2 to produce peroxy acetyl nitrate (PAN) or degrades to produce HCHO and other products (Fischer et al., 2014; Jacob, 1999; Lafranchi et al., 2009).

Regional air quality models simulate the complex relationships between ozone, NO_x, and VOCs like isoprene, which makes them useful tools in the development of air quality policy and ozone management strategies. Models in frequent use today include the Comprehensive Air Quality Model with Extensions (CAMx) (www.camx.com), the Community Multiscale Air Quality (CMAQ) model (https://www.cmascenter.org/cmaq/), and GEOS-Chem (http://acmg.seas.harvard.edu/geos/). These models represent atmospheric chemistry in a three-dimensional framework and consider multiple physiochemical processes that may affect the concentrations of aerosol and gas-phase species, including chemistry, emissions, deposition, and transport. Although regional air quality models sometimes agree well with observations of ozone, ozone precursors are often misrepresented, likely stemming from uncertainties in their emissions and chemistry (Canty et al., 2015; Goldberg et al., 2016). For example, the National Emissions Inventory (NEI), which provides anthropogenic emissions for most air quality models, has been shown to overestimate emissions of NO_x from mobile and industrial sources, leading to high modeled NO_x concentrations in urban areas compared to *in situ* and remote observations (Anderson et al., 2014; Canty et al., 2015; Travis et al., 2016). Emissions for biogenic species are often prepared using either the Model of Emissions of Gases and Aerosols from Nature (MEGAN) (Guenther et al., 2012) or the Biogenic Emissions Inventory System (BEIS) (Bash et al., 2016), which produce isoprene emissions that differ up to a factor of two (Carlton and Baker, 2011; Warneke et al., 2010). Furthermore, several gas-phase mechanisms are available for incorporation into air quality models, each providing a simplified and unique representation of isoprene oxidation chemistry (Carter, 2010; Stockwell et al., 1997; Whitten et al., 1996), which can affect modeled concentrations

of NO_x and secondary VOCs such as HCHO (Archibald et al., 2010b; Marvin et al., 2017; Pöschl et al., 2000; von Kuhlmann et al., 2004; Zhang et al., 2011). Accurate representation of ozone precursors by air quality models is crucial to the development of effective strategies for controlling surface ozone.

Efforts are made continuously to improve the representation of VOCs and NO_x in regional air quality models. For example, anthropogenic emissions from the NEI are revised when new information becomes available (EPA, 2015a), the biogenic emissions models MEGAN and BEIS improve agreement with observations with every new version released (Bash et al., 2016; Guenther et al., 2012), and gas-phase chemical mechanisms evolve to reflect current literature (Yarwood et al., 2010, 2005). In a recent study, we inter-compared isoprene oxidation schemes between versions of a few different gas-phase mechanisms (Marvin et al., 2017), including the Carbon Bond (CB) mechanism, which is available for implementation in both the CAMx and CMAQ regional models. Mechanisms were tested using a 0-dimensional photochemical box model and evaluated against *in situ* observations of HCHO from the Southeast Nexus (SENEX) aircraft campaign. We found that CB6r2, a recent CB version (Hildebrandt Ruiz and Yarwood, 2013; Yarwood et al., 2010), fails to improve simulated HCHO, despite significant updates to its isoprene chemistry compared to its predecessor CB05 (Yarwood et al., 2005). Consequently, we suggested a few simple modifications to CB6r2, in an updated version called 'CB6r2-UMD', that were specifically targeted to improve the model representation of HCHO production from isoprene oxidation. Within the box model framework, the modifications incorporated into CB6r2-UMD substantially improved agreement with HCHO observations, increasing the normalized mean bias (NMB) of the mechanism from −32% to −14%, on par with more recent and

detailed mechanisms such as GEOS-Chem version 9-2+ (Fisher et al., 2016; Kim et al., 2015; Mao et al., 2013b; Marais et al., 2016; Travis et al., 2016) and the Master Chemical Mechanism (MCM) version 3.3.1 (Jenkin et al., 2015).

This work applies improved isoprene chemistry, following the modifications recommended in CB6r2-UMD, to a regional modeling framework and quantifies consequences for ozone, NO_x, and relevant VOCs. We use CAMx as our regional model, primarily because CB6r2 comes standard with recent versions. First, we must describe additional modifications to CB6r2-UMD that become important in the regional modeling environment. This provides us with three mechanisms to implement in successive model simulations: CB6r2, CB6r2-UMD, and an updated version of CB6r2-UMD that we call CB6r2-UMD*. For consistency with Marvin et al. (2017), simulated mixing ratios of ozone and its precursors are evaluated using observations from the SENEX aircraft campaign. Additionally, we use CAMx process analysis tools to explore effects on relevant reaction rates and ozone production indicators. Implications for isoprene emission inventories, NO_x emission inventories, and surface ozone management strategies are also discussed.

4.2 Methods

4.2.1 Aircraft observations

The SENEX aircraft campaign provides *in situ* observations of ozone and ozone precursors from the summertime Southeast US, which is abundant in isoprene (up to ~8 ppb) and varied in ozone production conditions. The National Oceanic and Atmospheric Administration (NOAA) supported 20 flights of the WP-3D research

aircraft between May 29 and July 10 of 2013, with corresponding flight tracks as shown in Fig. 4.1. To meet the mission objective of chemical and aerosol characterization, the aircraft payload included instrumentation to measure ozone, NO_x, and an expansive suite of VOCs. We use data from the 60-second average merge files (revision RD) that are available for download from http://www.esrl.noaa.gov/csd/projects/senex/. Instrumentation for key measurements used in this study are listed in Table 4.1, adapted from a SENEX overview paper by Warneke et al. (2016).

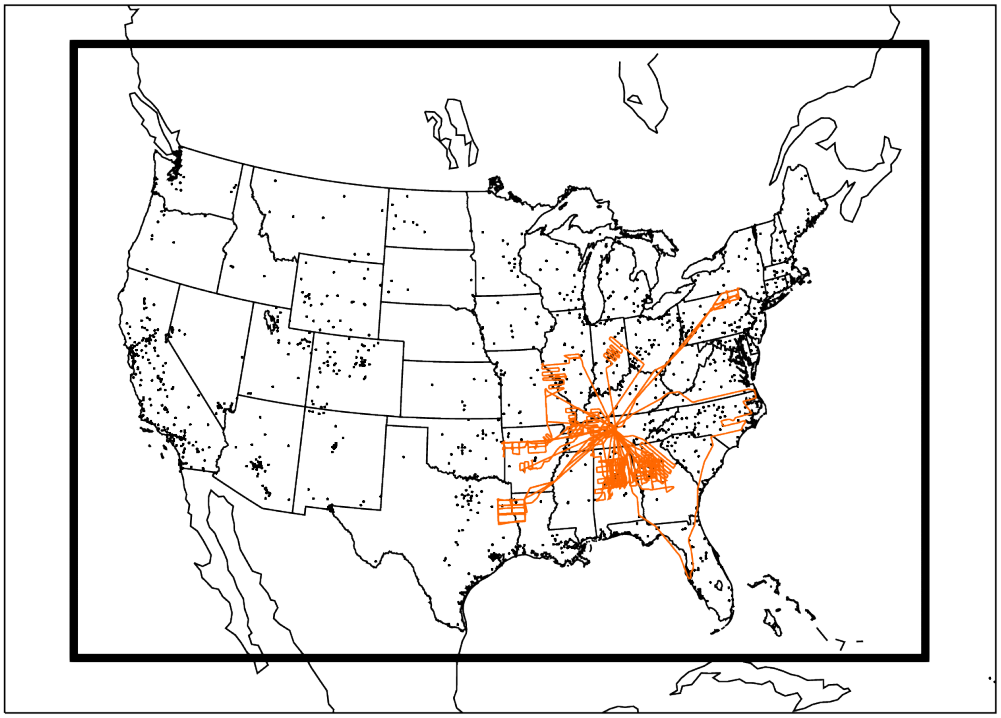

Fig. 4.1. Map of the continental United States. Flight tracks from the SENEX aircraft campaign are plotted in orange, locations for AQS monitors that collected ground measurements of ozone in 2013 are indicated by black dots, and the boundaries from our CAMx model simulations are denoted by the thick black border.

Table 4.1. Instrumentation for the SENEX observations used in this work (adapted from Warneke et al., 2016).

Measurement	Technique	Accuracy
O_3; NO; NO_2; NO_y	Chemiluminescence (CL)	2%; 3%; 4%; 12%
ISOP	Proton-transfer-reaction mass spectrometry (PTR-MS)	25%
HCHO	Laser-induced fluorescence (LIF)	10%
PAN; PPN; APAN	Chemical ionization mass spectrometry (CIMS)	15% + 10 ppt; + 3 ppt; + 6 ppt

The SENEX payload featured multiple techniques for measuring ozone and NO_x, including gas-phase chemiluminescence (CL), cavity ring down absorption spectroscopy (CRDS), and airborne cavity-enhanced absorption spectroscopy (ACES). Ozone and NO were measured only via CL and CRDS, whereas NO_2 was measured using all three techniques. Accuracies differ among the three instruments, with CL reporting the smallest uncertainty (O_3: ±2%, NO: ±3%; NO_2: ±4%) (Ryerson et al., 2000, 1999, 1998). Here and elsewhere, all reported uncertainties are 1σ. Ozone and NO_2 measurements from the different SENEX instrumentation were inter-compared previously by Warneke et al. (2016), who found CL to measure consistently higher than both CRDS (NO_2: 6%; O_3: 8%) and ACES (NO_2: 10%), but generally within or approaching the combined instrument uncertainties for each species. Degradation of the detection limit within the CRDS instrument prohibited inter-comparison of the two different measurements of NO. For consistency with Marvin et al. (2017), we prefer to use the CL measurements of ozone and NO_x; however, we investigate inter-instrument variability in our uncertainty analysis, presented in Section 4.4.3.

This study utilizes SENEX observations of select VOCs, including isoprene, HCHO, and peroxy nitrates (PN). Isoprene was sampled *in situ* via proton-transfer-reaction mass spectrometry (PTR-MS) (de Gouw and Warneke, 2007) and collected in canisters by an improved whole air sampler (iWAS) for post-flight analysis by gas chromatography - mass spectrometry (GC-MS) (Gilman et al., 2009; Lerner et al., 2017). The PTR-MS instrument obtains a greater density of data points by sampling at a higher frequency (~0.06 Hz) compared to the iWAS (up to 72 canisters per flight), but it is also less accurate (PTR-MS: ±25%; iWAS: ±12–20%). The two techniques were compared by Warneke et al. (2016), with iWAS/GC-MS shown to measure isoprene 8% higher than PTR-MS, well within stated uncertainties. We prefer to use the PTR-MS measurements of isoprene for consistency with Marvin et al. (2017). Formaldehyde was measured by the NASA In Situ Airborne Formaldehyde (ISAF) instrument, which operates via laser-induced fluorescence (LIF) detection (Cazorla et al., 2015), with a reported accuracy of ±10%. Certain PN species including PAN, PPN, and APAN were measured via chemical ionization mass spectrometry (CIMS), with reported accuracies of ±(15% + detection limit) for each species (Veres and Roberts, 2015), where detection limits are 10, 3, and 6 ppt, respectively.

We filter the SENEX observations to emphasize daytime (SZA < 70°), boundary-layer (altitude < 1500 m) conditions, and to exclude data affected by biomass burning (CO > 300 ppb or acetonitrile > 0.5 ppb) or fresh NO_x sources ($NO_x > 95^{th}$ percentile). In order to maintain consistency with Marvin et al. (2017), we also exclude data that coincide with missing or negative measurements of the model constraints from that study, which results in a total of 2219 data points for all observed species.

4.2.2 Ground-based observations

The air quality system (AQS), maintained by the EPA, provides surface observations of ozone at monitoring locations across the continental US (Fig. 4.1). Although measurements of ozone may be obtained by different methods throughout the AQS, most of the measurements we use are obtained using ultraviolet (UV) absorption spectrometry and are considered accurate within ±5 ppb. Hourly ozone data are acquired online from: http://www.epa.gov/ttn/airs/aqsdatamart.

4.2.3 Regional model

We run CAMx version 6.50 at hourly, 12 km resolution to simulate atmospheric composition during SENEX. Simulations span the continental US for May 21 – July 15 of 2013, coincident with observations and allowing for at least one week of model spinup. Fig. 4.1 maps the boundaries of the model domain, which extends 35 layers in the vertical up to ~100 mb.

All major model inputs were originally prepared for compatibility with CMAQ versions 5.0+ to support ongoing studies conducted by the EPA (Pye et al., 2018, 2015). Meteorology is driven by the Weather Research and Forecasting (WRF) model version 3.8 (Skamarock et al., 2008) and is specific to the model simulation period. Anthropogenic area and point emissions are based on the 2011 NEI version 2 platform "ek" (EPA, 2015a), with emissions for electrical generation units (EGU) updated using temporalized Continuous Emission Monitoring System (CEMS) data for 2013 (Farkas et al., 2015). Mobile emissions, from the Motor Vehicle Emission Simulator (MOVES) 2014a (EPA, 2015b), and biogenic emissions, from BEIS version 3.61, are driven by

day-specific meteorology for 2013. Initial and boundary conditions are extracted from a coarse 36 km CMAQ simulation that in turn is initialized using the GEOS-Chem global model version 8-3-2 (Henderson et al., 2014).

Our simulations are simplified compared to the original CMAQ simulations due to limitations in the CAMx model framework. For example, CMAQ computes biogenic and sea salt emissions inline in order to couple emissions more tightly to time-dependent processes such as meteorology (Foley et al., 2010), a capability that is not currently available for CAMx. Instead, we must calculate these emissions offline, which is expected to reduce precision and increase uncertainty relative to CMAQ. Biogenic emissions are processed via the Sparse Matrix Operator Kernel Emissions (SMOKE) (https://www.cmascenter.org/smoke/) modeling system version 4.5, and sea salt emissions are generated using CAMx support software. Both CAMx and CMAQ calculate plume rise and vertical emission injection from point sources inline; however, CMAQ differentiates between industrial emissions and wildland fires (Pouliot et al., 2005), whereas CAMx applies a single plume rise algorithm to all point source emissions (Emery et al., 2010). In order to utilize all available point source emissions, we estimate plume rise for wildland fires using industrial stack parameters, as described in Appendix C. Additionally, we omit simulation of windblown dust (Foroutan et al., 2017), lightning NO_x (Allen et al., 2012; Pickering et al., 1998), and bidirectional ammonia emissions (Pleim et al., 2013), all of which are calculated inline in CMAQ. Otherwise, our CAMx model setup is designed to mimic the baseline CMAQ simulation from Pye et al. (2018) as close as possible, without modifying source code. Uncertainty due to simplification of our CAMx simulations relative to CMAQ is addressed in Section 4.4.3.

Our CAMx simulations output average species concentrations at hourly intervals. We also utilize the model's Chemical Process Analysis (CPA) functionality to retrieve integrated reaction rates, as well as ozone indicator ratios and production regime assignments. For comparison to *in situ* observations, model output is extracted from the closest grid cell and hour to each of the filtered data points from SENEX, effectively synchronizing the model with the measurements in time and space.

4.2.4 Box model

We apply results from the box model simulations conducted by Marvin et al. (2017), which are generated using the Framework for 0-D Atmospheric Modeling version 3 (F0AMv3) (Wolfe et al., 2016b). These simulations are constrained to match observed mixing ratios of relevant species from SENEX, including: NO, NO_2, O_3, CO, isoprene, methane, methanol, and PAN. Mixing ratios are held fixed throughout each model run for all constrained species except NO, which is allowed to float after initialization to preserve the modeled NO/NO_2 ratio. Time and location of the aircraft are used to calculate solar zenith angle (SZA), which controls photolysis rates. The chemical system defined by each set of observations is integrated 72 hours forward in time, in one-hour time steps with time-varying SZA, to reach diel steady state. A minor term for physical loss is included to ensure that the atmospheric lifetime of any given species does not exceed 24 hr. Model output includes diel steady-state mixing ratios and instantaneous reaction rates for species corresponding to the implemented gas-phase chemical mechanism. Please refer to Marvin et al. (2017) for additional information regarding box model setup and simulation procedures.

In this study, we mainly use the box model output to constrain reaction rates to SENEX observations. Assuming that the MCMv3.3.1 gas-phase chemical mechanism achieves the best estimate of reaction rates related to isoprene chemistry (Jenkin et al., 2015; Marvin et al., 2017), we utilize the respective simulation from Marvin et al. (2017) to represent the actual atmosphere. The version implemented in this simulation is an isoprene-focused subset of the MCMv3.3.1 mechanism, which comprises 610 species and 1974 photochemical reactions. Constrained box model reaction rates are used to evaluate the reaction rates generated for CAMx and comprise the "inferred" rates mentioned throughout the text. Explanations are provided when box model simulations are applied for other purposes.

4.3 Gas-phase chemical mechanisms

This study utilizes results from three CAMx simulations, each of which implements a different variation of the Carbon Bond mechanism version 6 revision 2 (CB6r2) (Hildebrandt Ruiz and Yarwood, 2013). The CB6r2 mechanism is one of the most recent iterations of the CB mechanism, which was originally designed for implementation in large-scale air quality models. Version 6 and its four revisions feature an isoprene oxidation scheme that is generally considered up-to-date with the current scientific understanding. This scheme provides a detailed interpretation of first-generation isoprene oxidation chemistry, with explicit representation of $ISOPO_2$ and its NO_x-dependent reaction pathways. The reactions of $ISOPO_2$ with NO, HO_2, and RO_2 are all included, as is its isomerization, though only via 1,6-H shift. Subsequent chemistry is simplified, and certain oxidation products are lumped together for

computational efficiency. In our baseline simulation, we use CB6r2 with halogen chemistry, which is limited to 115 species and 304 reactions and comes standard with CAMx version 6.50 (Ramboll Environ, 2018).

Despite its detailed isoprene oxidation scheme, the CB6r2 mechanism underestimates important isoprene oxidation products such as HCHO. In our prior work (Marvin et al., 2017), we proposed a series of modifications to CB6r2 to improve HCHO production from isoprene oxidation in line with more recent and detailed mechanisms such as GEOS-Chem version 9-2+ (Fisher et al., 2016; Kim et al., 2015; Mao et al., 2013b; Marais et al., 2016; Travis et al., 2016) and MCMv3.3.1 (Jenkin et al., 2015). Specifically, modifications were targeted to improve HCHO production from isoprene oxidation products such as MVK and MACR in the late generations of isoprene oxidation, as described in Section 3.5 of this dissertation. Implementation of these modifications in a constrained 0-dimensional photochemical box model improved agreement with observations of HCHO from SENEX, increasing the NMB from −32% for CB6r2 to −14% for the modified mechanism, which we call CB6r2-UMD. The modifications are applied only to existing species and reactions, preserving the computational efficiency of CB6r2.

Translation of the CB6r2-UMD modifications to a regional model framework reveals additional shortcomings in CB6r2 that were masked by the box model constraints in Marvin et al. (2017), specifically regarding the photochemical production of PAN and its precursor CH_3CO_3. The CH_3CO_3 radical is produced by a wide variety of isoprene oxidation products near the end of the isoprene cascade; however, CB6r2 incorrectly attributes a large fraction of CH_3CO_3 production to the oxidation of glycolaldehyde ($HOCH_2CHO$). Instead, this reaction is expected to produce a different

PN radical ($HOCH_2CO_3$) that eventually decomposes to form HCHO (Jenkin et al., 2015; Paulot et al., 2009a), which is addressed in CB6r2-UMD by reassigning the major product of this reaction from CH_3CO_3 to HCHO. When PAN is constrained, as in the box model setup from Marvin et al. (2017), this change affects only the production of HCHO. Within the framework of the regional model, however, PAN is unconstrained, allowing the production of CH_3CO_3 to drop considerably. Because CH_3CO_3 is a precursor to both PAN and HCHO, we expect implementation of CB6r2-UMD 'as is' to reduce production of PAN and dampen effects on HCHO.

To improve the model representation of both PAN and HCHO, we propose one further modification to the isoprene oxidation scheme from CB6r2: we recommend increasing the production of CH_3CO_3 from the OH oxidation of MVK and MACR. This reaction is expected to be a major source of CH_3CO_3 (Lafranchi et al., 2009), but the product fraction used in CB6r2 (0.269) is underestimated due to simplification of its NO_x-dependency. Like isoprene, MVK and MACR oxidize to form unique RO_2 species whose fates are determined by NO_x conditions. However, CB6r2 does not represent these species or their reaction pathways explicitly, instead lumping MVK and MACR together and condensing their oxidation chemistry into a single reaction. In order to better account for this NO_x-dependency, we determine product fractions α_{MVK} and α_{MACR} for CH_3CO_3 from the oxidation MVK and MACR, respectively, using the following relationships adapted from LaFranchi et al. (2009):

$$\alpha_{\mathrm{MVK}} = 0.7 * \frac{k_{\mathrm{RO2+NO}}[\mathrm{NO}]}{k_{\mathrm{RO2+NO}}[\mathrm{NO}]+k_{\mathrm{RO2+HO2}}[\mathrm{HO2}]} \quad (4.1)$$

$$\alpha_{\mathrm{MACR}} = 0.1855 * \frac{k_{\mathrm{RO2+NO}}[\mathrm{NO}]}{k_{\mathrm{RO2+NO}}[\mathrm{NO}]+k_{\mathrm{RO2+HO2}}[\mathrm{HO2}]} \quad (4.2)$$

Based on the CB6r2-UMD box model simulation from Marvin et al. (2017), we calculate an average RO_2 reactivity ratio of 0.8147 ± 0.1166 (1σ) for SENEX. We substitute this value into Equations (4.1) and (4.2), and then we combine product fractions for lumped MVK and MACR assuming a 2:1 ratio of MVK to MACR:

$$\alpha_{\text{MVK+MACR}} = \frac{2}{3} * \alpha_{\text{MVK}} + \frac{1}{3} * \alpha_{\text{MACR}} \quad (4.3)$$

This procedure results in a product ratio $\alpha_{\text{MVK+MACR}}$ of 0.431 ± 0.0549 for the production of CH_3CO_3 from the OH oxidation of MVK and MACR, ~60% higher than the product fraction used in CB6r2.

Further steps are required to retain carbon balance in the reaction for the OH oxidation of MVK and MACR. For example, glycolaldehyde is co-produced with CH_3CO_3 in this reaction, so we increase its product fraction from 0.269 to match the value calculated for CH_3CO_3. Increased carbon from the manipulation of CH_3CO_3 and glycolaldehyde is then balanced by reducing, from 0.457 to 0.295, the yield of a lumped species called OPO_3. In CB6r2, OPO_3 represents PN radicals from unsaturated aldehydes; for this reaction, we understand it to represent the precursor to methacryloyl peroxynitrate (MPAN), produced via oxidation of MACR. According to LaFranchi et al. (2009), the product fraction for the production of MPAN from the oxidation of MACR should be 0.45; however, a 2:1 ratio of MVK to MACR implies a product fraction of 0.15 for the lumped species, only about one third of the product fraction used in CB6r2. Therefore, by exchanging production of OPO_3 for CH_3CO_3 and glycolaldehyde, we begin to approach literature recommendations for all three species. We combine these simple changes with the modifications from CB6r2-UMD to create

an updated version called CB6r2-UMD*, which preserves the computational efficiency of the original CB6r2 mechanism.

4.4 Analysis

Mixing ratios and reaction rates simulated with CAMx for ozone, NO_x, and certain VOCs – isoprene, HCHO, and PAN – are evaluated with respect to SENEX observations. Modeled versus measured mixing ratios (ppb) are compared across chemistry variations – CB6r2, CB6r2-UMD, and CB6r2-UMD* – for each of these species in Fig. 4.2. Linear least-squares regression analysis is performed for each simulation with respect to observations, and the normalized mean bias (NMB) is calculated as follows:

$$\mathrm{NMB} = \frac{\frac{1}{n}\sum_{i=1}^{n}(M_i - O_i)}{\frac{1}{n}\sum_{i=1}^{n} O_i} \times 100\% \quad (4.4)$$

where M is the modeled mixing ratio (ppb) and O is the observed mixing ratio (ppb) for each individual point i in a total of n data points (n = 2219). Results are described below, first for ozone precursor species VOCs and NO_x, and then for ozone. Additional analysis is provided to evaluate simulated PN distributions, as well as production rates for HCHO, HO_x, and ozone. Output is evaluated with respect to measurements where available, and otherwise with respect to inferred values from our "best estimate" box model simulation, which implements MCMv3.3.1 isoprene chemistry and is constrained to SENEX observations.

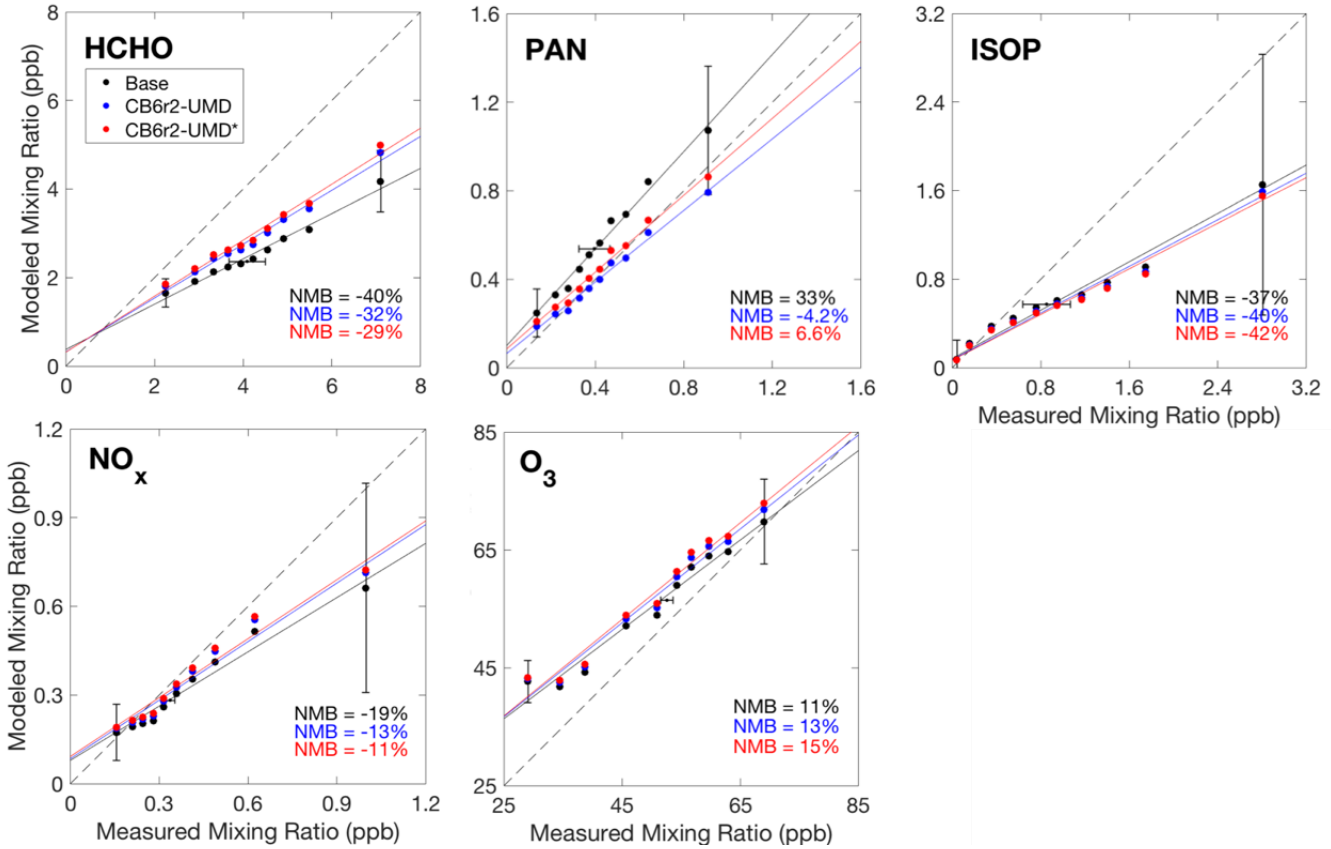

Fig. 4.2. Scatter of modeled versus measured mixing ratios (ppb) from SENEX. Each panel represents a different photochemical species important to ozone production and isoprene oxidation chemistry. Three CAMx simulations are incorporated into every panel, with each simulation represented by a unique color: baseline (black), CB6r2-UMD (blue) and CB6r2-UMD* (red). Datasets are binned for clarity, with each bin containing 222 points. A line of best fit, obtained by linear least-squares regression analysis, and the normalized mean bias are determined prior to the binning procedure, and are shown for each dataset in its respective color. The 1:1 line, shown here as a dashed black line, is provided for reference. The vertical error bars show 1σ variability in the first and last bins of the baseline simulation, while the horizontal error bars represent measurement uncertainty at median measured mixing ratios.

4.4.1 Ozone precursors

4.4.1.1 VOCs

The CAMx implementations of CB6r2-UMD and CB6r2-UMD* improve simulated mixing ratios of isoprene oxidation products HCHO and PAN relative to the standard CB6r2 mechanism, as shown in Fig. 4.2. With CB6r2-UMD and CB6r2-UMD* specifically designed to increase production of HCHO from isoprene oxidation, model-measurement agreement improves substantially, from −40% for the baseline case to −29% for CB6r2-UMD*. However, all representations of simulated HCHO exceed the measurement uncertainty, which is ±10%. Additionally, even the best model-measurement agreement of −29% is much lower than the −14% achieved by the constrained CB6r2-UMD box model simulation from Marvin et al. (2017). The majority of this difference is due to a persistent ~40% underestimation of simulated isoprene mixing ratios, though other potential contributions may include faster loss of HCHO to oxidation or photolysis, or even enhanced removal by physical processes such as mixing or deposition. Furthermore, mean simulated HCHO increases only 0.45 ppb (18%) between the baseline and CB6r2-UMD* CAMx simulations, which is dampened compared to an increase of 0.77 ppb (27%) achieved between the constrained CB6r2 and CB6r2-UMD box model simulations. Because the changes to the chemistry specifically target HCHO production from isoprene oxidation, underestimation of isoprene in the CAMx simulations is indicated as a major limiting factor to the accuracy of modeled HCHO mixing ratios.

The CPA tool for CAMx outputs reaction rates for first-generation HCHO production from isoprene oxidation and total HCHO production, which we compare

between simulations and evaluate with respect to inferred rates from SENEX observations. Fig. 4.3a illustrates this comparison and shows that the total HCHO production rate in CAMx approaches the inferred rate with each update to the isoprene chemistry. The total HCHO production rate increases from 1.55 ppb hr^{-1} for the baseline case to 1.92 ppb hr^{-1} for CB6r2-UMD*, which overestimates the inferred rate of 1.77 ppb hr^{-1} by 8%. Please note, however, that the total production rate from CAMx includes contributions from ~20 primary VOCs, whereas the inferred rate represents HCHO production from the oxidation of isoprene, methanol, and methane only, with isoprene accounting for ~80% of the total. Evaluation of the HCHO production rate from first-generation isoprene oxidation reveals that all simulated values (~0.3 ppb hr^{-1}) underestimate the inferred value (0.53 ppb hr^{-1}) by at least 40%. This suggests that HCHO production is limited by a deficit in isoprene oxidation.

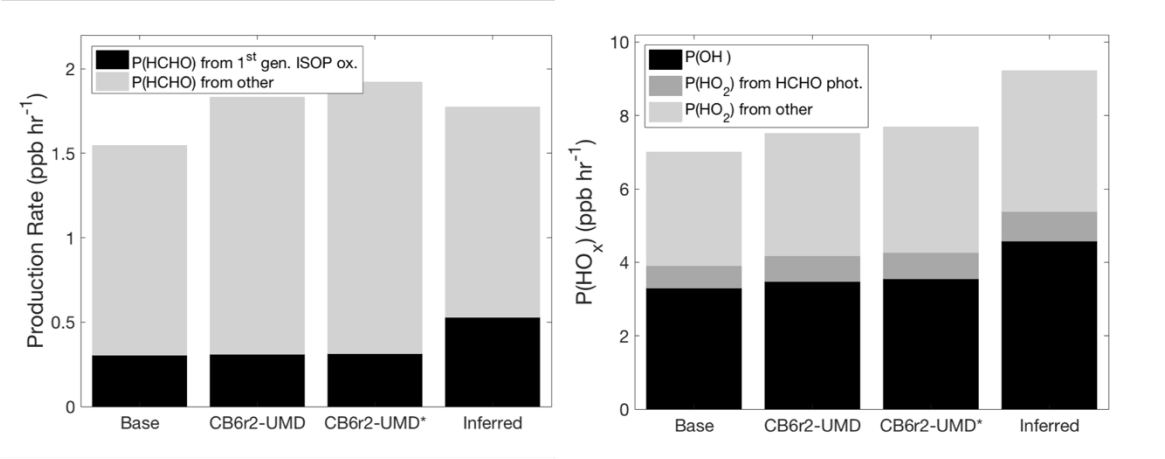

Fig. 4.3. Average production rates (ppb hr^{-1}) for a) HCHO and b) HO_x, simulated and inferred for SENEX. Production rates are stacked according to source reactions and simulated species (HO_x only), with the top of the stack equal to the total production rate. Note: first-generation production of HCHO from isoprene oxidation includes oxidation by OH, O_3, $O(^3P)$, and NO_3.

Evidently, substantial improvement in the simulation of isoprene itself is needed in order to bring simulated oxidation products such as HCHO into better agreement with SENEX observations.

Though also a product of isoprene oxidation, PAN is well-simulated by both CB6r2-UMD and CB6r2-UMD*. As shown in Fig. 4.2, the representation of PAN in the baseline simulation leads to a 33% overestimation of simulated mixing ratios. Implementation of the CB6r2-UMD and CB6r2-UMD* mechanisms brings model-measurement agreement within 10%. Although CB6r2-UMD* is designed specifically to improve PAN relative to CB6r2-UMD, agreement is slightly worse for CB6r2-UMD* (NMB = 6.6%) than for CB6r2-UMD (−4.2%); however, both are within the measurement uncertainty, which is ±(15% + 10 ppt). Such a high quality of model-measurement agreement, despite the stated challenges with simulated isoprene, is indicative of an overestimation in simulated production of PAN from the oxidation of isoprene and perhaps other primary VOCs.

The CB6r2-UMD and CB6r2-UMD* mechanisms also improve the simulated distribution of total PNs compared to measurements, as shown in Fig. 4.4. For this comparison, measurements are speciated according to the CB formulation, where PANX represents the sum of the three-carbon PNs peroxy proprionyl nitrate (PPN) with peroxy acryloyl nitrate (APAN), while OPAN represents the four-carbon PN peroxy methacryloyl nitrate (MPAN). Direct measurements are provided for PPN and APAN, whereas MPAN is inferred based on its expected ratio to PAN, 0.075 at 23 °C, as recommended by LaFranchi et al. (2009). Mixing ratios for PPN, inferred by the same procedure and using the same recommended ratio, match measured values

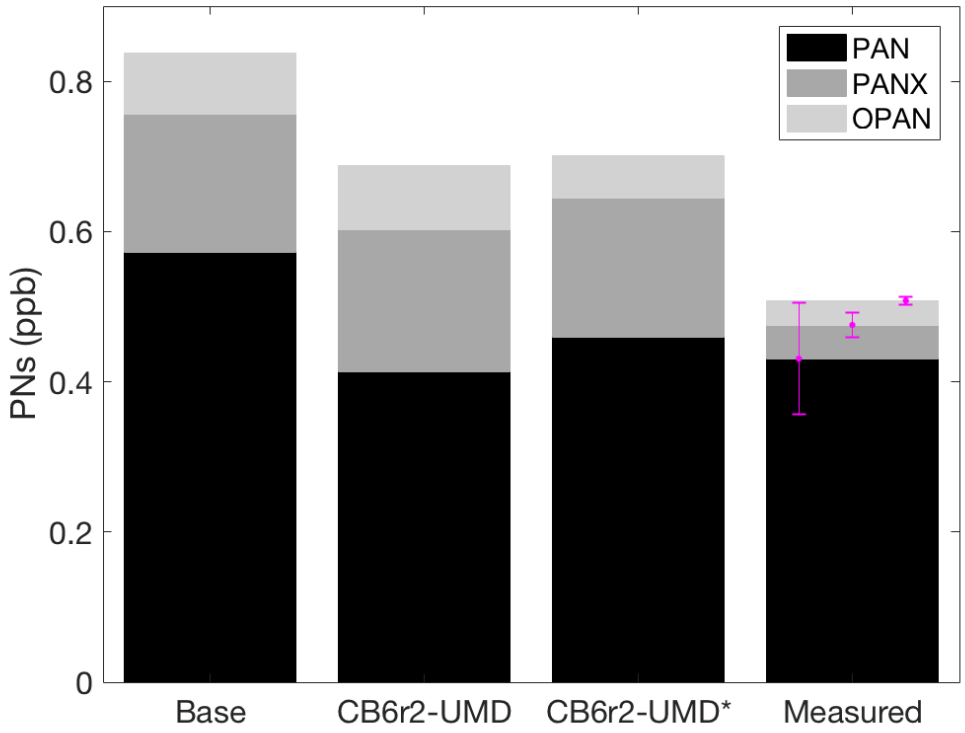

Fig. 4.4. Average mixing ratios (ppb) of PNs, simulated for and measured during SENEX. Simulated and measured mixing ratios are speciated and stacked according to the CB formulation, where PANX represents the sum of the three-carbon PNs peroxy proprionyl nitrate (PPN) with peroxy acryloyl nitrate (APAN), while OPAN represents the four-carbon PN peroxy methacryloyl nitrate (MPAN). Direct measurements are provided for PPN and APAN, whereas MPAN is inferred based on a ratio of 0.075 to PAN. The top of the stack represents total PNs. Error bars indicate measurement uncertainty.

within 3%. Fig. 4.4 shows that both CB6r2-UMD and CB6r2-UMD* correct a gross overestimation of PAN during SENEX. The average mixing ratio is reduced from 0.57 ppb in the baseline simulation to 0.41 ppb and 0.46 ppb for CB6r2-UMD and CB6r2-UMD*, respectively, which converge on the average measured mixing ratio (0.43 ppb). Only CB6r2-UMD*, however, also improves the average simulated mixing ratio of OPAN, which is reduced from 0.082 ppb in the baseline simulation to 0.056 ppb, approaching the inferred mixing ratio of 0.03 ppb. Although CB6r2-UMD* brings simulated PAN mixing ratios within the measurement uncertainty, MPAN is still

overestimated by 73% and PPN by more than a factor of 3. As NO_x reservoirs, PNs are important to the production of tropospheric ozone, and their overestimation may cause regional models to underestimate ozone production where these reservoirs form and to overestimate ozone production where they decompose.

As shown in Fig. 4.2, isoprene itself is underestimated by ~40% in all three CAMx simulations compared to observations, which cannot be explained by a measurement uncertainty of ±25%. Increased production of HCHO in CB6r2-UMD and CB6r2-UMD* increases production of HO_2 from 0.61 ppb hr^{-1} in the baseline case to 0.72 ppb hr^{-1} (18%) in CB6r2-UMD*, as demonstrated in Fig. 4.3b. Radical cycling distributes this enhancement among both HO_x species, increasing the production of OH up to 0.25 ppb hr^{-1} (8%). Enhanced OH increases the reactivity of atmospheric VOCs, effectively increasing photochemical loss and reducing ambient mixing ratios. This is especially apparent for primary VOCs such as isoprene, which are not replenished by photochemical production. Reduction in isoprene mixing ratios leads to poorer model-measurement agreement in CB6r2-UMD (−40%) and CB6r2-UMD* (−42%), compared to the baseline case (−37%). In Section 4.5.1, we consider strategies for improving simulated isoprene, which we expect also to impact the simulation of its oxidation products, including HCHO, PAN, and ozone.

4.4.1.2 NO_x

Simulated NO_x is also underestimated in all three CAMx simulations compared to observations, as shown in Fig. 4.2. At best, CAMx underestimates NO_x by 11%, which remains outside the combined measurement uncertainty for NO and NO_2 (±5%). However, model-measurement agreement for NO_x improves with each adjustment to the isoprene chemistry. As described in Section 4.3, the CB6r2-UMD mechanism substantially decreases production of the PAN precursor CH_3CO_3 relative to the baseline mechanism, which reduces the amount of CH_3CO_3 available to react with NO_2. Reduced loss by PAN uptake allows more NO_2 to exist in its radical form, cycling with NO as NO_x. The response of simulated NO_x to the modifications incorporated into CB6r2-UMD* is less obvious, as uptake of NO_2 by OPAN precursor OPO_3 is simply replaced by CH_3CO_3 uptake. However, residual differences between the formation and thermal decomposition rates for PAN and OPAN may affect NO_2 partitioning. The CB6r2 mechanism assumes that the same formation and degradation rates apply to all PN species, but the CB6r2-UMD and CB6r2-UMD* mechanisms update these rates only for PAN. Therefore, the rates for PAN reflect the 2014 Kinetic Data Evaluation of the International Union of Pure and Applied Chemistry (IUPAC), while the rates for PANX and OPAN reflect a prior assessment (Atkinson et al., 2006). Assuming a temperature of 298 K and atmospheric density of 2.5×10^{19} molecules cm^{-3}, the formation rate of PAN in the UMD variants is slower than that of OPAN (8.97 versus 9.40×10^{-12} molecules cm^{-3} s^{-1}), and its degradation rate is faster (4.31 versus 2.99×10^{-4} molecules cm^{-3} s^{-1}), allowing more NO_2 to exist in the radical state. Further reduction in the production of PN species such as PANX and OPAN, and continued

refinement of their formation and decomposition rates, is expected to increase simulated NO_2 and thus continue to improve model-measurement agreement.

Although NO_x is underestimated in CAMx, NO_y ($NO_y = NO_x + PNs + HNO_3 +$ organic nitrates) is overestimated compared to observations, which were measured simultaneously with ozone and NO_x during SENEX via CL detection (Ryerson et al., 2000, 1999, 1998). Fig. 4.5 demonstrates that NO_y is overestimated in the baseline CAMx simulation by 23%, which exceeds the reported measurement uncertainty of ±12%. Also shown is HNO_3, a major component of NO_y (35% on average during SENEX), which was measured via CIMS (Neuman et al., 2003, 2002). Modeled HNO_3 is overestimated in CAMx by 5%, though this discrepancy is within the reported measurement uncertainty of ±(20% + 50 ppt). By subtracting the contributions of the measured components, we can infer that the mean mixing ratio of organic nitrates (not measured) during SENEX is 0.48 ppb, or ~25% of total NO_y. The mean mixing ratio from the baseline CAMx simulation is 0.66 ppb, which overestimates the inferred value by 38%. Because our chemical modifications mainly affect NO_y partitioning between NO_x and PAN, we expect similar results for NO_y, HNO_3, and organic nitrates from the two chemical sensitivity simulations. Further investigation into the CB6r2 chemical mechanism and its variants is required to meaningfully improve NO_y partitioning relative to observations. However, we do expect partitioning-based corrections to increase simulated NO_x. Overestimation of NO_y in CAMx is indicative of excess nitrogen in the troposphere, which – if partitioned properly – may ultimately lead to overestimation of NO_x and therefore also ozone production. We discuss strategies for improving simulated NO_x in Section 4.5.2.

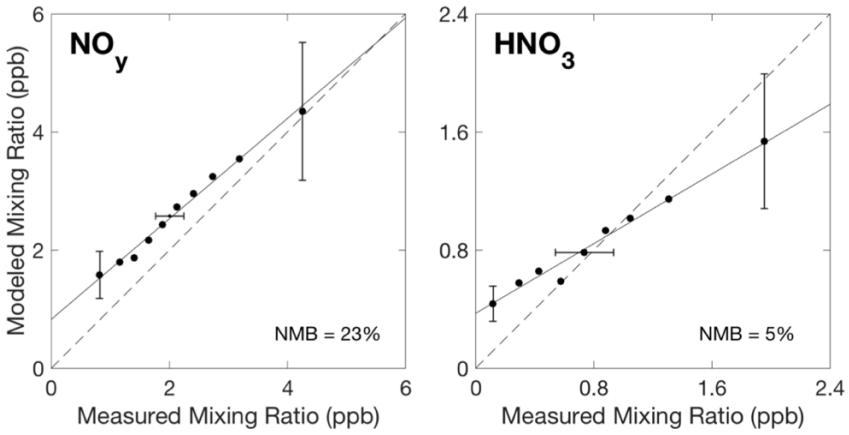

Fig. 4.5. Scatter of modeled versus measured mixing ratios (ppb) for NO_y and HNO_3 from SENEX. Modeled mixing ratios are shown for the baseline CAMx simulation only. A line of best fit, obtained by linear least-squares regression analysis, and the normalized mean bias are shown for each dataset. The 1:1 line, shown here as a dashed black line, is provided for reference. Vertical error bars represent variability in the first and last bins, while the horizontal error bars represent measurement uncertainty.

4.4.2 Ozone and ozone production diagnostics

Despite model underestimation of important ozone precursors isoprene and NO_x, simulated ozone mixing ratios are consistently overestimated in CAMx compared to observations. As shown in Fig. 4.2, all three CAMx simulations overestimate ozone along the SENEX flight track by more than 10%, which exceeds the measurement uncertainty of ±2%. Simulated ozone production is limited by the rates of reaction of NO with HO_2 and RO_2:

$$P(O_3) = k_{HO2+NO}[HO_2][NO] + \sum k_{RO2i+NO}[RO_{2i}][NO] \quad (4.5)$$

where $P(O_3)$ is the ozone production rate (molecules cm^{-3} s^{-1}), k_{HO2+NO} and $k_{RO2i+NO}$ are reaction rate constants (cm^3 $molecule^{-1}$ s^{-1}), and $[HO_2]$, $[RO_{2i}]$, and [NO] are species concentrations (molecules cm^{-3}). The subscript *i* denotes the separation of RO_2 into individual species for calculation of the second term. Increased production of HCHO, and thus HO_2, with the implementation of CB6r2-UMD and CB6r2-UMD*

increases ozone production rates (Fig. 4.6) and mixing ratios (Fig. 4.2), which worsens overestimation of the SENEX observations (13% and 15%, respectively), relative to the baseline simulation (11%). Such overestimation of ozone mixing ratios could lead to model prediction of false positive ozone exceedances and therefore potentially also the misallocation of valuable ozone management resources.

Although ozone mixing ratios are overestimated in CAMx, net ozone production is underestimated by all three simulations compared to inferred rates from SENEX observations. In CAMx, net ozone production is computed through the summation of all reaction rates directly involved in the photochemical production and loss of ozone, where loss is represented by a negative rate. The presentation of net ozone production rates (ppb hr^{-1}) as a function of NO (ppb) in Fig. 4.6 highlights a

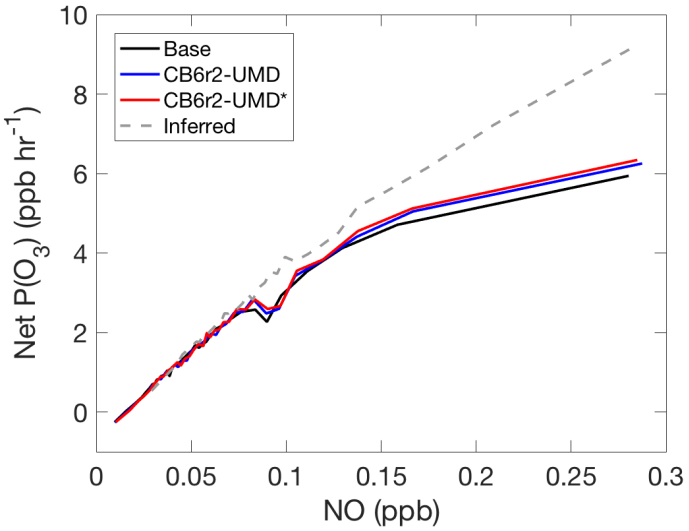

Fig. 4.6. Net photochemical ozone production (ppb hr^{-1}) as a function of NO (ppb), simulated and inferred for SENEX. Three CAMx simulations are incorporated, with each simulation represented by a unique color: baseline (black), CB6r2-UMD (blue) and CB6r2-UMD* (red). Inferred rates are represented by the dashed gray line. Calculated rates are binned by NO, with each bin containing 60 points. Lines represent bin averages.

deviation in the simulated rates from the inferred rates, which reaches a maximum of 3.3 ppb hr^{-1} (36%) at high mixing ratios of NO. Underestimation in some of the elements of the photochemical production of ozone is supported by a recent study by Hembeck et al. (2019). Their study found that ozone precursor radicals HO_2 and RO_2 are underestimated by 35 ± 19% in a simulation of the CMAQ regional model – with BEISv3.61 emissions and a variant on CB05 chemistry – compared to inferred values from the Maryland phase of the 2011 DISCOVER-AQ aircraft campaign. An underestimation of the HO_2 and RO_2 radicals implies persistent deficiencies in VOC emissions or oxidation that continue to limit the production of surface ozone.

Underestimation of net ozone production thus also indicates that the overestimation of ozone mixing ratios is not photochemical in nature. Instead, the enhancement of ozone mixing ratios in regionally-simulated ozone mixing ratios may be attributable to physical factors, perhaps underestimated ozone deposition or excessive vertical mixing, the latter of which was recently hypothesized by Travis et al. (2016). The vertical profile of ozone is generally expected to increase with altitude; however, the average vertical profile modeled for SENEX overestimates observed ozone mixing ratios near the surface and underestimates them aloft (Fig. 4.7). Contrarily, the vertical profile of carbon monoxide (CO), a conserved tracer for surface emissions, is generally expected to decrease with altitude; however, the average vertical profile modeled for SENEX underestimates observed CO mixing ratios near the surface and overestimates them aloft. The behavior demonstrated by the simulated vertical profiles of both ozone and CO, relative to observations from SENEX, thus indicates that excessive vertical mixing indeed contributes to the overestimation of ozone mixing ratios in our CAMx simulations. Further investigation is encouraged to quantify the

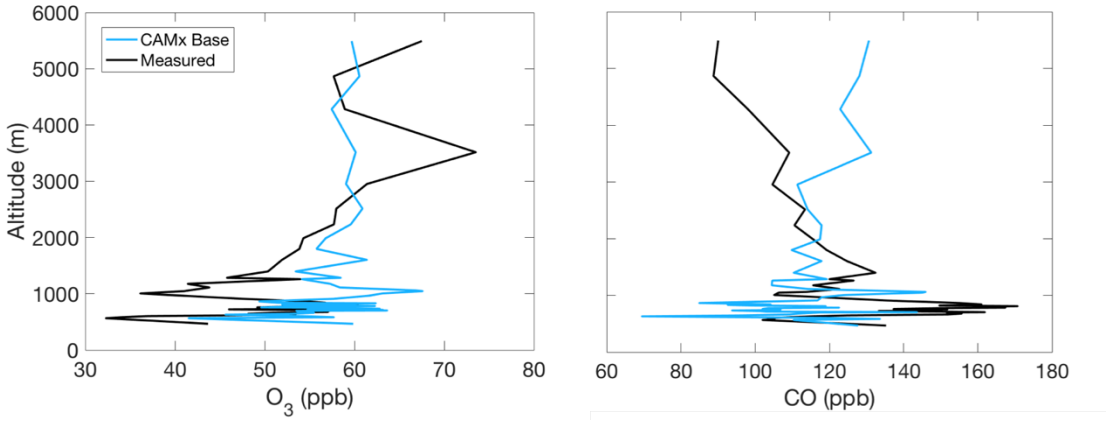

Fig. 4.7. Average vertical profiles for ozone (left) and CO (right) mixing ratios (ppb), as modeled and measured for SENEX. Model output and observations are filtered as normal, except for the boundary layer restrictions (altitude < 1500 m). Mixing ratios are binned by altitude (m), with each bin containing 60 points. Lines represent bin averages.

impact of vertical mixing on the simulation of ozone and its precursors and to determine appropriate strategies for correction.

The CAMx model characterizes ozone production regimes as either NO_x-limited or VOC-limited using the ratio of the hydrogen peroxide (H_2O_2) production rate to the nitric acid (HNO_3) production rate, derived from Sillman et al. (1995). A larger ratio indicates that radical termination is dominated by the self-reaction of HO_2, while a smaller ratio indicates that radical termination involves the uptake of NO_x. Regime characterization diverges at a ratio of 0.35, above which ozone production is NO_x-limited, and below which ozone production is VOC-limited. An overwhelming majority (~95%) of the simulated data points for SENEX are identified as NO_x-limited, as demonstrated in Fig. 4.8, which presents the difference in net ozone production rates (ppb hr^{-1}) between the CB6r2-UMD* simulation and the baseline case as a function of NO (ppb). Transition between regimes is extremely rare for this dataset, occurring only twice (overlapping), and shifting from VOC-limited to NO_x-limited. Because ozone

production is largely NO_x-limited for SENEX, we anticipate that any additional corrections to ozone precursors such as isoprene or NO_x will continue to increase ozone mixing ratios and thus degrade model-measurement agreement even further.

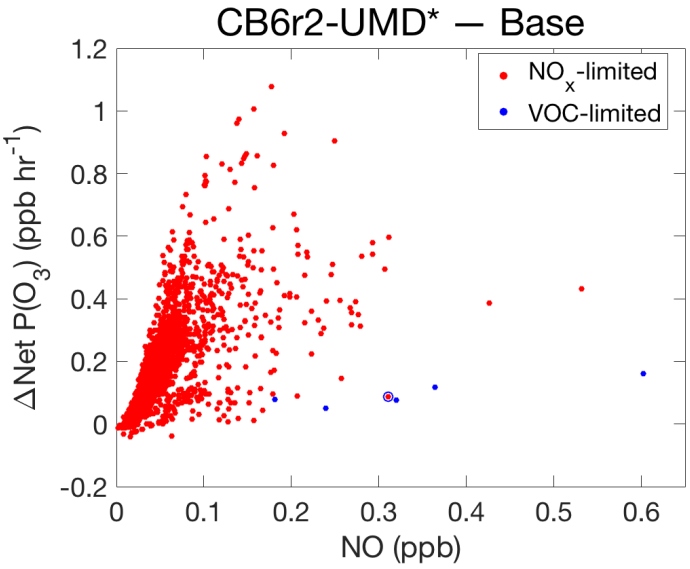

Fig. 4.8. The difference in net ozone production rates (ppb hr^{-1}), simulated for SENEX using the CB6r2-UMD* and baseline CAMx simulations, as a function of NO (ppb). Data points are colored by ozone production regime, identified as NO_x-limited (red) where $P(H_2O_2)/P(HNO_3) > 0.35$ and VOC-limited (blue) where $P(H_2O_2)/P(HNO_3) < 0.35$. Two overlapping transition points, that shift from VOC-limited to NO_x-limited between simulations, are plotted in red and encircled with blue.

4.4.3 Uncertainties

Thus far, we have shown that the modifications to the isoprene chemistry in CB6r2-UMD and CB6r2-UMD* improve model-measurement agreement for most considered species compared to the baseline CAMx simulation, but we have also shown that modeled mixing ratios continue to remain outside of the measurement uncertainty for all considered species except PAN. On top of their reported accuracy of ±10%, the measurements of HCHO obtained by the ISAF instrument are also potentially subject to additional interference from ISOPOOH (St. Clair et al., 2016). However, Marvin et al. (2017) showed that for SENEX, this interference inflates measured HCHO mixing ratios by at most 1% on average, and a systematic 11% downward-revision in measured HCHO mixing ratios is still not enough to achieve agreement with modeled HCHO mixing ratios from any of our three CAMx simulations.

In addition to the reported measurement uncertainties, simultaneous measurements of key species among multiple instruments from the SENEX payload provide an opportunity for exploring uncertainties relating to inter-instrument variability. As mentioned in Section 4.2.1, our analysis applies observations of isoprene measured via PTR-MS, with NO_x and ozone measured via CL detection. However, additional reliable measurements are available for isoprene via iWAS/GC-MS, for ozone via CRDS, and for NO_2 via both CRDS and ACES. For our dataset, isoprene mixing ratios measured via iWAS/GC-MS are 7% less than those measured via PTR-MS. Substituting iWAS measurements for PTR-MS improves model-measurement agreement for isoprene from −37% to −34% for the baseline CAMx simulation; however, the remaining difference cannot be explained by measurement uncertainty, at most ±20%. We also find that CRDS ozone is 2% lower than CL ozone, and that CRDS

NO_2 is 1% higher than CL NO_2, resulting in worse model-measurement agreement for both species. Thus, despite their differences, these alternate measurements of isoprene, ozone, and NO_2 generally support the same trends emphasized by our analysis. The ACES measurements of NO_2, on the other hand, are 20% lower than those obtained via CL detection, which would improve NO_x model-measurement agreement to −2.3%, 5.2%, and 7.9% for the baseline, CB6r2-UMD, and CB6r2-UMD* simulations, respectively. Although these values differ significantly from those obtained using CL NO_2, they are within or near the combined measurement uncertainty of ±6%. Use of ACES NO_2 for model-measurement comparison thus implies worse agreement for NO_x with each modification of the CB6r2 mechanism, contrary to our analysis with the CL measurements. Opposite signs and trends in agreement require different solutions for improving simulated NO_x in CAMx.

Comparison of simulated mixing ratios between CAMx and CMAQ allows us also to assess inter-model variability. In Fig. 4.9, we compare simulated to measured mixing ratios (ppb) of HCHO, NO_2, and ozone (with NO_2 and ozone represented using CL measurements). The figure shows model results for both our baseline CAMx simulation and a CMAQ simulation based on Pye et al. (2018, 2015). The CMAQ simulation shown here differs from that published by Pye et al. only through our omission of lightning NO_x; however, we do not expect lightning NO_x to significantly affect simulated mixing ratios for times and locations coincident with SENEX. Fig. 4.9 shows that, despite its simplification relative to CMAQ as described in Section 4.2.3, the CAMx baseline simulation achieves a better normalized mean bias for the ozone precursors HCHO (−40% versus −44%) and NO_2 (−21% versus −35%). Due to the prevailing NO_x-limited conditions for ozone production during SENEX, less NO_2 in

CMAQ results in less ozone production and thus lower simulated ozone mixing ratios. Consequently, ozone from the CMAQ simulation achieves model-measurement agreement of 2.7%, nearly within the measurement uncertainty of ±2%. However, as well as the ozone mixing ratios from CMAQ may match the observations from SENEX, accuracy in the simulation of ozone precursors is critical to maintaining accuracy in the simulation of ozone under all conditions.

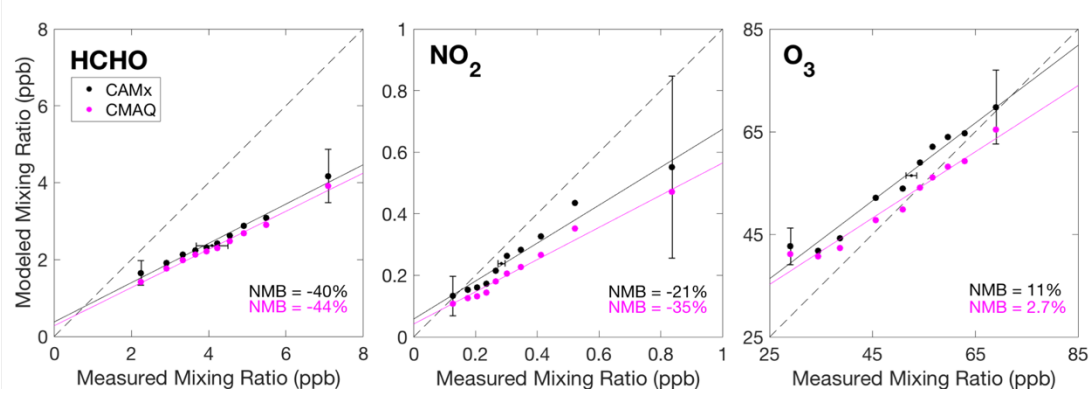

Fig. 4.9. Scatter of modeled versus measured mixing ratios (ppb) from SENEX. Each panel represents a different photochemical species important to ozone production and isoprene oxidation chemistry. Two model simulations are incorporated into every panel, with each simulation represented by a unique color: CAMx baseline (black) and CMAQ baseline (magenta). Datasets are binned for clarity, with each bin containing 222 points. A line of best fit, obtained by linear least-squares regression analysis, and the normalized mean bias are determined prior to the binning procedure, and are shown for each dataset in its respective color. The 1:1 line, shown here as a dashed black line, is provided for reference. The vertical error bars show 1σ variability in the first and last bins of the baseline simulation, while the horizontal error bars represent measurement uncertainty at median measured mixing ratios.

4.5 Implications

4.5.1 Isoprene emissions

Our analysis has important implications for the isoprene emissions that drive our regional modeling platform. As described in Section 4.4.1.1, model evaluation by comparison to SENEX observations reveals that each of our CAMx simulations underestimates observed isoprene mixing ratios and inferred rates for first-generation HCHO production from isoprene oxidation by ~40%, which must be attributed to underestimated isoprene emissions, overestimated photochemical loss, or excessive physical transport. Loss of isoprene is dominated by its oxidation with OH, which is described by a rate constant that is known within ±15% at 296 K (Atkinson et al., 2006), the mean temperature observed during SENEX. In Section 4.4.1.1, we also showed that the simulated production of OH is underestimated by >22% in CAMx compared to the inferred production from SENEX, which implies that the loss of isoprene to photochemical oxidation is underestimated in our simulations, despite a potential offset by uncertainty in the rate constant. This suggests that isoprene is likely impacted by excessive transport by dispersion or vertical mixing, underestimated emissions from BEIS v3.61 (Fig. 4.10), or a combination of both.

To the best of our knowledge, very few studies have evaluated the isoprene emissions from BEISv3.61 prior to this work. However, one study by Goldberg et al. (2016), includes a comparison of modeled isoprene, simulated using CAMx version 6.10 with BEISv3.61 emissions, to aircraft observations of isoprene from the

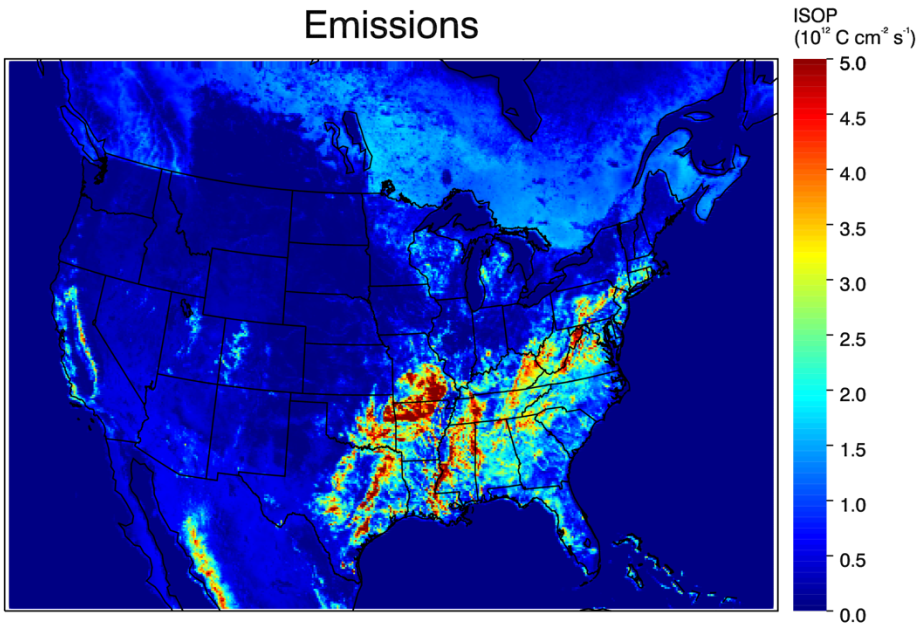

Fig. 4.10. Isoprene area emissions (10^{12} C cm^{-2} s^{-1}) generated using BEIS version 3.61 for the baseline CAMx simulation (i.e., unadjusted), averaged for the hours of 8–20 EDT across all days in the simulation period. Note that the color bar saturates at 5×10^{12} C cm^{-2} s^{-1}.

Maryland phase of the DISCOVER-AQ campaign. The modeled isoprene from the Goldberg et al. comparison achieves an NMB of 2.92%, much closer to observations than the modeled isoprene from this work. However, the simulation from the Goldberg et al. comparison applies the Carbon Bond 2005 (CB05) gas-phase chemical mechanism, an outdated predecessor to CB6r2. Marvin et al. (2017) showed that, for SENEX conditions, CB6r2 results in ~20% more OH on average relative to CB05 (Fig. 3.2), which could lower modeled isoprene by nearly the same fraction. Differences in model output post-processing procedures applied in this work and in Goldberg et al. account for another 10% difference in modeled isoprene. The remaining 10% deviation from observations may be explained by the difference in vertical mixing schemes applied in the two modeling scenarios: we apply the Asymmetric Convective Model version 2 (ACM2) scheme (Pleim, 2007), whereas Goldberg et al. applies the default

K-theory scheme provided in CAMx, which is expected to reduce vertical mixing compared to ACM2 (Goldberg, 2015). Despite the potential contribution from vertical mixing, therefore, our results maintain that isoprene emissions from BEISv3.61 are underestimated by 30−40%, and that this bias may impact a variety of modeling scenarios.

To correct for underestimated isoprene emissions, we conduct one more sensitivity simulation that applies our best isoprene oxidation mechanism CB6r2-UMD* and additionally increases isoprene emissions from BEISv3.61 by 40%. We refer to this simulation as 'ISOP-UMD', because it aims to improve multiple aspects in the regional simulation of isoprene. Implementation of ISOP-UMD significantly improves simulated mixing ratios for isoprene and HCHO compared to SENEX observations. These results are illustrated in Fig. 4.11, which compares modeled versus measured mixing ratios (ppb) for isoprene, HCHO, and other relevant species between the baseline and ISOP-UMD CAMx simulations. As shown in this figure, the ISOP-UMD simulation improves modeled mixing ratios of isoprene to match observations within 1%. Additionally, mixing ratios of HCHO match observations within 16%, which approaches the model-measurement agreement achieved by the MCMv3.3.1 (NMB=−15%) and CB6r2-UMD (−14%) chemical mechanisms in the constrained box model simulations of Marvin et al. (2017). Increased isoprene emissions in ISOP-UMD also increase the total HCHO production rate and bring total production of HO_x closer to the inferred rate from SENEX (Fig. 4.12). Modeled PAN improves in ISOP-UMD compared to the baseline simulation but worsens relative to both chemistry-focused simulations; however, agreement of 15% is still within measurement uncertainties.

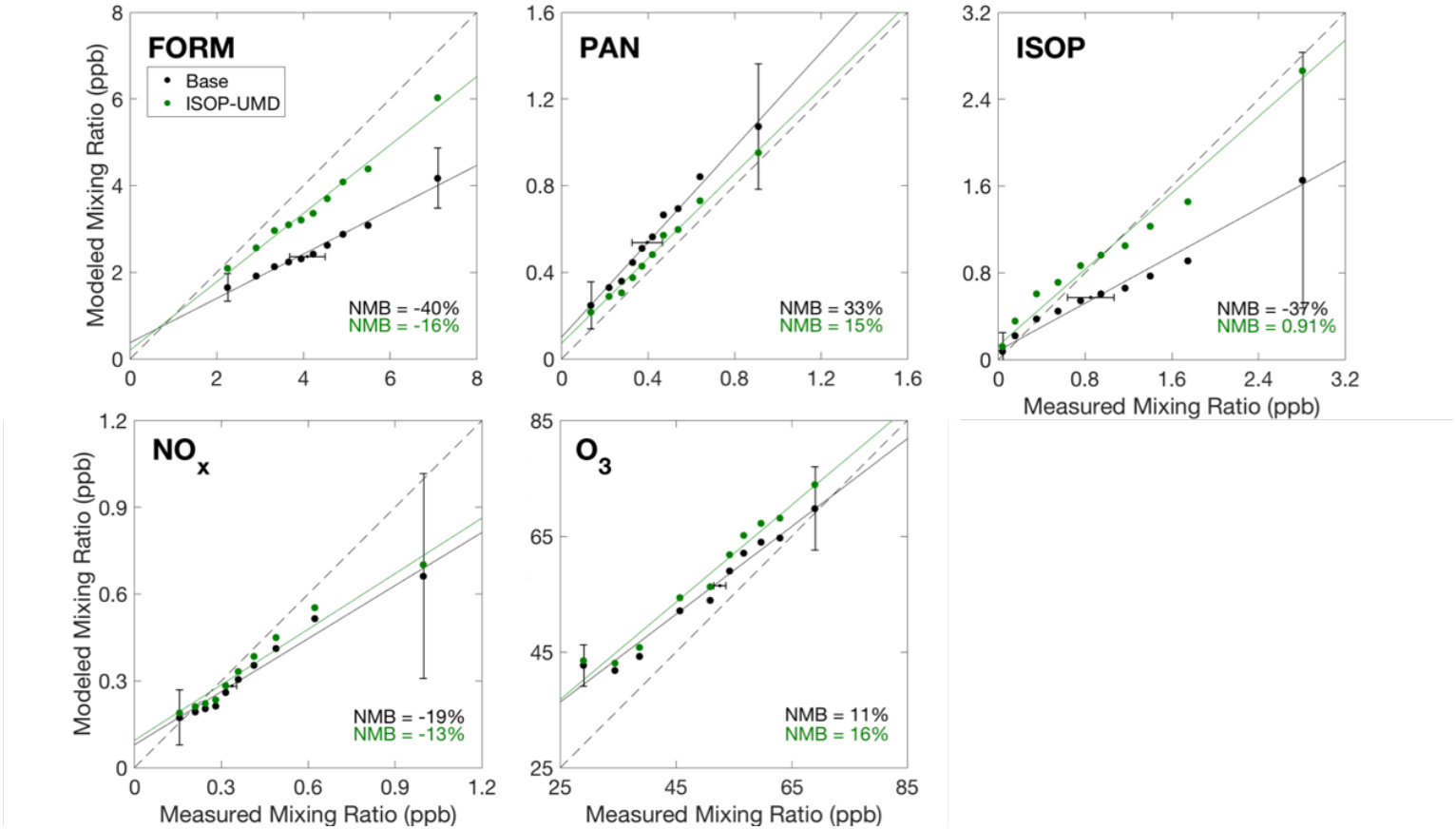

Fig. 4.11. Scatter of modeled versus measured mixing ratios (ppb) from SENEX. Each panel represents a different photochemical species important to ozone production and isoprene oxidation chemistry. Two model simulations are incorporated into every panel, with each simulation represented by a unique color: CAMx baseline (black) and CMAQ baseline (magenta). Datasets are binned for clarity, with each bin containing 222 points. A line of best fit, obtained by linear least-squares regression analysis, and the normalized mean bias are determined prior to the binning procedure, and are shown for each dataset in its respective color. The 1:1 line, shown here as a dashed black line, is provided for reference. The vertical error bars show 1σ variability in the first and last bins of the baseline simulation, while the horizontal error bars represent measurement uncertainty at median measured mixing ratios.

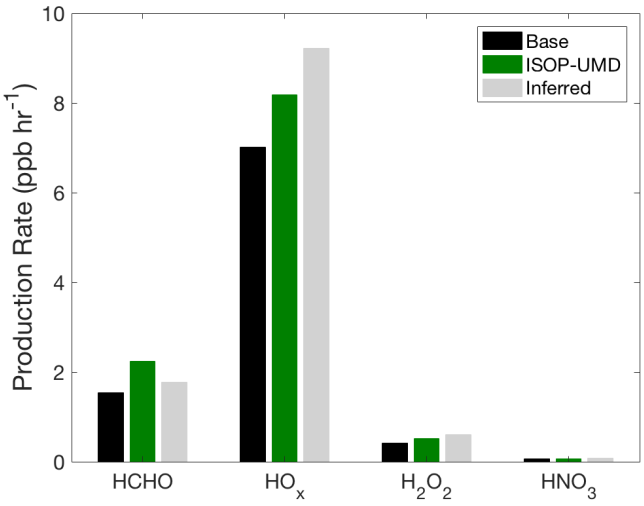

Fig. 4.12. Production rates (ppb hr^{-1}) for HCHO, HO_2, H_2O_2, and HNO_3, simulated and inferred (gray) for SENEX. Simulated values are provided for the baseline CAMx simulation (black), as well as for ISOP-UMD (green).

Enhancement of isoprene mixing ratios in ISOP-UMD increases RO_2 and therefore also its uptake of NO_x, resulting in decreased NO_x mixing ratios compared to implementation of the CB6r2-UMD* chemistry only; however, agreement is still better than that achieved for the baseline CAMx simulation. Finally, model-measurement agreement for ozone worsens with ISOP-UMD compared to the three other CAMx simulations; however, because ozone production is predominantly NO_x-limited along the SENEX flight tracks, such a substantial increase in VOCs has a relatively minor effect on simulated ozone mixing ratios. Although agreement worsens for ozone, we value the improvements achieved by ISOP-UMD in the simulation of ozone precursors, which are more instructive to the development of effective ozone management strategies, as will be discussed in Section 4.5.3.

4.5.2 NO_x emissions

Implications for NO_x emissions, as implemented in our regional modeling platform, are not as clear as they are for isoprene. Each of our simulations applies area and point emissions based on the 2011 NEI version 2 platform "ek" (EPA, 2015a), with EGU emissions updated to reflect temporalized CEMS data for 2013 (Farkas et al., 2015) and mobile emissions developed specifically for the simulation period using the MOVES model version 2014a (EPA, 2015b). Our evaluation of modeled NO_x by comparison to SENEX measurements returns conflicting results, depending on which measurements are used. Comparison to the CL measurements indicates that NO_x is underestimated in CAMx, whereas the comparison using ACES NO_2 suggests that NO_x is overestimated in CAMx. In either case, modeled NO_y is grossly overestimated, which indicates an excess of nitrogen in the troposphere. Such an excess may be attributed to overestimated emissions of NO_x, underestimated physiochemical loss of NO_y, or some combination of each. However, effects of NO_y partitioning on simulated NO_x remain unclear as long as the CL and ACES measurements disagree.

Recent studies have suggested that industrial and mobile emissions of NO_x from the NEI are biased high by 50−60% (Anderson et al., 2014; Canty et al., 2015; Travis et al., 2016). Based on our analysis, we would expect a corrective reduction in NO_x emissions to improve simulated NO_x relative to the ACES measurements, but to worsen simulated NO_x relative to the CL measurements. However, spatial analysis reveals that modeled NO_x, though biased low compared to CL measurements on average, is biased high relative to the same measurements by up to 0.5 ppb near cities and power plants, as shown in Fig. 4.13. These results may support the recommendations of Anderson et al. (2014), Canty et al. (2015), and Travis et al. (2016); but, if the model truly

underestimates observed NO_x, as suggested by the CL measurements, NO_x emissions reductions must be coupled with improvements in NO_y partitioning to ensure that model-measurement agreement does not degenerate as a result. We therefore encourage further evaluation of the NO_x measurements and their contributions to total NO_y as a first priority, in order to build a reliable groundwork for assessing NO_x emissions in the future.

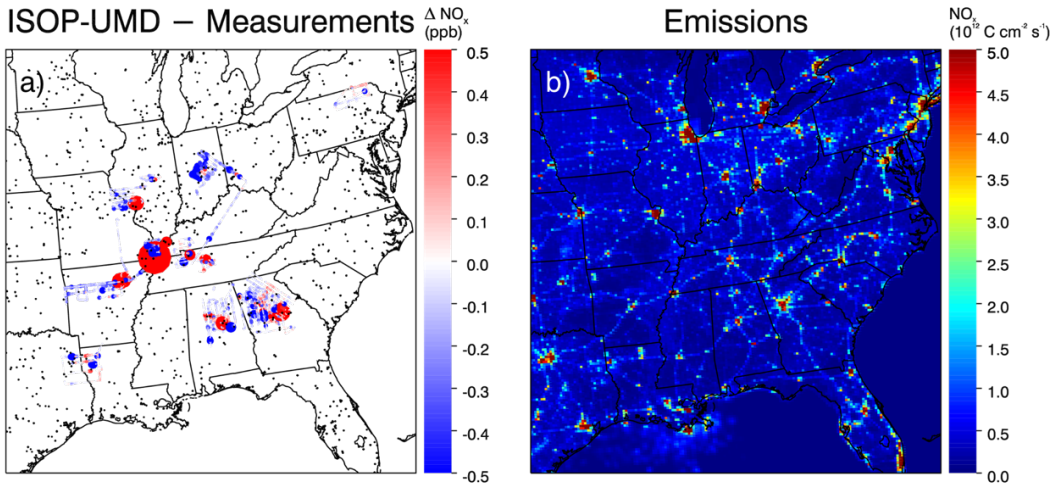

Fig. 4.13. a) Difference between modeled and measured NO_x mixing ratios (ppb) for SENEX, where modeled mixing ratios are obtained from the ISOP-UMD simulation and measurements are obtained by CL detection. Dynamic sizing is applied to emphasize absolute differences. Black dots indicate EGU locations. Note that the color bar saturates at −0.5 and 0.5 ppb. b) NO_x area emissions (10^{12} C cm^{-2} s^{-1}) based on the 2011 NEI version 2 platform "ek," with day-specific mobile emissions developed using MOVES 2014a, averaged for the hours of 8–20 EDT across all days in the simulation period. Note that the color bar saturates at 5×10^{12} C cm^{-2} s^{-1}.

4.5.3 Surface ozone management strategies

Here we apply our best isoprene mechanism CB6r2-UMD* and a 40% increase in isoprene emissions from BEISv3.61, as implemented in our ISOP-UMD simulation, to assess consequences for the production of surface ozone and related management strategies across the entire CONUS domain. As shown in Fig. 4.14, net production of surface ozone (ppb hr^{-1}) increases across the majority of the CONUS with the implementation of our isoprene-related improvements, relative to the baseline CAMx simulation. The largest differences (up to 0.5 ppb hr^{-1}) occur throughout the Eastern US, especially near expansive NO_x-emitting urban areas. Decreases in net ozone production only occur over areas that experience near-zero ozone production, including oceans and forests. A noticeable reduction occurs over the Ozark Mountain Region in

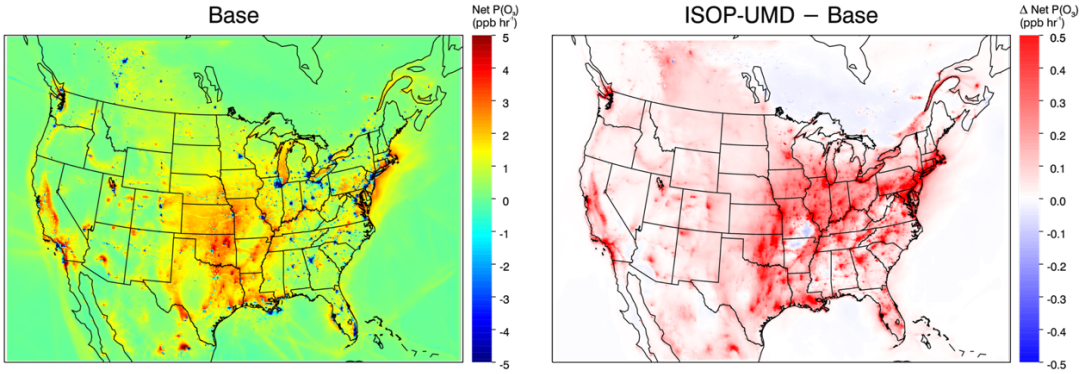

Fig. 4.14. Simulated net surface ozone production (ppb hr^{-1}) across the CONUS domain, averaged for the hours of 8–20 EDT across days on which daytime SENEX flights occurred. The left-hand panel shows net surface ozone production modeled using the baseline CAMx simulation, while the right-hand panel shows the difference in surface ozone production between the ISOP-UMD and baseline simulations. Note that the color bars saturate at −5 and 5 ppb hr^{-1} (left) and 0.5 ppb hr^{-1} (right).

Missouri and Arkansas, known for its plentiful isoprene emissions (Carlton and Baker, 2011). This behavior may be attributed to the loss of background ozone to VOC oxidation, which would be enhanced by increased emissions of isoprene in the ISOP-UMD simulation. Underestimation of net surface ozone production in the baseline CAMx simulation compared to ISOP-UMD suggests that stronger ozone control measures may be required to improve air quality than is indicated by standard regional modeling resources.

The isoprene modifications incorporated into ISOP-UMD also impact the characterization of ozone production regimes in CAMx. As mentioned in Section 4.4.2, CAMx determines whether ozone production is predominantly NO_x- or VOC-limited based on the ratio of $P(H_2O_2)$ to $P(HNO_3)$. Increased emissions of isoprene and production of HCHO in ISOP-UMD, relative to the baseline simulation, generates more HO_2 for radical termination, whereas production of HNO_3 is limited by modeled NO_x, and is therefore not substantially affected (Fig. 4.12). Consequently, $P(H_2O_2)/P(HNO_3)$ increases in ISOP-UMD, relative to the baseline simulation, and ozone production becomes more NO_x-limited, as shown in Fig. 4.15. This figure shows daytime ratios from the baseline and ISOP-UMD simulations, extracted at ground level for three locations of interest – Georgia (GA), Maryland (MD), and New York (NY) – from the full domain. These locations are impacted substantially by isoprene emissions and are selected to differentiate between regions of low (GA), moderate (MD), and high (NY) net ozone production, respectively, based on the map from Fig. 4.13a. The color bar reflects the relationship between $P(H_2O_2)/P(HNO_3)$ and ozone production regime, with hot colors representative of NO_x-limited ozone production and cool colors representative of VOC-limited ozone production, separated at a ratio of 0.35.

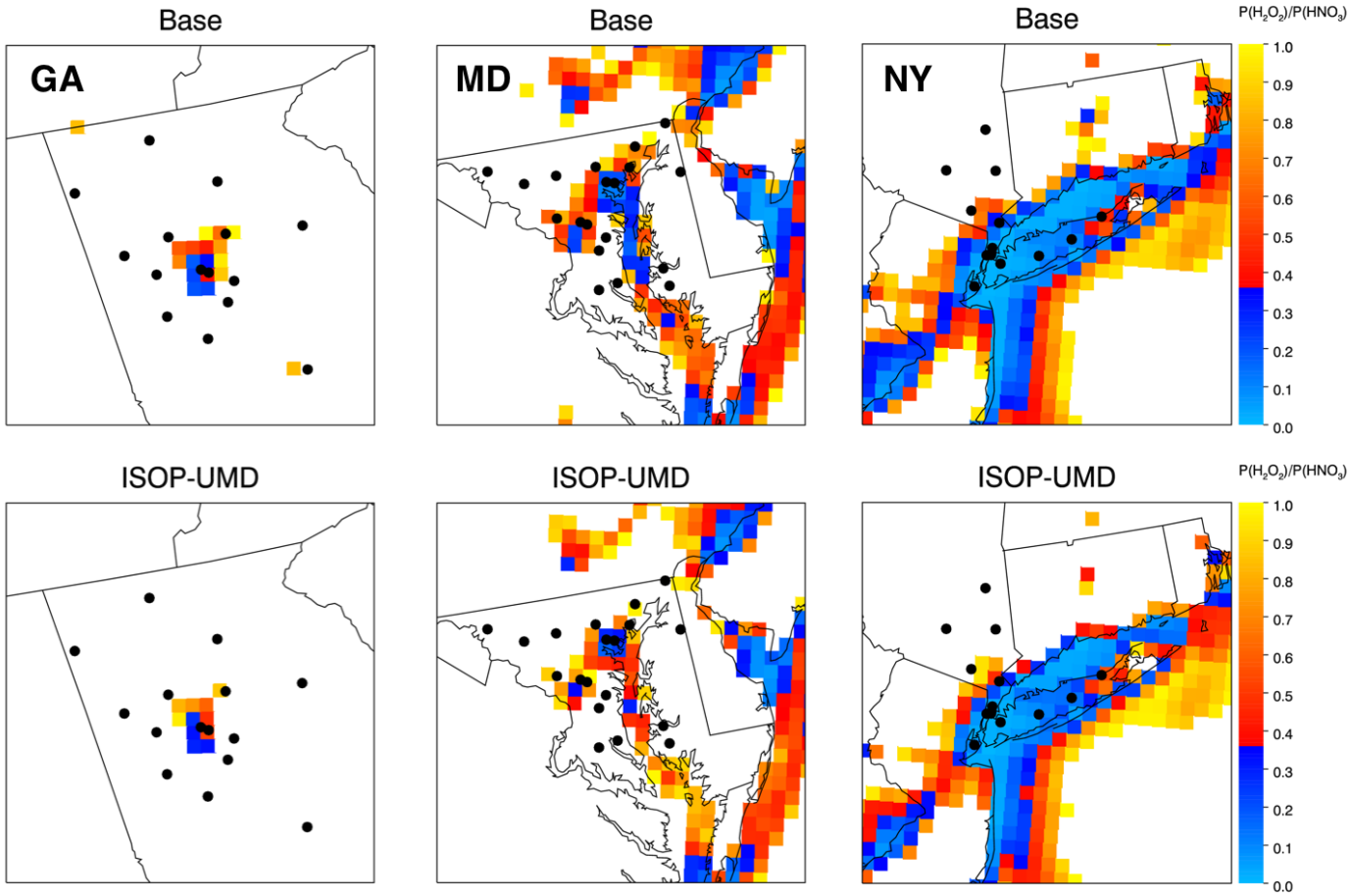

Fig. 4.15. Simulated $P(H_2O_2)/P(HNO_3)$ (unitless) at the surface, averaged for the hours of 8–20 EDT across days on which daytime SENEX flights occurred. The different panels show model results from the baseline (top) and ISOP-UMD simulations (bottom) and feature selected regions from the continental US domain: GA (left), MD (middle), and NY (right). The color bar distinguishes the prevailing ozone production regime in each grid cell, identified as NO_x-limited (hot) where $P(H_2O_2)/P(HNO_3) > 0.35$ and VOC-limited (cool) where $P(H_2O_2)/P(HNO_3) < 0.35$. White space represents grid cells where $P(H_2O_2)/P(HNO_3) > 1$.

In certain cases, the shift toward NO_x-limited ozone production is substantial enough to cause a transition out of a predominantly VOC-limited regime. This transition occurs in only one grid cell in GA, but much more commonly throughout the large urban areas surrounding MD and NY (~30 grid cells each). Although some grid cells remain more sensitive to VOC conditions, the transition of several cells from VOC-limited to NO_x-limited ozone production with our improvements to the model representation of isoprene suggests that standard regional modeling platforms underestimate the sensitivity of ozone production to changes in NO_x conditions at those locations. From a policy standpoint, this means that greater progress towards ozone attainment may be achieved by controlling NO_x emissions over VOC emissions, especially in problem areas like MD and NY. Further support for this implication is provided by Ring et al. (2018), who discovered that near-shore ship emissions supplied by the NEI are erroneously attributed to the surface layer in coastal grid cells. Adjustment of these emissions by distribution into higher vertical layers, as in Ring et al., is expected to reduce NO_x mixing ratios in coastal surface cells, which may intensify the shift toward NO_x-limited ozone production shown here.

Please note, however, that the CAMx approach to regime identification does not account for uncertainty in the $P(H_2O_2)/P(HNO_3)$ ratio at which regime transition occurs. Sillman et al. (1995), from which the CAMx approach is derived, apply the ratio of H_2O_2/HNO_3 mixing ratios and suggest that regime transition may occur at ratios between 0.3 and 0.5, depending on location and environmental conditions. Therefore, we encourage future evaluation of the regime identification methods applied in CAMx for validation of these implications.

Another policy-relevant indicator is maximum daily average 8-hour (MDA8) ozone, which is used in assessing ozone attainment with respect to the 70 ppb NAAQS. If the annual fourth-highest MDA8 at any given location averages over 70 ppb for the preceding three years, that location is in nonattainment of the 70 ppb NAAQS, and a strategy for meeting attainment must be incorporated into state policy. We evaluate the effects of ISOP-UMD on modeled MDA8 relative to the baseline simulation by comparison to surface observations for the same regions examined in Fig. 4.14. Hourly observations of surface ozone are obtained by the EPA's air quality system (AQS), which comprises a network of ground-level ozone monitors with locations in the GA, MD, and NY states denoted in Fig. 4.14. Model-measurement comparisons are shown in Fig. 4.16, with demarcations at 70 ppb to identify daily exceedances of the NAAQS. The ISOP-UMD simulation exaggerates a tendency of the baseline simulation to overestimate the magnitude of MDA8, which we have shown is largely affected by model processes beyond photochemistry, such as initial conditions, boundary conditions, mixing, or deposition. Although the largest deviation from the observation, by magnitude, occurs in GA (22−28%), both MD and NY experience a larger number of false-positive ozone exceedances, which increase substantially with the implementation of ISOP-UMD. Although most true exceedances are captured by the model, a tendency to additionally predict artificial ozone exceedances may lead to the misallocation of valuable ozone management resources. Therefore, it is critical to continue to improve the regional simulation of ozone and its precursors to ensure that such resources are optimally utilized.

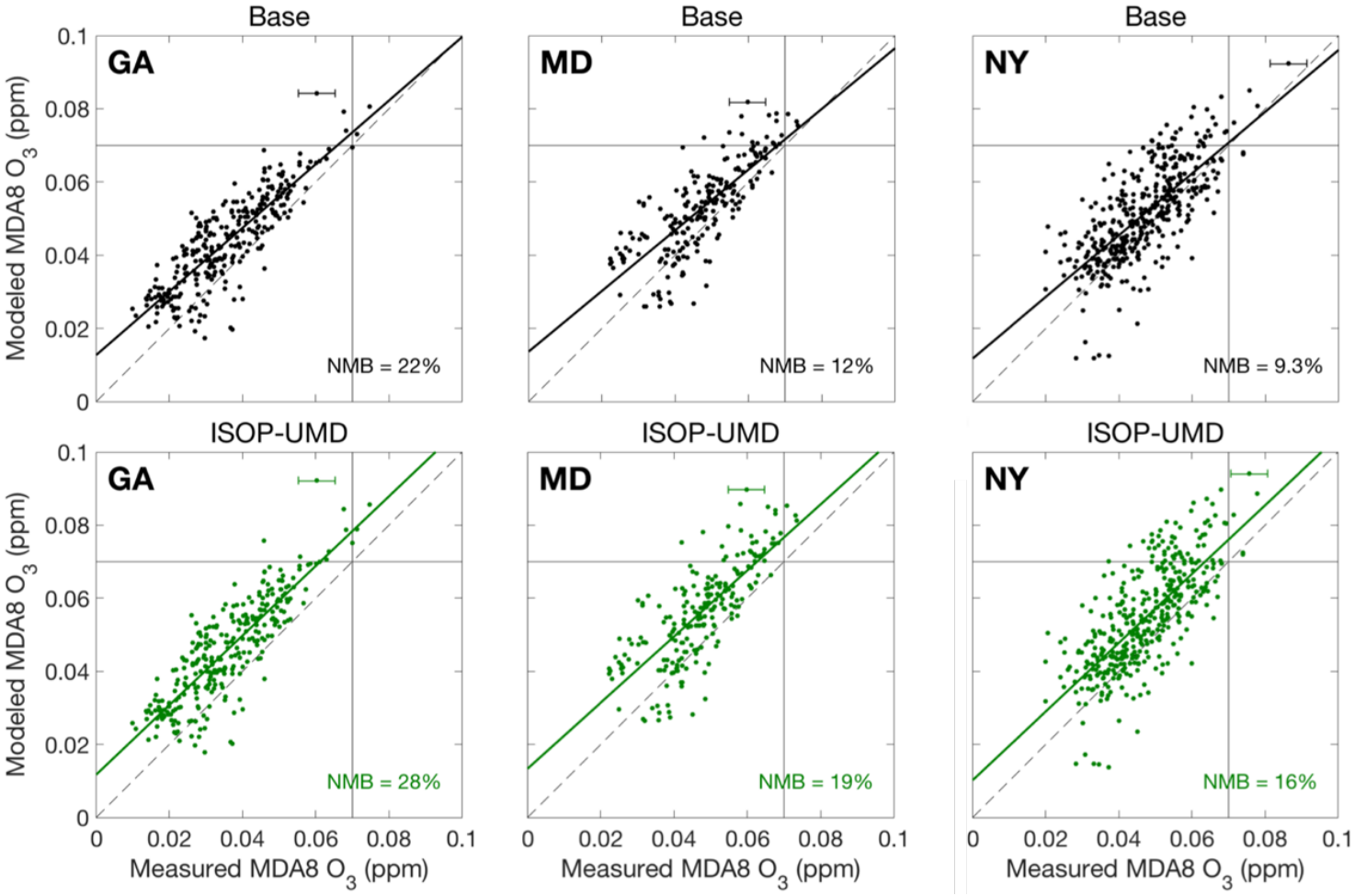

Fig. 4.16. Scatter of modeled versus measured MDA8 ozone (ppm), at ground monitor locations for days on which SENEX flights occurred. The different panels show comparisons using the baseline (top) and ISOP-UMD simulations (bottom) and feature selected regions from the continental US domain: GA (left), MD (middle), and NY (right).

4.6 Conclusions

In this work, we implement modifications to isoprene oxidation chemistry, as represented within a regional modeling framework. Modifications to the CB6r2 chemical mechanism are applied to the CAMx regional model, based on recommendations from the box modeling study of Marvin et. al (2017). These recommendations comprise the CB6r2-UMD mechanism, specifically designed to improve HCHO production from isoprene oxidation. In addition to the modifications from Marvin et al. (2017), we find that additional minor modifications, referred to throughout this study as 'CB6r2-UMD*', are required to account for errors in the production of PAN that become important within a regional modeling environment. Each of the CB6r2, CB6r2-UMD, and CB6r2-UMD* mechanisms are used to simulate atmospheric composition over the continental US during the summer of 2013. All three simulations are evaluated with respect to *in situ* observations and inferred reaction rates from the SENEX aircraft campaign, which focuses model-measurement comparisons on the isoprene-rich summertime Southeast US. Analysis emphasizes the impacts of improved isoprene chemistry on the regional modeling of surface ozone and its photochemical precursors.

Model evaluation with respect to SENEX observations shows that the modifications incorporated into CB6r2-UMD and CB6r2-UMD* improve the simulation of several ozone precursors. For example, VOCs such as HCHO and PNs improve incrementally with each update to the chemistry. However, all three mechanisms underestimate isoprene itself by ~40%, which dampens the degree of improvement achieved in its oxidation products. The new mechanisms also tend to increase NO_x mixing ratios, though the quality of model performance is ambiguous,

depending on which measurements of NO_2 are used as a basis for comparison. Although net ozone production improves with our modifications to the chemistry, simulated ozone mixing ratios are overestimated in the baseline simulation by 11% and, due to predominantly NO_x-limited conditions during SENEX, tend to increase with simulated NO_x, which worsens agreement with observations. A comparison of modeled to measured vertical profiles of ozone and CO suggests that a corrective reduction in modeled ozone mixing ratios may not be attainable through improvements to the photochemistry but instead may perhaps be achieved through improvements to the model representation of physical processes such as vertical mixing.

Results from our analysis have several important implications. Despite a potential contribution from vertical mixing, the underestimation of isoprene mixing ratios and HCHO production from isoprene oxidation in all three of our simulations implies a 30–40% low bias of isoprene emissions from BEISv3.61. Correction of this bias, combined with the CB6r2-UMD* mechanism in a simulation that we refer to as 'ISOP-UMD,' significantly improves model-measurement agreement for isoprene and HCHO. Isoprene matches observations within 1%, and agreement for HCHO (−16%) approaches that achieved by the best constrained box model simulations from Marvin et al. (2017). As our best known representation of NO_x and VOCs, we apply ISOP-UMD also to determine consequences for the simulation and management of surface ozone. For example, we find that net surface ozone production increases substantially (up to 0.5 ppb hr^{-1}) across the continental US, especially near urban areas, which may suggest a need for stronger ozone control measures than is indicated by standard regional modeling scenarios. The implementation of ISOP-UMD also shifts surface ozone toward more NO_x-limited production, which indicates that ozone production

responds more quickly to reductions in NO_x emissions than would normally be expected. Finally, ISOP-UMD exaggerates a tendency to overestimate MDA8 and predict false-positive ozone exceedances, which could lead to the inefficient application of valuable ozone management resources.

Moving forward, we encourage investigation into a number of related topics so that the scientific community can continue to improve the regional simulation of ozone and its precursors. Despite improvement in the simulation of isoprene and its oxidation products, the persisting underestimation of HCHO indicates a deficit of VOC oxidation that remains to be resolved. Furthermore, inconsistent NO_x measurements produce conflicting model assessments that must be reconciled before we can reliably evaluate the quality of NO_x emissions. Sustained efforts to improve the regional simulation of ozone precursors such as these, as well as the underlying physical processes, will not only continue to improve modeled ozone, but will also continue to facilitate the development of more effective air quality policy.

Chapter 5: Conclusion

5.1 Summary

This body of work comprises the preparation and application of the Framework for 0-D Atmospheric Modeling (F0AM) (Wolfe et al., 2016b) and the Comprehensive Air Quality Model with Extensions (CAMx) (www.camx.com), in combination with observations from the Southeast Nexus (SENEX) aircraft campaign (Warneke et al., 2016), to the quantitative analysis of the atmospheric oxidation of isoprene (C_5H_8). Science questions addressed in this dissertation specifically target the representation of isoprene chemistry and emissions in the computer models that simulate atmospheric photochemistry and consider the impacts of isoprene oxidation on the simulation of surface ozone (O_3) as well as the formulation of air quality policy.

In Chapter 2, my contributions to the development of the F0AM and CAMx models are described, within the context of the guiding science questions. For F0AM, I assembled a suite of gas-phase chemical mechanisms to facilitate the evaluation and comparison of several interpretations of isoprene oxidation chemistry. Some mechanisms – including the Carbon Bond 2005 (CB05) mechanism (Yarwood et al., 2005) and the Master Chemical Mechanism version 3.2 (MCMv3.2) (Jenkin et al., 1997; Saunders et al., 2003) – I updated from existing work, while others – namely the CB version 6 revision 2 (CB6r2) (Hildebrandt Ruiz and Yarwood, 2013) and the Master Chemical Mechanism version 3.3.1 (MCMv3.3.1) (Jenkin et al., 2015) – I developed from scratch. For CAMx, I constructed a platform for simulating atmospheric composition across the continental US (CONUS) during the summer of 2013, which

facilitates evaluation of isoprene chemistry and emissions with respect to observations from SENEX. Isoprene chemistry is represented using the CB6r2 mechanism, and isoprene emissions are represented using the Biogenic Emissions Inventory System version 3.61 (BEISv3.61) (Bash et al., 2016). Use of the CAMx model also provides access to valuable ozone assessment tools that can be used to quantify impacts of atmospheric isoprene oxidation on the production of surface ozone and determine consequences for policy-relevant ozone management strategies. My contributions to the development and application of F0AM are recognized with my co-authorship on its description paper, published by Wolfe et al. on 20 September 2016 in *Geoscientific Model Development*, and several additional papers: Wolfe et al. (2015), Wolfe et al. (2016a), and Roberts et al. (in preparation). My development of the CONUS 2013 platform for CAMx, together with the scientific application of this platform as described in Chapter 4, will soon be submitted for publication to the journal *Atmospheric Environment*.

In Chapter 3, *in situ* observations from the 2013 SENEX mission are combined with F0AM to evaluate and improve the simulation of isoprene oxidation chemistry. Five commonly used gas-phase chemical mechanisms – CB05, CB6r2, MCMv3.2, MCMv3.3.1, and a recent version of GEOS-Chem (Fisher et al., 2016; Kim et al., 2015; Mao et al., 2013b; Marais et al., 2016; Travis et al., 2016) – are evaluated and inter-compared with respect to formaldehyde (HCHO), a high-yield product of isoprene oxidation. Though HCHO mixing ratios are underestimated by all considered mechanisms, the mechanisms generally reproduce the dependence of observed HCHO on conditions for NO_x ($NO_x = NO + NO_2$). Observed HCHO mixing ratios are best reproduced by MCMv3.3.1 (normalized mean bias = −15%), followed by GEOS-Chem

(−17%), MCMv3.2 (−25%), CB6r2 (−32%) and CB05 (−33%). Inter-comparison of HCHO production rates reveals that major restructuring of the isoprene oxidation scheme in the Carbon Bond mechanism increases HCHO production by only ∼5% in CB6r2 relative to CB05, while further refinement of the complex isoprene scheme in the Master Chemical Mechanism increases HCHO production by ∼16% in MCMv3.3.1 relative to MCMv3.2. The GEOS-Chem mechanism provides a good approximation of the explicit isoprene chemistry in MCMv3.3.1 and generally reproduces the magnitude and source distribution of HCHO production rates. Improvements to the isoprene scheme in CB6r2 are derived and incorporated into a new mechanism called 'CB6r2-UMD', designed to preserve computational efficiency. The CB6r2-UMD mechanism mimics production of HCHO in MCMv3.3.1 and demonstrates good agreement with observed mixing ratios from SENEX (−14%). Improved simulation of HCHO also impacts modeled ozone: at ∼0.3 ppb NO, the ozone production rate increases ∼3% between CB6r2 and CB6r2-UMD, and it rises another ∼4% when HCHO is constrained to match observations. I am the lead author on this chapter, which was published on 30 May 2017 in *Atmospheric Environment*.

In Chapter 4, improvements to the isoprene chemistry within the CB6r2 chemical mechanism are implemented using the CAMx regional model and evaluated using observations from SENEX. Improvements are based on the CB6r2-UMD mechanism from Chapter 3 but require further modifications for compatibility with a regional modeling framework, which are incorporated into a new mechanism called 'CB6r2-UMD*'. Using the CONUS 2013 modeling platform, implementation of improved isoprene chemistry improves agreement with SENEX observations of HCHO

(−29%) relative to CB6r2 (−40%). However, isoprene itself is underestimated compared to SENEX observations by ~40% in all cases, which dampens the benefit to simulated HCHO. A 40% increase to isoprene emissions from BEISv3.61, combined with improved isoprene chemistry from CB6r2-UMD*, brings simulated isoprene into agreement with observations and significantly improves model-measurement agreement for HCHO (−16%), approaching the best agreement achieved by the constrained box model simulations from Chapter 3. Although such improvements to isoprene chemistry and emissions exaggerate a tendency of the regional modeling platform to overestimate surface ozone (>11%), net ozone production rates are consistently underestimated by ~30% compared to SENEX. Application of the CAMx ozone assessment tools demonstrates that net surface ozone production increases (by up to 0.5 ppb hr^{-1}) and becomes more NO_x-limited across the CONUS domain, which suggests that ozone control strategies may be more effective and that ozone production may be more responsive, specifically to reductions in NO_x emissions, than is indicated by standard regional modeling scenarios.

5.2 Future Work

Although this body of work makes considerable progress towards addressing the driving science questions, certain details could benefit from continued investigation. For example, Chapter 3 demonstrates that residual uncertainties in isoprene oxidation chemistry result in a deficit of volatile organic compound (VOC) oxidation, limiting the production of HCHO in all considered gas-phase mechanisms. Future laboratory or chamber studies may resolve these residual uncertainties and close

the gap between modeled and measured HCHO. Such studies may also provide insight into other aspects of isoprene oxidation, such as the impact of HO_x ($HO_x = OH + HO_2$) recycling on ambient mixing ratios of isoprene, or the production of numerous other isoprene oxidation products besides HCHO. Although rare, due to the difficulty of measuring such species, *in situ* observations of HO_x radicals could provide similar information. As demonstrated by Hembeck et al. (2019) concentrations of the HO_2 and RO_2 radicals can be inferred from standard aircraft observations, and innovative new resources such as these could be instrumental in expanding the scientific understanding of isoprene oxidation chemistry.

Further investigation is also recommended to quantify contributions to the regional modeling of isoprene beyond simple photochemistry. For example, Chapter 4 reveals that deficiencies in the simulation of vertical mixing and biogenic emissions degrade simulated isoprene mixing ratios compared to observations. Uncertainties in vertical mixing could be evaluated through the use of *in situ* observations of meteorological variables, radiosondes, or lidar measurements, all of which provide useful information related to mixing and depth of the planetary boundary layer (Banks et al., 2016; Banks and Baldasano, 2016). A comprehensive evaluation of isoprene emissions would also be useful in refining the 40% adjustment to BEISv3.61 that is applied in Chapter 4. Such an evaluation might include a comparison to simulated emissions from the most recent version of a another leading inventory, the Model of Emissions of Gases and Aerosols from Nature (MEGAN) (Guenther et al., 2012). Remote observations, such as HCHO column measurements from the Ozone Monitoring Instrument (OMI) aboard the Aura satellite (De Smedt et al., 2015; González Abad et al., 2015) or from the new Tropospheric Monitoring Instrument

(TROPOMI) aboard the Sentinel-5 Precursor satellite (http://www.tropomi.eu/data-products/formaldehyde), should also be incorporated, as these observations provide another means for evaluating simulated HCHO, and they can be inverted to derive an observationally-constrained estimate of isoprene emissions (Kaiser et al., 2018; Marais et al., 2012; Millet et al., 2008; Palmer et al., 2003).

Chapter 4 also exposes a persistent underestimation in simulated net ozone production rates that remains to be resolved. Further evaluation of the emissions and chemistry of ozone precursors beyond just isoprene will continue to advance the field with respect to the simulation of photochemical ozone production rates. For example, *in situ* observations of HCHO collected during the 2015 Wintertime Investigation of Transport, Emissions, and Reactivity (WINTER) campaign (https://www.eol.ucar.edu/field_projects/winter) could be applied to evaluate production from the oxidation of anthropogenic VOCs, which become important during the wintertime (Luecken et al., 2012). Observationally-constrained estimates of radicals important to ozone production, such as HO_2 and RO_2 (Hembeck et al., 2019), may be also useful in elucidating the contributions of various VOCs to ozone production. *In situ* observations of HO_2 and RO_2 collected in support of the recent Atmospheric Tomography Mission (ATom) (https://espo.nasa.gov/atom/content/ATom), which sampled the remote atmosphere over the Atlantic and Pacific Oceans during the summer of 2018, may provide similar information and could also be used to evaluate the production of background ozone and its impact on model boundary conditions.

Finally, this body of work suggests that, despite the substantial underestimation of net ozone production rates, standard regional modeling scenarios consistently overestimate simulated ozone mixing ratios, which also remains to be corrected.

Chapter 4 provides evidence that this overestimation is influenced to some extent by excessive vertical mixing, which supports the recent hypotheses of Travis et al. (2016). As mentioned above, the simulation of vertical mixing in regional models may be evaluated through the application of various meteorological and boundary layer observations. Besides vertical mixing, the contributions of other physical influences to the simulation of ozone mixing ratios could be quantified using CAMx probing tools, such as the ozone source apportionment tool (OSAT). Boundary conditions may be evaluated using new observations from the remote ATOM mission, as previously mentioned, and ozone deposition rates could be evaluated through the derivation and application of eddy covariance fluxes, as in Wolfe et al. (2015). Thus, sustained efforts to resolve remaining uncertainties related to various atmospheric processes are essential for achieving further improvement in the atmospheric modeling of surface ozone and related air quality policy.

Appendix A: Example model setup scripts

This appendix presents example model setup scripts for the Framework for 0-Dimensional Atmospheric Modeling (F0AM) and the Comprehensive Air Quality Model with Extensions (CAMx). Fig. A.1. demonstrates a F0AM setup script that is optimized for a simulation in support of an aircraft field study application. Fig. B.1. demonstrates a CAMx setup script for a simulation utilizing the Continental US (CONUS) 2013 modeling platform.

Fig. A.1. Example model setup script for F0AM. This script represents a setup typical for a simulation in support of an aircraft field study. Several variables are constrained to aircraft observations, and photolysis is optimized for a solar radiation source. This particular example runs photochemistry defined by the CB6r2 gas-phase chemical mechanism.

Senex.m 9/19/18, 3:06 PM

```
% Senex.m
% This program runs F0AM constrained by meteorological and chemical
% observations from the SENEX 2013 aircraft field campaign.
% 20140821 mmarvin

clear

%% DATA LOADING
% Load formatted data here into the structure 'D'.
% To see an example of how to generate such data, take a look at
    Convert2UWCM_BPEX07.m.

load('SENEX_AllData_60s_20150422.mat');
D.i = find((D.StaticPrs >= 0.) & (D.CH4_ppb >= 0.) & (D.CO_ppbv >= 0.)...
    & (D.O3_ppbv >= 0.) & (D.NO_ppbv >= 0.) & (D.NO2_ppbv >= 0.)...
    & (D.isoprene_pptv >= 0.) & (D.PAN_ppbv >= 0.) & (D.methanol_pptv >= 0.)...
    & (D.j_O3_up >= 0.));

%% SOLAR CYCLE

SolarParam.lat = D.GpsLat(D.i); %degrees (-90:90, N is postive)
SolarParam.lon = D.GpsLon(D.i); %degrees (-180:180, E is positive)
SolarParam.alt = D.GpsAlt(D.i); %meters
SolarParam.startTime = D.time_vec(D.i,:); %year month day hour minute second
    (in UTC)
SolarParam.nDays = 3; %integer

%% METEOROLOGY
%{
OPTIONS FOR INPUT:
 1) List of variables (useful if constraints will be manually changed)
 2) Load a .mat file containing the cell array Met

DETAILS:
 Each meteorological input (except jcorr) is specified by
 a 1-D column array located in the D structure. A model run will include
 the number of elements in each array in the structure.
 During the nth step of the model run, the nth element of each column array
 will specify the constraint for its respective variable.
 Since 'jcorr' is specified by a string (as opposed to a scalar or
 column array), its value is computed within the model as a ratio of
 MCM-parameterized j-values to the j-value. In this case, 'JNO2'
 is the utilized observation (corresponding to NO2 photolysis),
 and its observed values are given in the D structure.
%}

Met = {...
%   names        values
    'P'          D.StaticPrs(D.i)                    ;...    %Pressure, mbar
    'T'          D.AmbTemp(D.i)+273.15               ;...    %Temperature, K
    'RH'         D.RelHumidity(D.i)                  ;...    %Relative humidity
        , %
    'kdil'       1/86400                             ;...    %Dilution constant
        , /sec
    'jcorr'      {'JO1D','JNO2'}                     ;...    %Correction factor
```

Page 1 of 4

```
        for j-values
    'JO1D'      D.j_O3_up(D.i)+D.j_O3_down(D.i)     ;...
    'JNO2'      D.j_NO2_up(D.i)+D.j_NO2_down(D.i)   ;...
    'ALT'       D.GpsAlt(D.i)                       ;...    %Altitude, m
        (default: 500)
    'O3col'     300                                 ;...    %Column ozone, DU
        (default: 350)
    'albedo'    0.05                                ;...    %Albedo (default:
        0.01)
    };

%% CHEMICAL CONCENTRATIONS
%{
OPTIONS FOR INPUT:
 1) List of variables (useful if constraints will be manually changed)
 2) Load a .mat file containing the cell array InitConc

Valid values for HoldMe:
 1: Hold constant for each step
 0: Do not hold constant.
    Also, if ModelOptions.LinkSteps = 1 (see below), initialize first step only
        .

DETAILS:
 Non-zero concentrations are specified by a 1-D
 column array located in the D structure. The number of model steps of a
 model run corresponds to the number of elements in each array.
 During the nth step of the model run, the nth element of each column array
 will specify the initial concentration for its respective species. Species
     whose
 concentrations are  specified by a scalar (H2) are assumed to have
 the same initial value for all steps.
 Species with HoldMe = 1 will be held constant throughout each step.
 Species with HoldMe = 0 will only be initialized at the start of the run.
 If ModelOptions.LinkSteps = 1 (below), species with HoldMe = 0 will NOT
 be updated to observations for subsequent model steps. Also,these species
 and those not appearing in InitConc will have initial concentrations for
 subsequent steps determined by the final concentrations of the previous step.
%}

InitConc = {...
%   names           conc(ppb)                               HoldMe
    'CH4'           D.CH4_ppb(D.i)                           1;...
    'H2'            550                                      1;...
    'CO'            D.CO_ppbv(D.i)                           1;...
    'O3'            D.O3_ppbv(D.i)                           1;...
    'NO'            D.NO_ppbv(D.i)                           0;...
    'NO2'           D.NO2_ppbv(D.i)                          1;...
    'ISOP'          D.isoprene_pptv(D.i)/1000                1;...
    'PAN'           D.PAN_ppbv(D.i)                          1;...
    'MEOH'          D.methanol_pptv(D.i)/1000                1;...
    };

%% CHEMISTRY
%{
 Cell array of strings specifying script files containing all desired
```

```
 chemical sub-mechanisms. Refer to F0AMv3_readme.docx for information
 on how these scripts are written and how to make your own.
%}

ChemFiles = {...
    'CB6r2_K(Met)';...
    'CB6r2_J(Met,2)';...
    'CB6r2_AllRxns';...
    };

%% DILUTION
%{
OPTIONS FOR INPUT:
 1) List of variables (useful if constraints will be manually changed)
 2) Load a .mat file containing the cell array BkgdConc

DETAILS:
 Concentrations will be diluted at a rate constant given by kdil in
 the Met structure (above). Setting the 'DEFAULT' value to 1 will force
 the background concentrations to be the same as those in InitConc.
 All other species will have backgro und concentrations of 0.
%}

BkgdConc = {...
%   names           values (ppbv)
    'DEFAULT'       0;...   %0 for all zeros, 1 to use InitConc
    };

%% MODEL OPTIONS
%{
 Verbose is enabled, so progress and run times will be displayed in the command
     window.
 EndPointsOnly is enabled, so only the last point of each step will be given in
     the output.
 SavePath gives a filename, but if no directory is given it will be saved in
     the default
 \F0AMv3.1\Runs\ directory.
 TimeStamp specifies values to use to replace the 'Time' variable in the output
     .
 For this to make sense, this variable must be the same length as the input
     arrays
 in Met and InitConc, and EndPointsOnly must be enabled (so that the number of
     outputs is
 equal to (number of inputs) x (number of repetitions).
%}

ModelOptions.FixNOx = 0; %flag for scaling total NOx to constraints
ModelOptions.Verbose = 2; %flag for verbose output
ModelOptions.EndPointsOnly = 1;   %flag for concentration and rate outputs
ModelOptions.LinkSteps = 0;  %flag for using end-points of one run to
    initialize next run
ModelOptions.Repeat = 1; %number of times to loop through all constraints
ModelOptions.SavePath = '/Users/Magatron/Documents/MATLAB/F0AMv3.1/Setups/Senex
    /Runs/'; %partial or full path or empty
ModelOptions.TimeStamp = D.doy_frac(D.i); %time stamp to overwrite S.Time model
    output
```

```
ModelOptions.IntTime = 3600;

%% MODEL RUN
%{
 The structure S will contain all the model output, which is also saved
     according
 to SavePath (above).
%}

S = F0AM_ModelCore(Met,InitConc,ChemFiles,BkgdConc,ModelOptions,SolarParam);

clear Met InitConc ChemFiles BkgdConc ModelOptions SolarParam
```

Fig. A.2. Example model setup script for CAMx. This script represents the base simulation from the CONUS 2013 modeling platform, which runs photochemistry defined by the CB6r2h gas-phase chemical mechanism. The model runs at hourly, 12km resolution for the CONUS domain from 21 May through 15 July of 2013, coincident with the SENEX 2013 aircraft campaign. Inputs are day-specific and require extensive pre-processing.

CAMx.v6.50.Base.CONUS.2013.MPICH3.job 9/19/18, 3:39 PM

```
#!/bin/csh
#
# CAMx 6.50
#

set EXEC    = "/homes/metogra/mmarvin/camx/camx6.50/
    CAMx.v6.50.MPICH3.NCF3.gfortran"
#
set NAME    = "Base.CONUS.2013"
set RUN     = "v6.50.${NAME}.MPICH3"
set INPUT   = "/local/data/mmarvin/camx/2013"
set MET     = "$INPUT/met"
set EMIS_A  = "$INPUT/emis_area"
set EMIS_P  = "$INPUT/emis_point"
set ICBC    = "$INPUT/icbc"
set CHEM    = "/homes/metogra/mmarvin/camx/camx6.50/CHEM"
set OUTPUT  = "/data/chemstg63/mmarvin/camx/2013/output"
#
mkdir -p $OUTPUT
#
#  --- Create the nodes file  ---
#
cat << ieof > nodes
129.2.124.43:21
ieof
set NUMPROCS = 21
#
#  --- set the dates and times ----
#
set RESTART = "NO"
foreach today (05.21 05.22 05.23 05.24 05.25 05.26 05.27 05.28 05.29 05.30
    05.31 06.01 06.02 06.03 06.04 06.05 06.06 06.07 06.08 06.09 06.10 06.11
    06.12 06.13 06.14 06.15 06.16 06.17 06.18 06.19 06.20 06.21 06.22 06.23
    06.24 06.25 06.26 06.27 06.28 06.29 06.30 07.01 07.02 07.03 07.04 07.05
    07.06 07.07 07.08 07.09 07.10 07.11 07.12 07.13 07.14 07.15)
set MONTHDAY = $today
set MONTH = $MONTHDAY:r
set YMONTH = $MONTHDAY:r
set CAL = $MONTHDAY:e
set YESTERDAY = `echo ${CAL} | awk '{printf("%2.2d",$1-1)}'`
#
if (${CAL} == 01) then
    if (${MONTH} == 06) then
        set YMONTH = 05
        set YESTERDAY = 31
    endif
    if (${MONTH} == 07) then
        set YMONTH = 06
        set YESTERDAY = 30
    endif
endif
#
if( ${RESTART} == "NO" ) then
        set RESTART = "false"
else
        set RESTART = "true"
```

Page 1 of 4

```
endif
#
#  --- Create the input file (always called CAMx.in)
#
cat << ieof > CAMx.in

 &CAMx_Control

 Run_Message      = 'CAMx 6.50 Base CONUS 2013 -- CB6r2h_CF and BEISv3.61
     $RUN',

!--- Model clock control ---

 Time_Zone        = 0,                ! (0=UTC,5=EST,6=CST,7=MST,8=PST)
 Restart          = .${RESTART}.,
 Start_Date_Hour  = 2013,${MONTH},${CAL},0000,   ! (YYYY,MM,DD,HHmm)
 End_Date_Hour    = 2013,${MONTH},${CAL},2400,   ! (YYYY,MM,DD,HHmm)

 Maximum_Timestep    = 5.,            ! minutes
 Met_Input_Frequency = 60.,           ! minutes
 Ems_Input_Frequency = 60.,           ! minutes
 Output_Frequency    = 60.,           ! minutes

!--- Map projection parameters ---

 Map_Projection   = 'LAMBERT',  ! (LAMBERT,POLAR,UTM,LATLON)
 UTM_Zone         = 0,
 Longitude_Pole   = -97.,      ! deg (west<0,south<0)
 Latitude_Pole    =  40.,      ! deg (west<0,south<0)
 True_Latitude1   =  45.,      ! deg (west<0,south<0)
 True_Latitude2   =  33.,      ! deg (west<0,south<0)

!--- Parameters master (first) grid ---

 Number_of_Grids      = 1,
 Master_SW_XCoord     = -2556.,       ! km or deg, SW corner of cell (1,1)
 Master_SW_YCoord     = -1728.,       ! km or deg, SW corner of cell (1,1)
 Master_Cell_XSize    = 12.,          ! km or deg
 Master_Cell_YSize    = 12.,          ! km or deg
 Master_Grid_Columns  = 459,
 Master_Grid_Rows     = 299,
 Number_of_Layers     = 35,

!--- Model options ---

 Diagnostic_Error_Check = .false.,      ! True = will stop after 1st timestep
 Flexi_Nest             = .false.
 Advection_Solver       = 'PPM',        ! (PPM,BOTT)
 Chemistry_Solver       = 'EBI',        ! (EBI,IEH,LSODE)
 PiG_Submodel           = 'None',       ! (None,GREASD,IRON)
 Probing_Tool           = 'None',       !
     (None,OSAT,GOAT,APCA,PSAT,DDM,PA,RTRAC)
 Chemistry              = .true.,
 Drydep_Model           = 'ZHANG03',    ! (None,WESELY89,ZHANG03)
 Wet_Deposition         = .true.,
 ACM2_Diffusion         = .true.,
```

```
 Surface_Model          = .false.,
 Inline_Ix_Emissions    = .true.,
 Super_Stepping         = .true.,
 Gridded_Emissions      = .true.,
 Point_Emissions        = .true.,
 Ignore_Emission_Dates  = .false.,

!--- Output specifications ---

 Root_Output_Name         = '$OUTPUT/CAMx.$RUN.2013${MONTH}${CAL}',
 Average_Output_3D        = .true.,
 NetCDF_Format_Output     = .true.,
 NetCDF_Use_Compression   = .false.,
 Output_Species_Names(1)   = 'NO',
 Output_Species_Names(2)   = 'NO2',
 Output_Species_Names(3)   = 'O3',
 Output_Species_Names(4)   = 'CO',
 Output_Species_Names(5)   = 'INTR',
 Output_Species_Names(6)   = 'NTR1',
 Output_Species_Names(7)   = 'NTR2',
 Output_Species_Names(8)   = 'PAN',
 Output_Species_Names(9)   = 'OH',
 Output_Species_Names(10)  = 'HO2',
 Output_Species_Names(11)  = 'RO2',
 Output_Species_Names(12)  = 'ISOP',
 Output_Species_Names(13)  = 'ISPD',
 Output_Species_Names(14)  = 'FORM',
 Output_Species_Names(15)  = 'MEOH',
 Output_Species_Names(16)  = 'PANX',
 Output_Species_Names(17)  = 'OPAN',

!--- Input files ---

 Chemistry_Parameters = '$CHEM/CAMx6.5.chemparam.CB6r2h_CF_SOAP_ISORROPIA',
 Photolyis_Rates      = '$INPUT/tuv/tuv.ps2str_CB6.13${MONTH}${CAL}',
 Ozone_Column         = '$INPUT/o3map/o3map.2013${MONTH}${CAL}.daily',
 Initial_Conditions   = '$ICBC/ICON_V5d_profile_12US1.bin',
 Boundary_Conditions  = '$ICBC/BCON.12US1.35L.CB05.2013${MONTH}${CAL}.25h.bin',
 Point_Sources        = '$EMIS_P/point.camx.v6.2013${MONTH}$
     {CAL}.base.wildfires.bin',
 Master_Grid_Restart  = '$OUTPUT/CAMx.$RUN.2013${YMONTH}${YESTERDAY}.inst',
 Nested_Grid_Restart  = '$OUTPUT/CAMx.$RUN.2013${YMONTH}${YESTERDAY}.finst',
 PiG_Restart          = ' ',
 Srfmod_Grid(1)       = ' ',

 Surface_Grid(1) = '$MET/camx.lu.12km.2013${MONTH}$
     {CAL}.bin.modislai.watermask',
 Met3D_Grid(1)    = '$MET/camx.3d.12km.2013${MONTH}${CAL}.bin',
 Met2D_Grid(1)    = '$MET/camx.2d.12km.2013${MONTH}${CAL}.bin',
 Vdiff_Grid(1)    = '$MET/camx.kv.12km.2013${MONTH}${CAL}.bin.ACM2.patch',
 Cloud_Grid(1)    = '$MET/camx.cr.12km.2013${MONTH}${CAL}.bin',
 Emiss_Grid(1)    = '$EMIS_A/area.camx.v6.2013${MONTH}${CAL}.base.seasalt.bin',

 /
!------------------------------------------------------------------------------
    -
```

```
ieof
#
#  --- Execute the model ---
#
if( ! { mpiexec -launcher rsh -machinefile nodes -np $NUMPROCS $EXEC } ) then
   exit
endif
set RESTART = "YES"

end
```

Appendix B: Mechanism scripts for implementation of CB6r2 in F0AM

This appendix compiles the CB6r2 mechanism scripts that I developed for implementation in the Framework for 0-Dimensional Atmospheric Modeling (F0AM). Fig. B.1. shows the first page of the base reaction script, which demonstrates how species and reaction rates are defined within the model. Fig. B.2. presents a script for assigning photolysis rates, and Fig. B.3. presents a script for parameterizing complex reaction rate constants.

Fig. B.1. First page of the base reaction script for CB6r2, as implemented in F0AM. All proceeding reactions are defined following the pattern established below. First, all considered species are specified. Then, each reaction is numbered, named, and assigned a reaction a rate constant. Reactants are identified specifically, and each participant species – reactant or product – is assigned a net yield.

CB6r2_AllRxns.m 9/19/18, 4:01 PM

```
% CB6r2_AllRxns.m
% # of species = 77
% # of reactions = 216
% For more information, please see CAMx User's Guide, Appendix A.
% NOTE: CB6r2 species "O" renamed "O3P"
%
% 20150415 MM   First build.
% 20160203 GMW  Checked against documentation.
% 20160606 MM   Updated for consistency with CAMx v 6.3.
% 20160708 MM   Updated J values for consistency with CB6r1 (no docs for CB6r2)

SpeciesToAdd = {...
'O1D'; 'O3P'; 'OH'; 'HO2'; 'C2O3'; 'XO2'; 'XO2N'; 'CXO3'; 'MEO2'; 'TO2'; ...
'ROR'; 'HCO3'; 'CRO'; 'BZO2'; 'EPX2'; 'ISO2'; 'OPO3'; 'RO2'; 'XLO2'; 'XO2H';
    ...
'AACD'; 'ACET'; 'ALD2'; 'ALDX'; 'BENZ'; 'CAT1'; 'CO'; 'CRES'; 'CRON'; 'EPOX';
    ...
'ETH'; 'ETHA'; 'ETHY'; 'ETOH'; 'FACD'; 'FORM'; 'GLY'; 'GLYD'; 'H2O2'; 'HNO3';
    ...
'HONO'; 'HPLD'; 'INTR'; 'IOLE'; 'ISOP'; 'ISPD'; 'ISPX'; 'KET'; 'MEOH'; 'MEPX';
    ...
'MGLY'; 'N2O5'; 'NO'; 'NO2'; 'NO3'; 'NTR1'; 'NTR2'; 'O3'; 'OLE'; 'OPAN'; ...
'OPEN'; 'PACD'; 'PAN'; 'PANX'; 'PAR'; 'PNA'; 'PRPA'; 'ROOH'; 'SO2'; 'SULF'; ...
'TERP'; 'TOL'; 'XOPN'; 'XYL'; 'ECH4'; 'H2'; 'CH4'; };

RO2ToAdd = {'RO2'};

AddSpecies

%1
i=i+1;
Rnames{i} = 'NO2 = NO + O3P';
k(:,i) = JNO2;
Gstr{i,1} = 'NO2';
fNO2(i)=fNO2(i)-1; fNO(i)=fNO(i)+1; fO3P(i)=fO3P(i)+1;

%2
i=i+1;
Rnames{i} = 'O3P = O3';
k(:,i) = 5.68e-34.*((T./300).^-2.6).*M.^2.*0.21;
Gstr{i,1} = 'O3P';
fO3P(i)=fO3P(i)-1; fO3(i)=fO3(i)+1;

%3
i=i+1;
Rnames{i} = 'O3 + NO = NO2';
k(:,i) = 1.40e-12.*exp(-1310./T);
Gstr{i,1} = 'O3'; Gstr{i,2} = 'NO';
fO3(i)=fO3(i)-1; fNO(i)=fNO(i)-1; fNO2(i)=fNO2(i)+1;

%4
i=i+1;
Rnames{i} = 'O3P + NO = NO2';
k(:,i) = 1.00e-31.*((T./300).^-1.6).*M;
Gstr{i,1} = 'O3P'; Gstr{i,2} = 'NO';
fO3P(i)=fO3P(i)-1; fNO(i)=fNO(i)-1; fNO2(i)=fNO2(i)+1;
```

Page 1 of 34

Fig. B.2. Photolysis rates assignment script for CB6r2, as implemented in F0AM. This script applies model setup options for the determination of photolysis rates. If the MCM parameterization option is selected, each photolysis rate is assigned to a corresponding set of parameters for calculation using Equation 2.4. If no direct analogues are available from the MCM, photolysis rates are assigned to literature cross sections and quantum yields for determination via the lookup table method.

CB6r2_J.m 9/19/18, 4:10 PM

```
function J = CB6r2_J(Met,Jmethod)
% function J = CB6r2_J(Met,Jmethod)
% Calculates photolysis frequencies for CB06r2.
%
% INPUTS:
% Met: structure containing required meteorological constraints. Required vars
    depend on Jmethod.
%       Met.SZA: solar zenith angle in degrees
%       Met.ALT: altitude, meters
%       Met.O3col: overhead ozone column, DU
%       Met.albedo: surface reflectance, 0-1 (unitless)
%       Met.T: temperature, T
%       Met.P: pressure, mbar
%       Met.LFlux: name of a text file containing an actinic flux spectrum
%
% Jmethod: numeric flag or string specifying how to calculate J-values. Default
    is 'MCM'.
%       0 or 'MCM':      use MCMv3.3.1 parameterization.
%                        Some reactions are not included in MCM. For these,
    "HYBRID" values are used.
%                        Required Met fields: SZA
%       1 or 'BOTTOMUP': bottom-up integration of cross sections/quantum yields
    .
%                        See J_BottomUp.m for more info.
%                        Required Met fields: LFlux, T, P
%       2 or 'HYBRID':   Interpolation of hybrid J-values from TUV solar
    spectra.
%                        See J_TUVhybrid.m for more info.
%                        Required Met fields: SZA, ALT, O3col, albedo
%
% OUTPUTS:
% J: structure of J-values.
%
% 20150218 MM   Adapted from CB05_J
% 20150618 GMW  Adapted from script to function
% 20160304 GMW  Changed output from name/value pairs to structure, added
    Jmethod.
% 20160708 MM   Added JMVK and JMACR

% INPUTS
struct2var(Met)

if nargin<2
    Jmethod = 'MCM';
elseif ischar(Jmethod)
    Jmethod = upper(Jmethod);
end

% J-Values
switch Jmethod
    case {0,'MCM'}
        Jmcm = MCMv331_J(Met,'MCM');

        % also need hybrid values for non-MCM species
        % override Met inputs to match hybrid and MCM J's (see Fig. 2 in
            description paper)
```

Page 1 of 2

```
            ALT    = 500*ones(size(SZA)); %meters;
            O3col  = 350*ones(size(SZA)); %DU
            albedo = 0.01*ones(size(SZA)); %unitless
            Jhyb   = J_Hybrid(SZA,ALT,O3col,albedo);

        case {1,'BOTTOMUP'}
            Jmcm = J_BottomUp(LFlux,T,P);
            Jhyb = Jmcm; %for name mapping

        case {2,'HYBRID'}
            Jmcm = J_Hybrid(SZA,ALT,O3col,albedo);
            Jhyb = Jmcm; %for name mapping

        otherwise
            error(['MCMv331_J: invalid Jmethod "' Jmethod ...
                '". Valid options are "MCM" (0), "BOTTOMUP" (1), "HYBRID" (2).'])
    end

    %rename
    J=struct;
    J.JNO2        = Jmcm.J4;
    J.JNO3_NO     = Jmcm.J5;
    J.JNO3_NO2    = Jmcm.J6;
    J.JHNO3       = Jmcm.J8;
    J.JO3P        = Jmcm.J2;
    J.JO1D        = Jmcm.J1;
    J.JHONO       = Jmcm.J7;
    J.JH2O2       = Jmcm.J3;
    J.JNTR        = Jmcm.J54;
    J.JCOOH       = Jmcm.J41;
    J.JCCHO_R     = Jmcm.J13;
    J.JC2CHO      = Jmcm.J14;
    J.JHCHO_M     = Jmcm.J12;
    J.JHCHO_R     = Jmcm.J11;
    J.JMGLY       = Jmcm.J34;
    J.JHPLD       = Jmcm.J20;
    J.JGLY        = Jmcm.J31 + Jmcm.J32 + Jmcm.J33;
    J.JACET       = Jmcm.J21;
    J.JMEK        = Jmcm.J22;
    J.JMVK        = Jmcm.J23 + Jmcm.J24; %added 20160708 mrm
    J.JMACR       = Jmcm.J18 + Jmcm.J19; %added 20160708 mrm

    % NO DIRECT MCM ANALOGUES
    J.JN2O5       = Jhyb.Jn19 + Jhyb.Jn20;
    J.JHO2NO2     = Jhyb.Jn21 + Jhyb.Jn22;
    J.JPAN        = Jhyb.Jn14 + Jhyb.Jn15;
    J.JACRO       = Jhyb.Jn11;
    J.JGLYD       = Jhyb.Jn9;
    J.JCRON       = Jhyb.Jn12 + Jhyb.Jn13;
```

Fig. B.3. Complex reaction rate constant parameterization script for CB6r2, as implemented in F0AM. Each reaction rate constant is numbered, named, and calculated according to its appropriate parameterization, which varies among reactions. Most of these rate constants conform to a Troe-type expression, culminating in a complex combination of low- and high-pressure rate constants.


```
function K = CB6r2_K(Met)
% function K = CB6r2_K(Met)
% Calculate generic rate constants for use with the CB6r2 chemical mechanism.
%
% INPUTS:
% Met: structure containing the following fields.
%   T: temperature, K
%   M: number density, molec/cm^3
%
% OUTPUTS:
% K: structure of rate constants. Each is size length(T) x # of rate constants
%
% 20150218 MM   Adapted from CB05_K.m
% 20160304 GMW  Output changed from name/value pair to structure, and input to
    structure.
% 20160517 MM   Corrected error in exponents for all termolecular reactions (-2
    vs 2).
%               This was an error in the original documentation.

struct2var(Met)

nk = 20; %number of rate constants
krx = nan(length(T),nk);
Knames = cell(nk,1);
i=0;

i=i+1;
Knames{i}   = 'K_O3P_NO2';
LPL         = 1.30E-31.*(T./300).^(-1.5).*M;
HPL         = 2.30E-11.*(T./300).^(0.24);
krx(:,i)    = (LPL./(1+LPL./HPL)).*0.6.^(1./(1+(log10(LPL./HPL)).^2));

i=i+1;
Knames{i}   = 'K_O3P_NO';
LPL         = 9.0E-32.*(T./300).^(-1.5).*M;
HPL         = 3.00E-11.*(T./300).^(-0.0);
krx(:,i)    = (LPL./(1+LPL./HPL)).*0.6.^(1./(1+(log10(LPL./HPL)).^2));

i=i+1;
Knames{i}   = 'K_OH_NO';
LPL         = 7.4E-31.*(T./300).^(-2.4).*M;
HPL         = 3.3E-11.*(T./300).^(-0.3);
krx(:,i)    = (LPL./(1+LPL./HPL)).*0.81.^(1./(1+((log10(LPL./HPL))./0.87).^2));

i=i+1;
Knames{i}   = 'K_OH_NO2';
LPL         = 1.8E-30.*(T./300).^(-3.0).*M;
HPL         = 2.8E-11;
krx(:,i)    = (LPL./(1+LPL./HPL)).*0.6.^(1./(1+(log10(LPL./HPL)).^2));

i=i+1;
Knames{i}   = 'K_OH_HNO3';
K1          = 2.4E-14.*exp(460./T)     ;
K3          = 6.5E-34.*exp(1335./T)    ;
K4          = 2.7E-17.*exp(2199./T)    ;
K2          = (K3.*M)./(1+(K3.*M./K4)) ;
```

```
krx(:,i)    = K1 + K2 ;

i=i+1;
Knames{i}   = 'K_OH_OLE';
LPL         = 8.0E-27.*(T./300).^(-3.5).*M;
HPL         = 3.0E-11.*(T./300).^(-1.0);
krx(:,i)    = (LPL./(1+LPL./HPL)).*0.5.^(1./(1+((log10(LPL./HPL))./1.13).^2));

i=i+1;
Knames{i}   = 'K_OH_ETH';
LPL         = 8.6E-29.*(T./300).^(-3.1).*M;
HPL         = 9.0E-12.*(T./300).^(-0.85);
krx(:,i)    = (LPL./(1+LPL./HPL)).*0.48.^(1./(1+((log10(LPL./HPL))./1.15).^2));

i=i+1;
Knames{i}   = 'K_OH_ETHY';
LPL         = 5.0E-30.*(T./300).^(-1.5).*M;
HPL         = 1.0E-12;
krx(:,i)    = (LPL./(1+LPL./HPL)).*0.37.^(1./(1+((log10(LPL./HPL))./1.3).^2));

i=i+1;
Knames{i}   = 'K_SO2_OH';
LPL         = 4.5E-31.*(T./300).^(-3.9).*M;
HPL         = 1.3E-12.*(T./300).^(-0.7);
krx(:,i)    = (LPL./(1+LPL./HPL)).*0.53.^(1./(1+((log10(LPL./HPL))./1.1).^2));

i=i+1;
Knames{i}   = 'K_OH_OH';
LPL         = 6.9E-31.*(T./300).^(-0.8).*M;
HPL         = 2.6E-11;
krx(:,i)    = (LPL./(1+LPL./HPL)).*0.5.^(1./((1+(log10(LPL./HPL))./1.13).^2));

i=i+1;
Knames{i}   = 'K_OH_CO';
LPL         = 5.9E-33.*((T./300).^-1.4).*M;
HPL         = 1.1E-12.*((T./300).^1.3) ;
K_OH_COa    = (LPL./(1+LPL./HPL)).*0.6.^(1./(1+(log10(LPL./HPL)).^2));
LPL         = 1.5E-13.*((T./300).^0.6);
HPL         = 2.1E9.*((T./300).^6.1);
K_OH_COb    = (LPL./(1+LPL./(HPL./M))).*0.6.^(1./(1+(log10(LPL./(HPL./M))).^2))
    ;
krx(:,i)    = K_OH_COa + K_OH_COb;

i=i+1;
Knames{i}   = 'K_NO3_NO2';
LPL         = 3.60E-30.*(T./300).^(-4.1).*M;
HPL         = 1.90E-12.*(T./300).^(0.2);
krx(:,i)    = (LPL./(1+LPL./HPL)).*0.35.^(1./(1+((log10(LPL./HPL))./1.33).^2));

i=i+1;
Knames{i}   = 'K_N2O5';
LPL         = 1.30E-03.*(T./300).^(-3.5).*exp(-11000./T).*M;
HPL         = 9.70E14.*(T./300).^(0.1).*exp(-11080./T);
krx(:,i)    = (LPL./(1+LPL./HPL)).*0.35.^(1./(1+((log10(LPL./HPL))./1.33).^2));

i=i+1;
```

```
Knames{i}   = 'K_HO2_NO2';
LPL         = 1.8E-31.*(T./300).^(-3.2).*M;
HPL         = 4.7E-12;
krx(:,i)    = (LPL./(1+LPL./HPL)).*0.6.^(1./(1+(log10(LPL./HPL)).^2)) ;

i=i+1;
Knames{i}   = 'K_PNA';
LPL         = 4.1E-05.*exp(-10650./T).*M;
HPL         = 4.8E15.*exp(-11170./T);
krx(:,i)    = (LPL./(1+LPL./HPL)).*0.6.^(1./(1+(log10(LPL./HPL)).^2)) ;

i=i+1;
Knames{i}   = 'K_C2O3_NO2';
LPL         = (2.70E-28.*(T./300).^-7.1).*M;
HPL         = (1.20E-11.*(T./300).^-0.9);
krx(:,i)    = (LPL./(1+LPL./HPL)).*0.3.^(1./(1+((log10(LPL./HPL))./1.41).^2));

i=i+1;
Knames{i}   = 'K_PAN';
LPL         = 4.90E-03*exp(-12100./T).*M;
HPL         = 5.40E16*exp(-13830./T);
krx(:,i)    = (LPL./(1+LPL./HPL)).*0.3.^(1./(1+((log10(LPL./HPL))./1.41).^2));

i=i+1;
Knames{i}   = 'K_CXO3_NO2';
LPL         = 3.00E-28.*(T./300).^(-7.1).*M;
HPL         = 1.33E-11.*(T./300).^(-0.9);
krx(:,i)    = (LPL./(1+LPL./HPL)).*0.3.^(1./(1+(log10(LPL./HPL)).^2));

i=i+1;
Knames{i}   = 'K_PANX';
LPL         = 1.7E-03.*exp(-11280./T).*M;
HPL         = 8.3E16.*exp(-13940./T);
krx(:,i)    = (LPL./(1+LPL./HPL)).*0.3.^(1./(1+(log10(LPL./HPL)).^2));

i=i+1;
Knames{i}   = 'K_OPAN';
LPL         = 4.60E-04*exp(-11280./T).*M;
HPL         = 2.24E16*exp(-13940./T);
krx(:,i)    = (LPL./(1+LPL./HPL)).*0.3.^(1./(1+(log10(LPL./HPL)).^2));

%% accumulate
K = struct;
for i=1:length(Knames)
    K.(Knames{i}) = krx(:,i);
end
```

Appendix C: Treatment of wildland fire plume rise in the CONUS 2013 modeling platform for CAMx

Both the Comprehensive Air Quality Model with Extensions (CAMx) and the Community Multiscale Air Quality (CMAQ) model calculate plume rise and vertical emission injection for point source emissions inline; however, CMAQ applies a distinct algorithm for wildland fires that is not included in CAMx (Emery et al., 2010; Pouliot et al., 2005). Therefore, implementation of wildland fire emissions that were originally prepared for use in CMAQ requires modification of the parameters that are used to calculate plume rise in CAMx.

In both models, and for all point sources, the plume rise calculation is based on a set of equations developed by Briggs (1984, 1975, 1972, 1971, 1969) that are highly dependent on a quantity called buoyancy flux F ($m^4\ s^{-3}$). For traditional point sources, buoyancy flux is computed as a function of several parameters specific to the typical industrial emissions setup, including stack height H_s (m), stack diameter D_s (m), stack temperature T_s (K), and stack exit velocity V_s (m s^{-1}). Both CAMx and CMAQ implement Equation (1) to compute initial buoyancy flux at stack top for industrial point sources (Community Modeling and Analysis System, 2017, 2010; Ramboll Environ, 2018), where g is gravitational acceleration (9.80622 m s^{-2}) and T is ambient temperature at the top of the stack (K):

$$F = \frac{g * V_S * {D_S}^2 * (T_S - T)}{4 * T_S} \quad \text{(C.1)}$$

The buoyancy flux calculation for wildland fires in CMAQ is derived from Equation (1), but computes F instead as a function of heat flux Q (BTU s^{-1}) (Pouliot et al., 2005), as shown in Equation (2):

$$F = 0.0092752 * Q \quad \text{(C.2)}$$

Once computed, buoyancy flux is used directly to calculate plume rise, with the exact relationship depending upon atmospheric stability. The final formulations for plume rise and subsequent emission injection are neither consistent between CAMx and CMAQ, nor between wildland fire and industrial point sources within the CMAQ model framework (Emery et al., 2010; Pouliot et al., 2005).

In order to include emissions from wildland fires in our CAMx simulations, we supply a set of stack parameters that are compatible with Equation (1). To begin, we assume a stack height H_s of 2 m, consistent with the altitude used to estimate leaf temperature for biogenic emissions from BEIS (Bash et al., 2016). We also assume a stack temperature T_s of 40 K above the temperature at the top of the stack, based on observations and numerical simulations in the related literature (Achtemeier et al., 2011; Charland and Clements, 2013; Jenkins et al., 2001; Rio et al., 2010; Seto and Clements, 2011; Trentmann et al., 2006). The number of acres burned, which accompany the wildland fire emissions, are converted to m^2 and subsequently used to compute the stack diameter D_s, assuming a circular burn area A:

$$D_s = \sqrt{\frac{4}{\pi} * A} \quad \text{(C.3)}$$

The stack velocity V_s is then derived through the combination of Equations (1) and (2), with our values substituted for T_s and D_s, and the heat flux Q from the wildland fire emissions:

$$V_S = \frac{4*0.0092752*Q*T_S}{g*{D_S}^2*(T_S-T)} \quad \text{(C.4)}$$

This ensures that the buoyancy flux F computed in our CAMx simulations matches F computed for wildland fire plumes in CMAQ. Plume rise and emission injection are then calculated inline in CAMx, using the formulations standard to the CAMx model framework (Emery et al., 2010).

The resulting plume rise and vertical emissions distribution over wildland fires in CAMx are evaluated by comparison to CMAQ, here considered the more precise representation. For example, the left panel in Fig. C.1 shows the simulated vertical profile of carbon monoxide (CO), a common tracer for biomass burning, averaged across active fire cells throughout the CAMx and CMAQ baseline simulations described in Chapter 4. "Active" fire cells are day-specific and further refined using daily maximum mixing ratios of CO. Based on the shape of the vertical profile, it appears that more wildland fire emissions are injected at higher vertical levels in the CAMx simulation than in CMAQ. Although the same total emissions from wildland fires are expected in both simulations, this treatment results in a reduced average tropospheric column of CO over wildland fires ($1.862 \pm 1.590 \times 10^{18}$ molecules cm^{-2}) compared to CMAQ ($1.991 \pm 2.067 \times 10^{18}$ molecules cm^{-2}). This reduction may be due to elevated OH, a major sink for CO, near the vertical levels where the largest fractions of emissions are injected in CAMx, as shown in the right panel of Fig. C.1. Overall, this plume rise treatment provides a means for including wildland fire emissions in the CONUS 2013 platform for CAMx, though it may add to the uncertainty of simulated mixing ratios. The combined uncertainty of deviations from the baseline CMAQ simulation is discussed in Chapter 4.

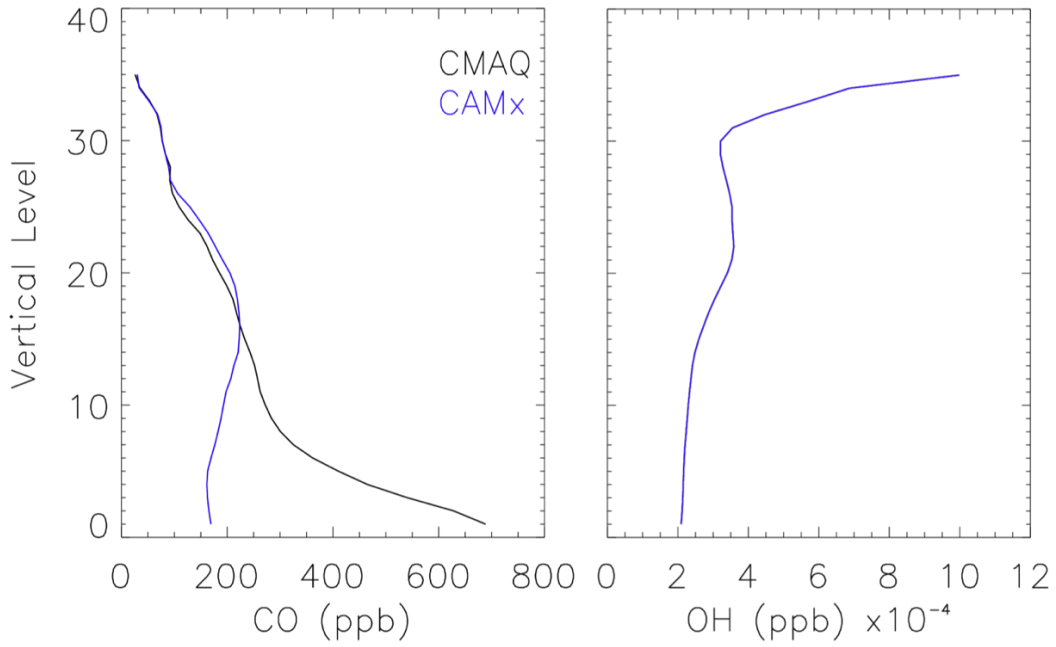

Fig. C.1. Simulated vertical profiles (ppb) of select species, averaged across active fire cells throughout the model domain. "Active" fire cells are day-specific and further refined using daily maximum mixing ratios of CO. The left panel shows the vertical profile of CO obtained from the CMAQ (black) and CAMx (blue) baseline simulations, while the right panel shows the vertical profile of OH from the CAMx baseline simulation only.

Appendix D: Attribution of HCHO production rates to primary source VOCs

To facilitate inter-comparison of different mechanisms, we sort HCHO-producing reactions into broad groups classified by primary source VOC: methane, methanol, isoprene (first- or second-generation), or 'other.' 'Other' accounts for HCHO production from late-generation isoprene oxidation by OH, including PAN degradation, and from multi-generational isoprene oxidation by O_3, $O(^3P)$, and NO_3. For each reaction, simulated production and loss rates are used to identify sources of carbon-containing reactants; major sources of those species are identified, and so on, until the primary source is isolated. Then, reactions are assigned to the primary source VOC identified by this process, and the rates of reactions assigned to the same primary VOC are summed together. Please note, however, that CH_3O_2 has significant sources in both methane oxidation and late-generation isoprene oxidation. Formaldehyde production rates deriving from the reactions of CH_3O_2 are multiplied by the fraction of CH_3O_2 produced via methane oxidation, and the result is attributed to a source of methane; the remaining HCHO production fraction is attributed to 'other.' Table D.1 lists the primary source VOC assignments for the mechanisms in Figs. 3.6 and 3.8b.

Table D.1. Assignment of HCHO-producing reactions to primary source VOCs. Reactions from CB6r2 and CB6r2-UMD are listed in the same column, with those unique to CB6r2-UMD in parentheses. Species names follow the nomenclature adopted by each mechanism.

Source	CB05	CB6r2(-UMD)	GEOS-Chem	MCMv3.2	MCMv3.3.1
CH4 + OH	MEO2 + C2O3[a] MEO2 + CXO3[a] MEO2 + MEO2[a] MEO2 + NO[a] MEPX + hν[a]	MEO2 + C2O3[a] MEO2 + HO2[a] MEO2 + NO[a] MEO2 + RO2[a] MEPX + OH[a]	CH2OO + CH2OO[a] CH2OO + CO[a] CH2OO + NO[a] CH2OO + NO2[a] MO2 + MCO3[a] MO2 + MO2[a] MO2 + NO[a] MO2 + O3[a] MP + hν[a] MP + OH[a] MPN[a]	CH3NO3 + OH[a] CH3O[a] CH3O2 + HO2[a] CH3O2 + RO2[a] CH3OOH + OH[a]	CH3NO3 + OH[a] CH3O[a] CH3O2 + HO2[a] CH3O2 + RO2[a] CH3OOH + OH[a]
CH3OH + OH	MEOH + OH	MEOH + OH	MOH + OH	CH3OH + OH	CH3OH + OH
ISOP + OH (1st Gen)	ISOP + OH	ISO2 + C2O3 ISO2 + HO2 ISO2 + NO ISO2 + RO2	RIO2 + HO2 RIO2 + MCO3 RIO2 + MO2 RIO2 + NO RIO2 + RIO2	C524O ISOPBO ISOPDO	C524O C524O2 ISOP34O ISOPBO ISOPBO2 ISOPDO ISOPDO2
ISOP + OH (2nd Gen)	ISPD + hν ISPD + NO3 ISPD + O3 ISPD + OH NTR + hν NTR + OH	(HPLD + hν) INTR + OH ISPD + hν ISPD + O3 (ISPD + OH)	A3O2 + MO2 B3O2 + MO2 HPALD + hν HPALD + OH ISOPNB + O3 ISOPNBO2 + HO2	CH3C2H2O2 HMACO3 + HO2 HMACO3 + NO HMACO3 + NO3 HMACO3 + RO2 HMACR + O3	C51O C530NO3 + OH C530O C531O C536OOH + hν C537OOH + hν

			ISOPNBO2 + NO	HMVKAO	CH3C2H2O2
			MACR + hν	INDO	DHPMEK + hν
			MACR + O3	ISOPBNO3 + O3	DHPMPAL + hν
			MAN2 + HO2	ISOPDNO3 + O3	HMACO3 + HO2
			MAN2 + MCO3	MACR + O3	HMACO3 + NO
			MAN2 + MO2	MACROHO	HMACO3 + NO3
			MAN2 + NO	MGLOOA	HMACO3 + RO2
			MAO3 + HO2	MVK + hν	HMACR + O3
			MAO3 + MCO3	MVK + O3	HMVKAO
			MAO3 + MO2	NC524O	INDO
			MAO3 + NO		ISOP34NO3 + O3
			MGLOOA		ISOPBNO3 + O3
			MRO2 + MCO3		ISOPDNO3 + O3
			MRO2 + MO2		MACR + O3
			MRO2 + NO		MACROHO
			MVK + hν		ME3BU3ECHO + O3
			MVK + O3		MGLOOA
			R4O2 + MO2		MVK + hν
			RIP + hν		MVK + O3
			VRO2 + HO2		NC51O
			VRO2 + MCO3		NC524O
			VRO2 + MO2		NC526O
			VRO2 + NO		PE4E2CO + O3
Other	ISOP + O3	ACET + OH	ALD2 + OH	ACETOL + hν	ACETOL + hν
	ISOP + O3P	EPX2 + C2O3	ATO2 + HO2	ACO2H + OH	ACO2H + OH
	MEO2 + C2O3[b]	EPX2 + HO2	ATO2 + MCO3	ACO3 + HO2	ACO3 + HO2
	MEO2 + CXO3[b]	EPX2 + NO	ATO2 + MO2	ACO3 + NO	ACO3 + NO
	MEO2 + MEO2[b]	EPX2 + RO2	ATO2 + NO	ACO3 + NO3	ACO3 + NO3
	MEO2 + NO[b]	GLYD + hν	ATOOH + hν	ACO3 + RO2	ACO3 + RO2
	MEPX + hν[b]	(GLYD + OH)	CH2OO + CH2OO[b]	ACO3H + hν	ACO3H + hν

		IOLE + O3	CH2OO + CO[b]	ACR + hν	ACR + hν
		ISOP + NO3	CH2OO + NO[b]	ACR + O3	ACR + O3
		ISOP + O3	CH2OO + NO2[b]	BIACETO	BIACETO
		ISOP + O3P	ETHLN + hν	C2H4 + O3	C2H4 + O3
		MEO2 + C2O3[b]	ETHLN + OH	C3DIOLO	C3DIOLO
		MEO2 + HO2[b]	ETO2 + MO2	C3H6 + O3	C3H6 + O3
		MEO2 + NO[b]	GAOOB	C524CO + hν	C524CO + hν
		MEO2 + RO2[b]	GLYC + hν	C5H8 + O3	C5H8 + O3
		MEPX + OH[b]	GLYC + OH	CH2OO	CH2OO
		OLE + NO3	GLYX + hν	CH2OO + CO	CH2OO + CO
		OLE + O3	HAC + hν	CH2OO + NO	CH2OO + NO
		OLE + O3P	HC187 + OH	CH2OO + NO2	CH2OO + NO2
		OLE + OH	HC5OO + MO2	CH3COCH2O	CH3COCH2O
			IEPOXOO + HO2	CH3COPAN + OH	CH3COPAN + OH
			IEPOXOO + NO	CH3NO3 + OH[b]	CH3NO3 + OH[b]
			INO2 + INO2	CH3O[b]	CH3O[b]
			INO2 + MCO3	CH3O2 + HO2[b]	CH3O2 + HO2[b]
			INO2 + MO2	CH3O2 + RO2[b]	CH3O2 + RO2[b]
			INO2 + NO	CH3OOH + OH[b]	CH3OOH + OH[b]
			INO2 + NO3	CO23C4NO3 + hν	CO2C3CHO + hν
			ISN1 + hν	ETHENO3O	ETHENO3O
			ISN1 + O3	GAOOB	GLYOOB
			ISNOHOO + MO2	GLYOOB	GLYOX + hν
			ISNOOB + MO2	GLYOX + hν	H13CO2C3 + hν
			ISOP + O3	H13CO2C3 + hν	HCOC5 + hν
			ISOPNDO2 + HO2	HCOC5 + hν	HCOCH2O
			ISOPNDO2 + NO	HCOCH2O	HCOCH2OOH + hν
			KO2 + MO2	HCOCH2OOH + hν	HMACO2H + OH
			MACRN + hν	HMACO2H + OH	HMACO3H + hν
			MACRNO2 + HO2	HMACO3H + hν	HOCH2CH2O

		MACRNO2 + NO	HMPAN + OH	HOCH2CHO + hν
		MACROOA	HOCH2CH2O	HOCH2CO2H + OH
		MAOP + hν	HOCH2CHO + hν	HOCH2CO3 + HO2
		MAOPO2 + MO2	HOCH2CO2H + OH	HOCH2CO3 + NO
		MCO3 + PO2	HOCH2CO3 + HO2	HOCH2CO3 + NO3
		MO2 + MCO3[b]	HOCH2CO3 + NO	HOCH2CO3 + RO2
		MO2 + MO2[b]	HOCH2CO3 + NO3	HOCH2CO3H + hν
		MO2 + NO[b]	HOCH2CO3 + RO2	HYPERACET + hν
		MO2 + O3[b]	HOCH2CO3H + hν	HYPROPO
		MP + hν[b]	HYPERACET + hν	INANO3 + OH
		MP + OH[b]	HYPROPO	IPROPOLO
		MPN[b]	IEC1O	MACROOA
		MRP + hν	INANO3 + OH	MC3CODBPAN + OH
		MVKN + OH	IPROPOLO	MCOCOMOOOH + hν
		MVKOOA	MACROOA	MCOCOMOXO
		NC2OO	MPAN + O3	MPAN + O3
		PMN	MVKO	MVKO
		PMN + O3	MVKOH + hν	MVKOH + hν
		PMN + OH	MVKOH + O3	MVKOH + O3
		PO2 + MO2	MVKOHAO	MVKOHAO
		PO2 + NO	MVKOOA	MVKOOA
		PP + hν	MVKOOH + hν	MVKOOH + hν
		PRN1 + MCO3	NMGLYOX + hν	NMGLYOX + hν
		PRN1 + MO2	NO3CH2CHO + hν	NO3CH2CO2H + OH
		PRN1 + NO	NO3CH2CO2H +	NO3CH2CO3 + HO2
		PROPNN + hν	OH	NO3CH2CO3 + NO
		PRPE + O3	NO3CH2CO3 + HO2	NO3CH2CO3 + NO3
		R4N1 + MCO3	NO3CH2CO3 + NO	NO3CH2CO3 + RO2
		R4N1 + MO2	NO3CH2CO3 + NO3	NO3CH2CO3H + hν
		R4N1 + NO	NO3CH2CO3 +RO2	NO3CH2PAN + OH

		RCO3 + MO2 VRP + hν	NO3CH2CO3H + hν NO3CH2PAN + OH NOA + hν OCCOHCO PAN + OH PHAN + OH PRONO3AO PRONO3BO	OCCOHCO PAN + OH PHAN + OH PRONO3AO PRONO3BO

[a] Corresponding HCHO production rates are multiplied by the fraction of CH_3O_2 produced via methane oxidation.
[b] Corresponding HCHO production rates are the remainder after subtraction of the methane contribution.

Appendix E: Model kinetic uncertainty

Uncertainties related to model kinetics are determined for CB6r2-UMD. Analysis is carried out on a subset of modeled data points from SENEX. This subset contains every 100th point, selected after sorting by NO_x in order to preserve the NO_x distribution of the full dataset. The subset is subjected to sensitivity simulations, in which reaction rates are perturbed one at a time by a constant multiplicative uncertainty factor. Responses in HCHO are averaged across the subset to determine which reactions have the largest influence on modeled HCHO. The reactions that, when their corresponding rates are perturbed by a constant factor of 2, vary modeled HCHO mixing ratios by 3% or more are listed in Table E.1.

The same simulations are then re-run using literature rate constant uncertainty estimates. Rate constants in CB6r2, and therefore CB6r2-UMD, are mainly supplied by the IUPAC kinetic data evaluation (Hildebrandt Ruiz and Yarwood, 2013). For each reaction, IUPAC provides 2σ reliability estimates for the rate constant at 298 K (Δlog k(298)) and its variability over a wide range of temperatures ($\Delta E/R$) (Atkinson et al., 2006). A temperature-dependent multiplicative uncertainty factor f for the rate constant k (cm^3 molecule^{-1} s^{-1}) is obtained using the following relationships, where T is temperature (K):

$$\Delta \log k(T) = \Delta \log k(298) + 0.4343 \left\{ \Delta E/R \left(\frac{1}{T} - \frac{1}{298} \right) \right\} \quad \text{(E.1)}$$

$$f = 10^{\Delta \log k(T)} \quad \text{(E.2)}$$

The upper and lower uncertainty limits of the rate constant are determined by multiplying or dividing the rate constant by *f*, respectively. The 1σ value of a given *f* is the square root of the 2σ value.

Since uncertainty estimates are not available for all rate constants, literature values are used only for the reactions identified in Table E.1. Photolytic reactions listed in the table are assigned a 2σ uncertainty estimate of 10% (1σ is ~5%), based on the reported accuracy of constrained J-values (Table 3.2). A factor of 2, recommended by IUPAC as a minimum uncertainty estimate for unverified rate constants, is used to represent the 1σ and 2σ uncertainty limits for all other reactions. Rate constants are perturbed one at a time to their uncertainty limits; average responses in modeled HCHO mixing ratios are reported for the reactions in Table E.1. For each point in the subset, the fractional changes in modeled HCHO from individual perturbations are combined in quadrature. We average these values across the subset and thus derive for CB6r2-UMD kinetics a 1σ uncertainty estimate of ~12% (2σ is ~20%) in modeled HCHO mixing ratios. This procedure is too computationally expensive to repeat for the other mechanisms considered in this work, but because the other mechanisms use similar rate constants for the reactions in Table E.1, we expect them to yield similar results.

Table E.1. Reactions in CB6r2-UMD that most influence modeled HCHO. The parameter ΔHCHO is the average effect on modeled HCHO mixing ratios when each rate constant is perturbed to its 1σ or 2σ uncertainty limits. Results are representative of the subset of SENEX data points selected for uncertainty analysis.

Reaction No.	Reaction	1σ ΔHCHO (%)	2σ ΔHCHO (%)
55	PAN = NO2 + C2O3	4.90	10.50
96	FORM + OH = HO2 + CO	3.53	7.05
54	C2O3 + NO2 = PAN	2.86	5.67
3	O3 + NO = NO2	2.13	4.24
11	O1D + H2O = 2 OH	2.09	4.18
10	O1D + M = O + M	2.09	4.18
149	ISOP + OH = ISO2 + RO2	1.97	3.94
1	NO2 + hν = NO + O	1.81	3.61
98	FORM + hν = CO + H2	1.55	3.09
25	HO2 + NO = OH + NO2	1.38	2.75
53	C2O3 + NO = NO2 + MEO2 + RO2	1.33	2.65
124	CH4 + OH = MEO2 + RO2	1.03	2.05
9	O3 + hν = O1D	0.97	1.94
97	FORM + hν = 2 HO2 + CO	0.83	1.66
123	CO + OH = HO2	0.72	1.44
126	MEOH + OH = FORM + HO2	0.65	1.31

Bibliography

Achtemeier, G.L., Goodrick, S.A., Liu, Y., 2011. Modeling multiple-core updraft plume rise for an aerial ignition prescribed burn by coupling daysmoke with a cellular automata fire model. Atmosphere. 3, 352–376. https://doi.org/10.3390/atmos3030352

Allen, D.J., Pickering, K.E., Pinder, R.W., Henderson, B.H., Appel, K.W., Prados, A., 2012. Impact of lightning-NO on eastern United States photochemistry during the summer of 2006 as determined using the CMAQ model. Atmos. Chem. Phys. 12, 1737–1758. https://doi.org/10.5194/acp-12-1737-2012

Anderson, D.C., Loughner, C.P., Diskin, G., Weinheimer, A., Canty, T.P., Salawitch, R.J., Worden, H.M., Fried, A., Mikoviny, T., Wisthaler, A., Dickerson, R.R., 2014. Measured and modeled CO and NOy in DISCOVER-AQ: An evaluation of emissions and chemistry over the eastern US. Atmos. Environ. 96, 78–87. https://doi.org/10.1016/j.atmosenv.2014.07.004

Anderson, D.C., Nicely, J.M., Salawitch, R.J., Canty, T.P., Dickerson, R.R., Hanisco, T.F., Wolfe, G.M., Apel, E.C., Atlas, E., Bannan, T., Bauguitte, S., Blake, N.J., Bresch, J.F., Campos, T.L., Carpenter, L.J., Cohen, M.D., Evans, M., Fernandez, R.P., Kahn, B.H., Kinnison, D.E., Hall, S.R., Harris, N.R.P., Hornbrook, R.S., Lamarque, J.-F., Le Breton, M., Lee, J.D., Percival, C., Pfister, L., Pierce, R.B., Riemer, D.D., Saiz-Lopez, A., Stunder, B.J.B., Thompson, A.M., Ullmann, K., Vaughan, A., Weinheimer, A.J., 2016. A pervasive role for biomass burning in tropical high ozone/low water structures. Nat. Commun. 7, 10267.

Archibald, A.T., Cooke, M.C., Utembe, S.R., Shallcross, D.E., Derwent, R.G., Jenkin, M.E., 2010a. Impacts of mechanistic changes on HOx formation and recycling in the oxidation of isoprene. Atmos. Chem. Phys. 10, 8097–8118. https://doi.org/10.5194/acp-10-8097-2010

Archibald, A.T., Jenkin, M.E., Shallcross, D.E., 2010b. An isoprene mechanism intercomparison. Atmos. Environ. 44, 5356–5364. https://doi.org/10.1016/j.atmosenv.2009.09.016

Atkinson, R., Baulch, D.L., Cox, R.A., Crowley, J.N., Hampson, R.F., Hynes, R.G., Jenkin, M.E., Rossi, M.J., Troe, J., Subcommittee, I., 2006. Evaluated kinetic and photochemical data for atmospheric chemistry: Volume II - Gas phase reactions of organic species. Atmos. Chem. Phys. 6, 3625–4055. https://doi.org/10.5194/acp-6-3625-2006

Baeza-Romero, M.T., Glowacki, D.R., Blitz, M.A., Heard, D.E., Pilling, M.J., Rickard, A.R., Seakins, P.W., 2007. A combined experimental and theoretical study of the reaction between methylglyoxal and OH/OD radical: OH regeneration. Phys. Chem. Chem. Phys. 9, 4114–4128. https://doi.org/10.1039/b702916k

Baier, B.C., Brune, W.H., Miller, D.O., Blake, D., Long, R., Wisthaler, A., Cantrell, C., Fried, A., Heikes, B., Brown, S., McDuffie, E., Flocke, F., Apel, E., Kaser, L., Weinheimer, A., 2017. Higher measured than modeled ozone production at increased NOx levels in the Colorado Front Range. Atmos. Chem. Phys. 17, 11273–11292.

Banks, R.F., Baldasano, J.M., 2016. Impact of WRF model PBL schemes on air quality simulations over Catalonia, Spain. Sci. Total Environ. 572, 98–113. https://doi.org/https://doi.org/10.1016/j.scitotenv.2016.07.167
Banks, R.F., Tiana-Alsina, J., Baldasano, J.M., Rocadenbosch, F., Papayannis, A., Solomos, S., Tzanis, C.G., 2016. Sensitivity of boundary-layer variables to PBL schemes in the WRF model based on surface meteorological observations, lidar, and radiosondes during the HygrA-CD campaign. Atmos. Res. 176–177, 185–201. https://doi.org/https://doi.org/10.1016/j.atmosres.2016.02.024
Bash, J.O., Baker, K.R., Beaver, M.R., 2016. Evaluation of improved land use and canopy representation in BEIS v3.61 with biogenic VOC measurements in California. Geosci. Model Dev. 9, 2191–2207. https://doi.org/10.5194/gmd-9-2191-2016
Bates, K.H., Crounse, J.D., St Clair, J.M., Bennett, N.B., Nguyen, T.B., Seinfeld, J.H., Stoltz, B.M., Wennberg, P.O., 2014. Gas phase production and loss of isoprene epoxydiols. J. Phys. Chem. A. 118, 1237–1246. https://doi.org/10.1021/jp4107958
Benish, S., Dickerson, R.R., Ren, X., He, H., Li, Z., 2019. Observations of nitrogen oxides and volatile organic compounds over Hebei, China and impact on ozone formation (in preparation).
Briggs, G.A., 1984. Plume rise and buoyancy effects. Oak Ridge, TN.
Briggs, G.A., 1975. Plume rise predictions, in: Lectures on Air Pollution and Environmental Impact Analyses. Boston, MA, pp. 59–111.
Briggs, G.A., 1972. Chimney plumes in neutral and stable surroundings. Atmos. Environ. 6, 507–510.
Briggs, G.A., 1971. Some recent analyses of plume rise observation, in: Englund, H.M., Beery, W.T. (Eds.), Proceeding of the Second International Clean Air Congress. Academic Press, New York, pp. 1029–1032.
Briggs, G.A., 1969. Plume Rise. USAEC Critical Review Series, Springfield, VA.
Busilacchio, M., Di Carlo, P., Aruffo, E., Biancofiore, F., Dari Salisburgo, C., Giammaria, F., Bauguitte, S., Lee, J., Moller, S., Hopkins, J., Punjabi, S., Andrews, S., Lewis, A.C., Parrington, M., Palmer, P.I., Hyer, E., Wolfe, G.M., 2016. Production of peroxy nitrates in boreal biomass burning plumes over Canada during the BORTAS campaign. Atmos. Chem. Phys. 16, 3485–3497.
Butkovskaya, N.I., Pouvesle, N., Kukui, A., Mu, Y., Le Bras, G., 2006. Mechanism of the OH-initiated oxidation of hydroxyacetone over the temperature range 236−298 K. J. Phys. Chem. A. 110, 6833–6843. https://doi.org/10.1021/jp056345r
Canty, T.P., Hembeck, L., Vinciguerra, T.P., Anderson, D.C., Goldberg, D.L., Carpenter, S.F., Allen, D.J., Loughner, C.P., Salawitch, R.J., Dickerson, R.R., 2015. Ozone and NOx chemistry in the eastern US: Evaluation of CMAQ/CB05 with satellite (OMI) data. Atmos. Chem. Phys. 15, 10965–10982. https://doi.org/10.5194/acp-15-10965-2015
Carlton, A.G., Baker, K.R., 2011. Photochemical modeling of the Ozark isoprene volcano: MEGAN, BEIS, and their impacts on air quality predictions. Environ. Sci. Technol. 45, 4438–4445. https://doi.org/10.1021/es200050x

Carter, W.P.L., 2010. Development of a condensed SAPRC-07 chemical mechanism. Atmos. Environ. 44, 5336–5345. https://doi.org/https://doi.org/10.1016/j.atmosenv.2010.01.024

Cazorla, M., Wolfe, G.M., Bailey, S.A., Swanson, A.K., Arkinson, H.L., Hanisco, T.F., 2015. A new airborne laser-induced fluorescence instrument for in situ detection of formaldehyde throughout the troposphere and lower stratosphere. Atmos. Meas. Tech. 8, 541–552. https://doi.org/10.5194/amt-8-541-2015

Charland, A.M., Clements, C.B., 2013. Kinematic structure of a wildland fire plume observed by Doppler lidar. J. Geophys. Res. Atmos. 118, 3200–3212. https://doi.org/10.1002/jgrd.50308

Community Modeling and Analysis System, 2017. SMOKE v4.5 User's Manual. Chapel Hill, NC.

Community Modeling and Analysis System, 2010. Operational Guidance for the Community Multiscale Air Quality (CMAQ) Modeling System. Chapel Hill, NC.

Crounse, J.D., Paulot, F., Kjaergaard, H.G., Wennberg, P.O., 2011. Peroxy radical isomerization in the oxidation of isoprene. Phys. Chem. Chem. Phys. 13, 13607–13613. https://doi.org/10.1039/C1CP21330J

Crutzen, P., 1973. A discussion of the chemistry of some minor constituents in the stratosphere and troposphere. Pure Appl. Geophys. 106, 1385–1399. https://doi.org/10.1007/BF00881092

Da Silva, G., Graham, C., Wang, Z.-F., 2010. Unimolecular β-hydroxyperoxy radical decomposition with OH recycling in the photochemical oxidation of isoprene. Environ. Sci. Technol. 44, 250–256. https://doi.org/10.1021/es900924d

de Gouw, J., Warneke, C., 2007. Measurements of volatile organic compounds in the earth's atmosphere using proton-transfer-reaction mass spectrometry. Mass Spectrom. Rev. 26, 223–257. https://doi.org/10.1002/mas.20119

De Smedt, I., Stavrakou, T., Hendrick, F., Danckaert, T., Vlemmix, T., Pinardi, G., Theys, N., Lerot, C., Gielen, C., Vigouroux, C., Hermans, C., Fayt, C., Veefkind, P., Müller, J.F., Van Roozendael, M., 2015. Diurnal, seasonal and long-term variations of global formaldehyde columns inferred from combined OMI and GOME-2 observations. Atmos. Chem. Phys. 15, 12519–12545. https://doi.org/10.5194/acp-15-12519-2015

Donner, L.J., Wyman, B.L., Hemler, R.S., Horowitz, L.W., Ming, Y., Zhao, M., Golaz, J.-C., Ginoux, P., Lin, S.-J., Schwarzkopf, M.D., Austin, J., Alaka, G., Cooke, W.F., Delworth, T.L., Freidenreich, S.M., Gordon, C.T., Griffies, S.M., Held, I.M., Hurlin, W.J., Klein, S.A., Knutson, T.R., Langenhorst, A.R., Lee, H.-C., Lin, Y., Magi, B.I., Malyshev, S.L., Milly, P.C.D., Naik, V., Nath, M.J., Pincus, R., Ploshay, J.J., Ramaswamy, V., Seman, C.J., Shevliakova, E., Sirutis, J.J., Stern, W.F., Stouffer, R.J., Wilson, R.J., Winton, M., Wittenberg, A.T., Zeng, F., 2011. The dynamical core, physical parameterizations, and basic simulation characteristics of the atmospheric component AM3 of the GFDL global coupled model CM3. J. Clim. 24, 3484–3519. https://doi.org/10.1175/2011jcli3955.1

Emery, C., Jung, J., Bonyoung, K., Yarwood, G., 2015. Improvements to CAMx snow cover treatments and Carbon Bond chemical mechanism for winter ozone. Novato, CA.

Emery, C., Jung, J., Downey, N., Johnson, J., Jimenez, M., Yarwood, G., Morris, R., 2012. Regional and global modeling estimates of policy relevant background ozone over the United States. Atmos. Environ. 47, 206–217. https://doi.org/https://doi.org/10.1016/j.atmosenv.2011.11.012

Emery, C., Jung, J., Yarwood, G., 2010. Implementation of an alternative plume rise methodology in CAMx. Novato, CA.

Emery, C., Liu, Z., Koo, B., Yarwood, G., 2016. Improved halogen chemistry for CAMx modeling. Novato, CA.

EPA, 2015a. 2011 National Emissions Inventory Version 2 Technical Support Document. Research Triangle Park, NC.

EPA, 2015b. MOVES2014a User Guide.

EPA, 2013. Integrated Science Assessment of Ozone and Related Photochemical Oxidants. Washington, DC.

Farkas, C.M., Moeller, M.D., Felder, F.A., Baker, K.R., Rodgers, M., Carlton, A.G., 2015. Temporalization of peak electric generation particulate matter emissions during high energy demand days. Environ. Sci. Technol. 49, 4696–4704. https://doi.org/10.1021/es5050248

Fischer, E. V, Jacob, D.J., Yantosca, R.M., Sulprizio, M.P., Millet, D.B., Mao, J., Paulot, F., Singh, H.B., Roiger, A., Ries, L., Talbot, R.W., Dzepina, K., Pandey Deolal, S., 2014. Atmospheric peroxyacetyl nitrate (PAN): a global budget and source attribution. Atmos. Chem. Phys. 14, 2679–2698. https://doi.org/10.5194/acp-14-2679-2014

Fisher, J.A., Jacob, D.J., Travis, K.R., Kim, P.S., Marais, E.A., Chan Miller, C., Yu, K., Zhu, L., Yantosca, R.M., Sulprizio, M.P., Mao, J., Wennberg, P.O., Crounse, J.D., Teng, A.P., Nguyen, T.B., St. Clair, J.M., Cohen, R.C., Romer, P., Nault, B.A., Wooldridge, P.J., Jimenez, J.L., Campuzano-Jost, P., Day, D.A., Hu, W., Shepson, P.B., Xiong, F., Blake, D.R., Goldstein, A.H., Misztal, P.K., Hanisco, T.F., Wolfe, G.M., Ryerson, T.B., Wisthaler, A., Mikoviny, T., 2016. Organic nitrate chemistry and its implications for nitrogen budgets in an isoprene- and monoterpene-rich atmosphere: Constraints from aircraft (SEAC4RS) and ground-based (SOAS) observations in the Southeast US. Atmos. Chem. Phys. 16, 5969–5991. https://doi.org/10.5194/acp-16-5969-2016

Foley, K.M., Roselle, S.J., Appel, K.W., Bhave, P. V, Pleim, J.E., Otte, T.L., Mathur, R., Sarwar, G., Young, J.O., Gilliam, R.C., Nolte, C.G., Kelly, J.T., Gilliland, A.B., Bash, J.O., 2010. Incremental testing of the Community Multiscale Air Quality (CMAQ) modeling system version 4.7. Geosci. Model Dev. 3, 205–226.

Foroutan, H., Young, J., Napelenok, S., Ran, L., Appel K, W., Gilliam R, C., Pleim J, E., 2017. Development and evaluation of a physics-based windblown dust emission scheme implemented in the CMAQ modeling system. J. Adv. Model. Earth Syst. 9, 585–608. https://doi.org/10.1002/2016MS000823

Gilman, J.B., Kuster, W.C., Goldan, P.D., Herndon, S.C., Zahniser, M.S., Tucker, S.C., Brewer, W.A., Lerner, B.M., Williams, E.J., Harley, R.A., Fehsenfeld, F.C., Warneke, C., de Gouw, J.A., 2009. Measurements of volatile organic compounds during the 2006 TexAQS/GoMACCS campaign: Industrial influences, regional characteristics, and diurnal dependencies of the OH reactivity. J. Geophys. Res. Atmos. 114, D00F06. https://doi.org/10.1029/2008JD011525

Goldberg, D.L., 2015. Lifetime and Distribution of Ozone and Related Pollutants in the Eastern United States. University of Maryland, College Park, MD.
Goldberg, D.L., Vinciguerra, T.P., Anderson, D.C., Hembeck, L., Canty, T.P., Ehrman, S.H., Martins, D.K., Stauffer, R.M., Thompson, A.M., Salawitch, R.J., Dickerson, R.R., 2016. CAMx ozone source attribution in the eastern United States using guidance from observations during DISCOVER-AQ Maryland. Geophys. Res. Lett. 43, 2249–2258. https://doi.org/10.1002/2015GL067332
Goldberg, D.L., Vinciguerra, T.P., Hosley, K.M., Loughner, C.P., Canty, T.P., Salawitch, R.J., Dickerson, R.R., 2015. Evidence for an increase in the ozone photochemical lifetime in the eastern United States using a regional air quality model. J. Geophys. Res. Atmos. 120, 12778–12793. https://doi.org/10.1002/2015JD023930
Goliff, W.S., Stockwell, W.R., Lawson, C. V, 2013. The Regional Atmospheric Chemistry Mechanism, version 2. Atmos. Environ. 68, 174–185. https://doi.org/10.1016/j.atmosenv.2012.11.038
González Abad, G., Liu, X., Chance, K., Wang, H., Kurosu, T.P., Suleiman, R., 2015. Updated Smithsonian Astrophysical Observatory Ozone Monitoring Instrument (SAO OMI) formaldehyde retrieval. Atmos. Meas. Tech. 8, 19–32. https://doi.org/10.5194/amt-8-19-2015
Guenther, A.B., Jiang, X., Heald, C.L., Sakulyanontvittaya, T., Duhl, T., Emmons, L.K., Wang, X., 2012. The Model of Emissions of Gases and Aerosols from Nature version 2.1 (MEGAN2.1): An extended and updated framework for modeling biogenic emissions. Geosci. Model Dev. 5, 1471–1492. https://doi.org/10.5194/gmd-5-1471-2012
Hembeck, L., He, H., Vinciguerra, T.P., Canty, T.P., Dickerson, R.R., Salawitch, R.J., Loughner, C.P., 2019. Measured and modeled ozone photochemical production in the Baltimore-Washington Airshed (in preparation).
Henderson, B.H., Akhtar, F., Pye, H.O.T., Napelenok, S.L., Hutzell, W.T., 2014. A database and tool for boundary conditions for regional air quality modeling: description and evaluation. Geosci. Model Dev. 7, 339–360. https://doi.org/10.5194/gmd-7-339-2014
Hildebrandt Ruiz, L., Yarwood, G., 2013. Interactions between organic aerosol and NOy: Influence on oxidant production. Novato, CA.
Hogrefe, C., Hao, W., Zalewsky, E.E., Ku, J.-Y., Lynn, B., Rosenzweig, C., Schultz, M.G., Rast, S., Newchurch, M.J., Wang, L., Kinney, P.L., Sistla, G., 2011. An analysis of long-term regional-scale ozone simulations over the Northeastern United States: Variability and trends. Atmos. Chem. Phys. 11, 567–582. https://doi.org/10.5194/acp-11-567-2011
Huszar, P., Belda, M., Karlický, J., Bardachova, T., Halenka, T., Pisoft, P., 2018. Impact of urban canopy meteorological forcing on aerosol concentrations. Atmos. Chem. Phys. 18, 14059–14078. https://doi.org/10.5194/acp-18-14059-2018
Hutzell, W.T., Luecken, D.J., Appel, K.W., Carter, W.P.L., 2012. Interpreting predictions from the SAPRC07 mechanism based on regional and continental simulations. Atmos. Environ. 46, 417–429. https://doi.org/https://doi.org/10.1016/j.atmosenv.2011.09.030

IPCC, 2013. Climate Change 2013: The Physical Science Basis. Contribution of Working Group I to the Fifth Assessment Report of the Intergovernmental Panel on Climate Change. Cambridge University Press, Cambridge, United Kingdom and New York, NY, USA. https://doi.org/10.1017/CBO9781107415324

Jacob, D.J., 1999. Introduction to Atmospheric Chemistry. Princeton University Press, Princeton.

Jenkin, M.E., Saunders, S.M., Pilling, M.J., 1997. The tropospheric degradation of volatile organic compounds: a protocol for mechanism development. Atmos. Environ. 31, 81–104.

Jenkin, M.E., Young, J.C., Rickard, A.R., 2015. The MCM v3.3.1 degradation scheme for isoprene. Atmos. Chem. Phys. 15, 11433–11459. https://doi.org/10.5194/acp-15-11433-2015

Jenkins, M., Clark, T., Coen, J., 2001. Coupling atmospheric and fire models, in: Johnson, E., Miyanishi, K. (Eds.), Forest Fires: Behavior and Ecological Effects. Academic Press, San Diego, CA, USA, pp. 258–301.

Kaiser, J., Jacob, D.J., Zhu, L., Travis, K.R., Fisher, J.A., González Abad, G., Zhang, L., Zhang, X., Fried, A., Crounse, J.D., St. Clair, J.M., Wisthaler, A., 2018. High-resolution inversion of OMI formaldehyde columns to quantify isoprene emission on ecosystem-relevant scales: Application to the southeast US. Atmos. Chem. Phys. 18, 5483–5497. https://doi.org/https://doi.org/10.5194/acp-18-5483-2018

Kaiser, J., Wolfe, G.M., Min, K.E., Brown, S.S., Miller, C.C., Jacob, D.J., deGouw, J.A., Graus, M., Hanisco, T.F., Holloway, J., Peischl, J., Pollack, I.B., Ryerson, T.B., Warneke, C., Washenfelder, R.A., Keutsch, F.N., Washenfelder, R.A., Keutsch, F.N., 2015. Reassessing the ratio of glyoxal to formaldehyde as an indicator of hydrocarbon precursor speciation. Atmos. Chem. Phys. 15, 7571–7583. https://doi.org/10.5194/acp-15-7571-2015

Kim, P.S., Jacob, D.J., Fisher, J.A., Travis, K., Yu, K., Zhu, L., Yantosca, R.M., Sulprizio, M.P., Jimenez, J.L., Campuzano-Jost, P., Froyd, K.D., Liao, J., Hair, J.W., Fenn, M.A., Butler, C.F., Wagner, N.L., Gordon, T.D., Welti, A., Wennberg, P.O., Crounse, J.D., St. Clair, J.M., Teng, A.P., Millet, D.B., Schwarz, J.P., Markovic, M.Z., Perring, A.E., 2015. Sources, seasonality, and trends of southeast US aerosol: An integrated analysis of surface, aircraft, and satellite observations with the GEOS-Chem chemical transport model. Atmos. Chem. Phys. 15, 10411–10433. https://doi.org/10.5194/acp-15-10411-2015

Kumar, V., Chandra, B.P., Sinha, V., 2018. Large unexplained suite of chemically reactive compounds present in ambient air due to biomass fires. Sci. Rep. 8, 626. https://doi.org/10.1038/s41598-017-19139-3

Lafranchi, B.W., Wolfe, G.M., Thornton, J.A., Harrold, S.A., Browne, E.C., Min, K.E., Wooldridge, P.J., Gilman, J.B., Kuster, W.C., Goldan, P.D., De Gouw, J.A., Mckay, M., Goldstein, A.H., Ren, X., Mao, J., Cohen, R.C., 2009. Closing the peroxy acetyl nitrate budget: Observations of acyl peroxy nitrates (PAN, PPN, and MPAN) during BEARPEX 2007. Atmos. Chem. Phys. 9, 7623–7641.

Lee, L., Teng, A.P., Wennberg, P.O., Crounse, J.D., Cohen, R.C., 2014. On rates and mechanisms of OH and O3 reactions with isoprene-derived hydroxy nitrates. J. Phys. Chem. A. 118, 1622–1637. https://doi.org/10.1021/jp4107603

Lerner, B.M., Gilman, J.B., Aikin, K.C., Atlas, E.L., Goldan, P.D., Graus, M., Hendershot, R., Isaacman-VanWertz, G.A., Koss, A., Kuster, W.C., Lueb, R.A., McLaughlin, R.J., Peischl, J., Sueper, D., Ryerson, T.B., Tokarek, T.W., Warneke, C., Yuan, B., de Gouw, J.A., 2017. An improved, automated whole air sampler and gas chromatography mass spectrometry analysis system for volatile organic compounds in the atmosphere. Atmos. Meas. Tech. 10, 291–313. https://doi.org/10.5194/amt-10-291-2017

Luecken, D.J., Hutzell, W.T., Strum, M.L., Pouliot, G.A., 2012. Regional sources of atmospheric formaldehyde and acetaldehyde, and implications for atmospheric modeling. Atmos. Environ. 47, 477–490. https://doi.org/10.1016/j.atmosenv.2011.10.005

Mao, J., Carlton, A.G., Cohen, R.C., Brune, W.H., Brown, S.S., Wolfe, G.M., Jimenez, J.L., Pye, H.O.T., Lee Ng, N., Xu, L., McNeill, V.F., Tsigaridis, K., McDonald, B.C., Warneke, C., Guenther, A., Alvarado, M.J., de Gouw, J., Mickley, L.J., Leibensperger, E.M., Mathur, R., Nolte, C.G., Portmann, R.W., Unger, N., Tosca, M., Horowitz, L.W., 2018. Southeast Atmosphere Studies: Learning from model-observation syntheses. Atmos. Chem. Phys. 18, 2615–2651. https://doi.org/10.5194/acp-18-2615-2018

Mao, J., Horowitz, L.W., Naik, V., Fan, S., Liu, J., Fiore, A.M., 2013a. Sensitivity of tropospheric oxidants to biomass burning emissions: Implications for radiative forcing. Geophys. Res. Lett. 40, 1241–1246. https://doi.org/10.1002/grl.50210

Mao, J., Paulot, F., Jacob, D.J., Cohen, R.C., Crounse, J.D., Wennberg, P.O., Keller, C.A., Hudman, R.C., Barkley, M.P., Horowitz, L.W., 2013b. Ozone and organic nitrates over the eastern United States: Sensitivity to isoprene chemistry. J. Geophys. Res. Atmos. 118, 11256–11268. https://doi.org/10.1002/jgrd.50817

Marais, E.A., Jacob, D.J., Jimenez, J.L., Campuzano-Jost, P., Day, D.A., Hu, W., Krechmer, J., Zhu, L., Kim, P.S., Miller, C.C., Fisher, J.A., Travis, K., Yu, K., Hanisco, T.F., Wolfe, G.M., Arkinson, H.L., Pye, H.O.T., Froyd, K.D., Liao, J., McNeill, V.F., 2016. Aqueous-phase mechanism for secondary organic aerosol formation from isoprene: Application to the southeast United States and co-benefit of SO2 emission controls. Atmos. Chem. Phys. 16, 1603–1618. https://doi.org/10.5194/acp-16-1603-2016

Marais, E.A., Jacob, D.J., Kurosu, T.P., Chance, K., Murphy, J.G., Reeves, C., Mills, G., Casadio, S., Millet, D.B., Barkley, M.P., Paulot, F., Mao, J., 2012. Isoprene emissions in Africa inferred from OMI observations of formaldehyde columns. Atmos. Chem. Phys. 12, 6219–6235. https://doi.org/10.5194/acp-12-6219-2012

Marvin, M.R., Salawitch, R.J., Wolfe, G.M., Canty, T.P., He, H., Ring, A., Hembeck, L., Goldberg, D.L., Pye, H.O.T., Aikin, K.C., de Gouw, J.A., Graush, M., Hanisco, T.F., Holloway, J.S., Hübler, G., Kaiser, J., Keutsch, F.N., Peischl, J., Pollack, I.B., Roberts, J.M., Ryerson, T.B., Veres, P.R., Warneke, C., 2019. Impact of improved isoprene oxidation chemistry on regional modeling of ozone and its precursors (in preparation).

Marvin, M.R., Wolfe, G.M., Salawitch, R.J., Canty, T.P., Roberts, S.J., Travis, K.R., Aikin, K.C., de Gouw, J.A., Graus, M., Hanisco, T.F., Holloway, J.S., Hübler, G., Kaiser, J., Keutsch, F.N., Peischl, J., Pollack, I.B., Roberts, J.M., Ryerson, T.B., Veres, P.R., Warneke, C., 2017. Impact of evolving isoprene mechanisms on simulated formaldehyde: An inter-comparison supported by in situ observations from SENEX. Atmos. Environ. 164, 325–336. https://doi.org/10.1016/j.atmosenv.2017.05.049

Millet, D.B., Jacob, D.J., Boersma, K.F., Fu, T.-M., Kurosu, T.P., Chance, K., Heald, C.L., Guenther, A.B., 2008. Spatial distribution of isoprene emissions from North America derived from formaldehyde column measurements by the OMI satellite sensor. J. Geophys. Res. Atmos. 113. https://doi.org/10.1029/2007JD008950

Müller, M., Anderson, B.E., Beyersdorf, A.J., Crawford, J.H., Diskin, G.S., Eichler, P., Fried, A., Keutsch, F.N., Mikoviny, T., Thornhill, K.L., Walega, J.G., Weinheimer, A.J., Yang, M., Yokelson, R.J., Wisthaler, A., 2016. In situ measurements and modeling of reactive trace gases in a small biomass burning plume. Atmos. Chem. Phys. 16, 3813–3824.

Naik, V., Horowitz, L., Fiore, A.M., Ginoux, P., Mao, J., Aghedo, A.M., Levy, H., 2013. Impact of preindustrial to present-day changes in short-lived pollutant emissions on atmospheric composition and climate forcing. J. Geophys. Res. Atmos. 118, 8086–8110. https://doi.org/10.1002/jgrd.50608

Neuman, J.A., Huey, L.G., Dissly, R.W., Fehsenfeld, F.C., Flocke, F., Holecek, J.C., Holloway, J.S., Hübler, G., Jakoubek, R., Nicks, D.K., Parrish, D.D., Ryerson, T.B., Sueper, D.T., Weinheimer, A.J., 2002. Fast-response airborne in situ measurements of HNO3 during the Texas 2000 Air Quality Study. J. Geophys. Res. Atmos. 107. https://doi.org/10.1029/2001JD001437

Neuman, J.A., Ryerson, T.B., Huey, L.G., Jakoubek, R., Nowak, J.B., Simons, C., Fehsenfeld, F.C., 2003. Calibration and evaluation of nitric acid and ammonia permeation tubes by UV optical absorption. Environ. Sci. Technol. 37, 2975–2981. https://doi.org/10.1021/es026422l

Nopmongcol, U., Koo, B., Tai, E., Jung, J., Piyachaturawat, P., Emery, C., Yarwood, G., Pirovano, G., Mitsakou, C., Kallos, G., 2012. Modeling Europe with CAMx for the Air Quality Model Evaluation International Initiative (AQMEII). Atmos. Environ. 53, 177–185. https://doi.org/10.1016/j.atmosenv.2011.11.023

Palmer, P.I., Jacob, D.J., Fiore, A.M., Martin, R. V, Chance, K., Kurosu, T.P., 2003. Mapping isoprene emissions over North America using formaldehyde column observations from space. J. Geophys. Res. Atmos. 108. https://doi.org/10.1029/2002JD002153

Paulot, F., Crounse, J.D., Kjaergaard, H.G., Kroll, J.H., Seinfeld, J.H., Wennberg, P.O., 2009a. Isoprene photooxidation: New insights into the production of acids and organic nitrates. Atmos. Chem. Phys. 9, 1479–1501. https://doi.org/10.5194/acp-9-1479-2009

Paulot, F., Crounse, J.D., Kjaergaard, H.G., Kurten, A., St Clair, J.M., Seinfeld, J.H., Wennberg, P.O., 2009b. Unexpected epoxide formation in the gas-phase photooxidation of isoprene. Science. 325, 730–733. https://doi.org/10.1126/science.1172910

Paulson, S.E., Seinfeld, J.H., 1992. Development and evaluation of a photooxidation mechanism for isoprene. J. Geophys. Res. Atmos. 97, 20703–20715. https://doi.org/10.1029/92JD01914
Peeters, J., Müller, J.F., 2010. HOx radical regeneration in isoprene oxidation via peroxy radical isomerisations. II: Experimental evidence and global impact. Phys. Chem. Chem. Phys. 12, 14227–14235. https://doi.org/10.1039/c0cp00811g
Peeters, J., Muller, J.F., Stavrakou, T., Nguyen, V.S., 2014. Hydroxyl radical recycling in isoprene oxidation driven by hydrogen bonding and hydrogen tunneling: The upgraded LIM1 mechanism. J. Phys. Chem. A. 118, 8625–8643. https://doi.org/10.1021/jp5033146
Peeters, J., Nguyen, T.L., Vereecken, L., 2009. HOx radical regeneration in the oxidation of isoprene. Phys. Chem. Chem. Phys. 11, 5935–5939. https://doi.org/10.1039/b908511d
Pickering, K.E., Wang, Y., Tao, W.-K., Price, C., Müller, J.-F., 1998. Vertical distributions of lightning NOx for use in regional and global chemical transport models. J. Geophys. Res. Atmos. 103, 31203–31216. https://doi.org/10.1029/98JD02651
Pike, R.C., Young, P.J., 2009. How plants can influence tropospheric chemistry: The role of isoprene emissions from the biosphere. Weather. 64, 332–336. https://doi.org/10.1002/wea.416
Pleim, J.E., 2007. A combined local and nonlocal closure model for the atmospheric boundary layer. Part I: Model description and testing. J. Appl. Meteorol. Climatol. 46, 1383–1395. https://doi.org/10.1175/JAM2539.1
Pleim, J.E., Bash, J.O., Walker, J.T., Cooter, E.J., 2013. Development and evaluation of an ammonia bidirectional flux parameterization for air quality models. J. Geophys. Res. Atmos. 118, 3794–3806. https://doi.org/10.1002/jgrd.50262
Pöschl, U., von Kuhlmann, R., Poisson, N., Crutzen, P.J., 2000. Development and intercomparison of condensed isoprene oxidation mechanisms for global atmospheric modeling. J. Atmos. Chem. 37, 29–52. https://doi.org/10.1023/a:1006391009798
Pouliot, G., Pierce, T., Benjey, W., O'neill, S.M., Ferguson, S.A., 2005. Wildfire emission modeling: Integrating BlueSky and SMOKE. Research Triangle Park, NC.
Pye, H.O.T., Luecken, D.J., Xu, L., Boyd, C.M., Ng, N.L., Baker, K.R., Ayres, B.R., Bash, J.O., Baumann, K., Carter, W.P.L., Edgerton, E., Fry, J.L., Hutzell, W.T., Schwede, D.B., Shepson, P.B., 2015. Modeling the current and future roles of particulate organic nitrates in the Southeastern United States. Environ. Sci. Technol. 49, 14195–14203. https://doi.org/10.1021/acs.est.5b03738
Pye, H.O.T., Zuend, A., Fry, J.L., Isaacman-Vanwertz, G., Capps, S.L., Appel, K.W., Foroutan, H., Xu, L., Ng, N.L., Goldstein, A.H., 2018. Coupling of organic and inorganic aerosol systems and the effect on gas-particle partitioning in the southeastern US. Atmos. Chem. Phys. 185194, 357–370. https://doi.org/10.5194/acp-18-357-2018
Ramboll Environ, 2018. CAMx User's Guide Version 6.50. Novato, CA.

Riedel, T.P., Wolfe, G.M., Danas, K.T., Gilman, J.B., Kuster, W.C., Bon, D.M., Vlasenko, A., Li, S.-M., Williams, E.J., Lerner, B.M., Veres, P.R., Roberts, J.M., Holloway, J.S., Lefer, B., Brown, S.S., Thornton, J.A., 2014. An MCM modeling study of nitryl chloride (ClNO2) impacts on oxidation, ozone production and nitrogen oxide partitioning in polluted continental outflow. Atmos. Chem. Phys. 14, 3789–3800.

Ring, A.M., Canty, T.P., Anderson, D.C., Vinciguerra, T.P., He, H., Goldberg, D.L., Ehrman, S.H., Dickerson, R.R., Salawitch, R.J., 2018. Evaluating commercial marine emissions and their role in air quality policy using observations and the CMAQ model. Atmos. Environ. 173, 96–107. https://doi.org/10.1016/j.atmosenv.2017.10.037

Rio, C., Hourdin, F., Chédin, A., 2010. Numerical simulation of tropospheric injection of biomass burning products by pyro-thermal plumes. Atmos. Chem. Phys. 10, 3463–3478.

Roberts, S.J., Salawitch, R.J., Wolfe, G.M., Marvin, M.R., Canty, T.P., Hall, D., Dickerson, R.R., Krask, D.J., 2019. Multidecadal trends in ozone and ozone chemistry in the Baltimore-Washington Region (in preparation).

Romer, P.S., Duffey, K.C., Wooldridge, P.J., Edgerton, E., Baumann, K., Feiner, P.A., Miller, D.O., Brune, W.H., Koss, A.R., de Gouw, J.A., Misztal, P.K., Goldstein, A.H., Cohen, R.C., 2018. Effects of temperature-dependent NOx emissions on continental ozone production. Atmos. Chem. Phys. 18, 2601–2614.

Ryerson, T.B., Buhr, M.P., Frost, G.J., Goldan, P.D., Holloway, J.S., Htibler, G., Jobson, B.T., Kuster, W.C., Mckeen, S.A., Parrish, D.D., Roberts, J.M., Sueper, D.T., Trainer, M., Williams, J., Fehsenfeld, F.C., 1998. Emissions lifetimes and ozone formation in power plant plumes. J. Geophys. Res. Atmos. 103, 569–591. https://doi.org/10.1029/98JD01620

Ryerson, T.B., Huey, L.G., Knapp, K., Neuman, J.A., Parrish, D.D., Sueper, D.T., Fehsenfeld, F.C., 1999. Design and initial characterization of an inlet for gas-phase NOy measurements from aircraft. J. Geophys. Res. Atmos. 104, 5483–5492. https://doi.org/10.1029/1998JD100087

Ryerson, T.B., Williams, E.J., Fehsenfeld, F.C., 2000. An efficient photolysis system for fast-response NO2 measurements. J. Geophys. Res. Atmos. 105, 447–473. https://doi.org/10.1029/2000JD900389

Saunders, S.M., Jenkin, M.E., Derwent, R.G., Pilling, M.J., 2003. Protocol for the development of the Master Chemical Mechanism, MCM v3 (Part A): Tropospheric degradation of non-aromatic volatile organic compounds. Atmos. Chem. Phys. 3, 161–180. https://doi.org/10.5194/acp-3-161-2003

Seto, D., Clements, C.B., 2011. Fire whirl evolution observed during a valley wind-sea breeze reversal. J. Combust. 2011, 1–12. https://doi.org/10.1155/2011/569475

Sillman, S., 1999. The relation between ozone, NOx and hydrocarbons in urban and polluted rural environments. Atmos. Environ. 33, 1821–1845.

Sillman, S., 1995. The use of NOy, H2O2, and HNO3 as indicators for ozone-NOx-hydrocarbon sensitivity in urban locations. J. Geophys. Res. Atmos. 100, 14175–14188. https://doi.org/10.1029/94JD02953

Sillman, S., Logan, J.A., Wofsy, S.C., 1990. The sensitivity of ozone to nitrogen oxides and hydrocarbons in regional ozone episodes. J. Geophys. Res. Atmos. 95, 1837–1851. https://doi.org/10.1029/JD095iD02p01837

Simon, H., Reff, A., Wells, B., Xing, J., Frank, N., 2015. Ozone trends across the United States over a period of decreasing NOx and VOC emissions. Environ. Sci. Technol. 49, 186–195. https://doi.org/10.1021/es504514z

Skamarock, W.C., Klemp, J.B., Dudhia, J., Gill, D.O., Barker, D.M., Duda, M.G., Huang, X.-Y., Wang, W., Powers, J.G., 2008. A description of the Advanced Research WRF Version 3. Boulder, CO.

St. Clair, J.M., Rivera-Rios, J.C., Crounse, J.D., Praske, E., Kim, M.J., Wolfe, G.M., Keutsch, F.N., Wennberg, P.O., Hanisco, T.F., 2016. Investigation of a potential HCHO measurement artifact from ISOPOOH. Atmos. Meas. Tech. 9, 4561–4568. https://doi.org/10.5194/amt-9-4561-2016

Stockwell, W.R., Kirchner, F., Kuhn, M., Seefeld, S., 1997. A new mechanism for regional atmospheric chemistry modeling. J. Geophys. Res. Atmos. 102, 847–872. https://doi.org/10.1029/97JD00849

Thornton, J.A., Wooldridge, P.J., Cohen, R.C., Martinez, M., Harder, H., Brune, W.H., Williams, E.J., Roberts, J.M., Fehsenfeld, F.C., Hall, S.R., Shetter, R.E., Wert, B.P., Fried, A., 2002. Ozone production rates as a function of NOx abundances and HOx production rates in the Nashville urban plume. J. Geophys. Res. Atmos. 107, 4146. https://doi.org/10.1029/2001JD000932

Toon, O.B., Maring, H., Dibb, J., Ferrare, R., Jacob, D.J., Jensen, E.J., Luo, Z.J., Mace, G.G., Pan, L.L., Pfister, L., Rosenlof, K.H., Redemann, J., Reid, J.S., Singh, H.B., Thompson, A.M., Yokelson, R., Minnis, P., Chen, G., Jucks, K.W., Pszenny, A., 2016. Planning, implementation, and scientific goals of the Studies of Emissions and Atmospheric Composition, Clouds and Climate Coupling by Regional Surveys (SEAC4RS) field mission. J. Geophys. Res. Atmos. 121, 4967–5009. https://doi.org/10.1002/2015JD024297

Trainer, M., Williams, E.J., Parrish, D.D., Buhr, M.P., Allwine, E.J., Westberg, H.H., Fehsenfeld, F.C., Liu, S.C., 1987. Models and observations of the impact of natural hydrocarbons on rural ozone. Nature. 329, 705–707. https://doi.org/10.1038/329705a0

Travis, K.R., Jacob, D.J., Fisher, J.A., Kim, P.S., Marais, E.A., Zhu, L., Yu, K., Miller, C.C., Yantosca, R.M., Sulprizio, M.P., Thompson, A.M., Wennberg, P.O., Crounse, J.D., St. Clair, J.M., Cohen, R.C., Laughner, J.L., Dibb, J.E., Hall, S.R., Ullmann, K., Wolfe, G.M., Pollack, I.B., Peischl, J., Neuman, J.A., Zhou, X., 2016. Why do models overestimate surface ozone in the Southeast United States? Atmos. Chem. Phys. 16, 13561–13577. https://doi.org/10.5194/acp-16-13561-2016

Trentmann, J., Luderer, G., Winterrath, T., Fromm, M.D., Servranckx, R., Textor, C., Herzog, M., Graf, H., Andreae, M.O., 2006. Modeling of biomass smoke injection into the lower stratosphere by a large forest fire (Part I): Reference simulation. Atmos. Chem. Phys. 6, 5247–5260.

Veres, P.R., Roberts, J.M., 2015. Development of a photochemical source for the production and calibration of acyl peroxynitrate compounds. Atmos. Meas. Tech. 8, 2225–2231. https://doi.org/10.5194/amt-8-2225-2015

Vijayaraghavan, K., Lindhjem, C., Koo, B., DenBleyker, A., Tai, E., Shah, T., Alvarez, Y., Yarwood, G., 2016. Source apportionment of emissions from light-duty gasoline vehicles and other sources in the United States for ozone and particulate matter. J. Air Waste Manage. Assoc. 66, 98–119. https://doi.org/10.1080/10962247.2015.1112316

von Kuhlmann, R., Lawrence, M.G., Pöschl, U., Crutzen, P.J., 2004. Sensitivities in global scale modeling of isoprene. Atmos. Chem. Phys. 4, 1–17. https://doi.org/10.5194/acp-4-1-2004

Wang, Y., Jacob, D.J., Logan, J.A., 1998. Global simulation of tropospheric O3-NOx-hydrocarbon chemistry: 1. Model formulation. J. Geophys. Res. Atmos. 103, 10713–10725.

Warneke, C., de Gouw, J.A., Del Negro, L., Brioude, J., McKeen, S., Stark, H., Kuster, W.C., Goldan, P.D., Trainer, M., Fehsenfeld, F.C., Wiedinmyer, C., Guenther, A.B., Hansel, A., Wisthaler, A., Atlas, E., Holloway, J.S., Ryerson, T.B., Peischl, J., Huey, L.G., Hanks, A.T.C., 2010. Biogenic emission measurement and inventories determination of biogenic emissions in the eastern United States and Texas and comparison with biogenic emission inventories. J. Geophys. Res. Atmos. 115. https://doi.org/10.1029/2009jd012445

Warneke, C., Trainer, M., de Gouw, J.A., Parrish, D.D., Fahey, D.W., Ravishankara, A.R., Middlebrook, A.M., Brock, C.A., Roberts, J.M., Brown, S.S., Neuman, J.A., Lerner, B.M., Lack, D., Law, D., Hübler, G., Pollack, I., Sjostedt, S., Ryerson, T.B., Gilman, J.B., Liao, J., Holloway, J., Peischl, J., Nowak, J.B., Aikin, K.C., Min, K.E., Washenfelder, R.A., Graus, M.G., Richardson, M., Markovic, M.Z., Wagner, N.L., Welti, A., Veres, P.R., Edwards, P., Schwarz, J.P., Gordon, T., Dube, W.P., McKeen, S.A., Brioude, J., Ahmadov, R., Bougiatioti, A., Lin, J.J., Nenes, A., Wolfe, G.M., Hanisco, T.F., Lee, B.H., Lopez-Hilfiker, F.D., Thornton, J.A., Keutsch, F.N., Kaiser, J., Mao, J., Hatch, C.D., 2016. Instrumentation and measurement strategy for the NOAA SENEX aircraft campaign as part of the Southeast Atmosphere Study 2013. Atmos. Meas. Tech. 9, 3063–3093. https://doi.org/10.5194/amt-9-3063-2016

Whitten, G., Deuel, H.P., Burton, C.S., Haney, J.L., 1996. Overview of the implementation of an updated isoprene chemistry mechanism in CB4/UAM-V. San Rafael, CA.

Wolfe, G.M., Cantrell, C., Kim, S., Mauldin Iii, R.L., Karl, T., Harley, P., Turnipseed, A., Zheng, W., Flocke, F., Apel, E.C., Hornbrook, R.S., Hall, S.R., Ullmann, K., Henry, S.B., DiGangi, J.P., Boyle, E.S., Kaser, L., Schnitzhofer, R., Hansel, A., Graus, M., Nakashima, Y., Kajii, Y., Guenther, A., Keutsch, F.N., 2014. Missing peroxy radical sources within a summertime ponderosa pine forest. Atmos. Chem. Phys. 14, 4715–4732. https://doi.org/10.5194/acp-14-4715-2014

Wolfe, G.M., Crounse, J.D., Parrish, J.D., St. Clair, J.M., Beaver, M.R., Paulot, F., Yoon, T.P., Wennberg, P.O., Keutsch, F.N., 2012. Photolysis, OH reactivity and ozone reactivity of a proxy for isoprene-derived hydroperoxyenals (HPALDs). Phys. Chem. Chem. Phys. 14, 7276–7286. https://doi.org/10.1039/C2CP40388A

Wolfe, G.M., Hanisco, T.F., Arkinson, H.L., Bui, T.P., Crounse, J.D., Dean-Day, J., Goldstein, A., Guenther, A., Hall, S.R., Huey, G., Jacob, D.J., Karl, T., Kim, P.S., Liu, X., Marvin, M.R., Mikoviny, T., Misztal, P.K., Nguyen, T.B., Peischl, J., Pollack, I., Ryerson, T., St. Clair, J.M., Teng, A., Travis, K.R., Ullmann, K., Wennberg, P.O., Wisthaler, A., 2015. Quantifying sources and sinks of reactive gases in the lower atmosphere using airborne flux observations. Geophys. Res. Lett. 42. https://doi.org/10.1002/2015GL065839

Wolfe, G.M., Kaiser, J., Hanisco, T.F., Keutsch, F.N., De Gouw, J.A., Gilman, J.B., Graus, M., Hatch, C.D., Holloway, J., Horowitz, L.W., Lee, B.H., Lerner, B.M., Lopez-Hilifiker, F., Mao, J., Marvin, M.R., Peischl, J., Pollack, I.B., Roberts, J.M., Ryerson, T.B., Thornton, J.A., Veres, P.R., Warneke, C., 2016a. Formaldehyde production from isoprene oxidation across NOx regimes. Atmos. Chem. Phys. 16. https://doi.org/10.5194/acp-16-2597-2016

Wolfe, G.M., Marvin, M.R., Roberts, S.J., Travis, K.R., Liao, J., 2016b. The Framework for 0-D Atmospheric Modeling (F0AM) v3.1. Geosci. Model Dev. 9. https://doi.org/10.5194/gmd-9-3309-2016

Yarwood, G., Jung, J., Whitten, G.Z., Heo, G., Mellberg, J., Estes, E., 2010. Updates to the Carbon Bond Mechanism for Version 6 (CB6). Novato, CA.

Yarwood, G., Rao, S., Yocke, M., Whitten, G.Z., 2005. Updates to the Carbon Bond chemical mechanism: CB05. Novato, CA.

Yarwood, G., Sakulyanontvittaya, T., Nopmongcol, O., Koo, B., 2014. Ozone depletion by bromine and iodine over the gulf of mexico. Novato, CA.

Zhang, H., Rattanavaraha, W., Zhou, Y., Bapat, J., Rosen, E.P., Sexton, K.G., Kamens, R.M., 2011. A new gas-phase condensed mechanism of isoprene-NOx photooxidation. Atmos. Environ. 45, 4507–4521. https://doi.org/10.1016/j.atmosenv.2011.04.011